Study of interaction effect between a line inclusion and a hole using Digital Photoelasticity

Satish Prakash Thorat

A Thesis Submitted to
Indian Institute of Technology Hyderabad
In Partial Fulfillment of the Requirements for
The Degree of Master of Technology

भारतीय प्रौद्योगिकी संस्थान हैदराबाद
Indian Institute of Technology Hyderabad

Department of Mechanical and Aerospace Engineering

June 2018

Declaration

I declare that this written submission represents my ideas in my own words, and where ideas or words of others have been included, I have adequately cited and referenced the original sources. I also declare that I have adhered to all principles of academic honesty and integrity and have not misrepresented or fabricated or falsified any idea/data/fact/source in my submission. I understand that any violation of the above will be a cause for disciplinary action by the Institute and can also evoke penal action from the sources that have thus not been properly cited, or from whom proper permission has not been taken when needed.
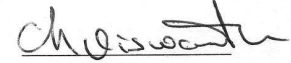
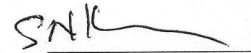_____
(Signature)

Satish Prakash Thorat
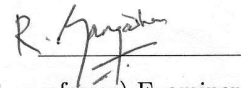
ME16MTECH11010
(Roll No.)

Approval Sheet

This thesis entitled **Study of interaction effect between A line inclusion and A hole using digital photoelasticity** by Satish Prakash Thorat is approved for the degree of Master of Technology from IIT Hyderabad.

(Dr. Viswanath Chinthapenta, Asst. professor) Examiner,
Dept. of Mechanical and Aerospace Engineering,
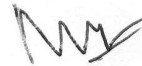IIT Hyderabad.

(Dr. Syed Nizamuddin Khaderi, Asst. professor) Examiner,
Dept. of Mechanical and Aerospace Engineering,
IIT Hyderabad.

(Dr. Gangadharan Raju, Asst. professor) Examiner,
Dept. of Mechanical and Aerospace Engineering,
IIT Hyderabad.

(Dr. M. Ramji, Asso. professor) Adviser,
Dept. of Mechanical and Aerospace Engineering,
IIT Hyderabad.

(Dr. S. Suriya Prakash, Asso. professor) Chairman,
Dept. of Civil Engineering,
IIT Hyderabad.

Acknowledgements

Foremost, I would like to express my sincere gratitude to my advisor **Dr. M. Ramji** for the continuous support for my M.Tech study and research, for his patience, motivation, and valuable guidance. This work could not have been achieved if it was not for his encouragement and solutions to many problems that I faced.

I also would like to thank my fellow lab members of Engineering Optics Lab, **Mr. Prataprao Patil, Mr. Naresh Reddy, Mr. Matta Sheshadri** and **Mr. Jobin T. Mathews** for their constant support, friendly environment in the lab and guidance in experiments.

I would also like to thank entire workshop staff especially **Mr. A. Praveen Kumar, Mr. Pramod M. Lohkare, Mr. M. Madhu Babu, Mr. G. Ramu** and **Mr. B. Ramesh** for their valuable assistance in specimen preparation. Also, I thank my classmates and friends at IIT Hyderabad for their help and support.

Last but not the least, I would like to thank my family for all the love and support.

Dedication

To

My Primary and Secondary School Teachers
Shewalkar Sir, Giri Sir, Parihar Sir

And

My Family
{After all, Family is Power.}

Abstract

The ease of fabrication and superior mechanical properties has emerged the new application areas for short-fibre-reinforced-polymers (SFRP). These SFRP has a new range of performance capabilities and is designed to fill the property gap between polymers and sophisticated continuous-fibre-reinforced-polymers (CFRP). Increased applications of composite materials have also increased the need of defects studies and effect of these defects on their mechanical and other properties too. The most common and much intense defect observed in the composite materials is porosity, the presence of voids in the matrix phase. The void content is the potentially harmful defect in the composite materials and can significantly affect the mechanical properties. In case of SFRPs, fibre end singularity problems are often modelled and studied as fibres as inclusions where the focus is on finding fracture parameters like stress intensity factor. The present study is devoted to exploring the effect of void on the fracture properties, in case of SFRPs. This problem is studied for the simplest form where the voids are modelled for the 2D case, i.e. a circular hole near the fibre. Hence the problem solved is a rigid line inclusion(indicates fibres) with a hole(indicates 2D voids) embedded in a matrix-resin. There are two reasons for modelling the fibre as a rigid line inclusion. First is the thickness of the steel inclusion, that we have used, is very small compared to other specimen dimensions. Second is the strength of the steel is very high compared to the strength of matrix-resin which is such true case in SFRP where fibre has more strength than that of the matrix material. Instead of stress intensity factor, strain intensity factor is used for quantifying the singularities at the tip of the inclusion because it is more appropriate to use in case of inclusion problems. Further, the variation of strain intensity factor with respect to three parameters, namely diameter of a hole, length of line inclusion and the distance between the inclusion and a hole is studied. We have used a numerical methodology, based on the reciprocal theorem, to calculate the strain intensity factor of the inclusion in the finite geometry. The input to this method is the actual elasticity solution, which is obtained using finite element analysis (FEA). Furthermore, these FEA models are validated using the experimental technique, Digital Photoelasticity, qualitatively and quantitatively as well.

Contents

List of Figures

List of Tables

Nomenclature

Symbols

Symbol	Unit	Description
K_I	MPa m$^{1/2}$	Stress intensity factor for mode I
K_I^ϵ	m$^{1/2}$	Strain intensity factor for mode I
F_σ	N/mm/fringe	Material fringe value
α	degree/radian	Orientation angle of slow axis of the Polariser
ζ	degree/radian	Orientation angle of slow axis of First Quarter wave plate
η	degree/radian	Orientation angle of slow axis of Second Quarter wave plate
β	degree/radian	Orientation angle of slow axis of Analyser
N	-	Fringe order
n	-	Number of parameters used in multi-parameters stress field equations
δ	radian	Phase retardation obtained when light passes through an optical element
θ_c	degree/radian	Isoclinic corresponds to principal stress direction
δ_c	radian	Isochromatic corresponds to principal stress difference
E	MPa	Young's modulus
ν	-	Poisson's ratio
μ	MPa	Shear modulus
κ	-	Kappa. $(3 - 4\nu)$, for plane strain and $(3 - \nu)/(1 + \nu)$, for plane stress condition.
ϕ	-	Eigen stress function for singular problems
J	MPa^2	Convergence error
λ	-	Order of singularity
L	mm	Inclusion length
s	mm	Distance between the rigid line inclusion and the centre of the hole
D	mm	Diameter of the hole
I_a	-	Light intensity of light emitted by the source
I_b	-	Surrounding light intensity or noise

Abbreviation

Abbreviation	Description
NSIF	Normalised strain intensity factor
SFRP	Short-fibre-reinforcement-polymers
CFRP	Continuous-fibre-reinforcement-polymers
ILSS	Inter-laminar shear stress
PST	Phase shifting technique used for unwrapping of isochromatic data
AGQUP	Adaptive Quality Guided Unwrapping Algorithm
DIC	Digital image correlation
CPE8H	Eight nodded plane strain hybrid element used for modelling in ABAQUS
CCD	Charge coupled device

Chapter 1

Introduction and Literature Review

1.1 Introduction

1.1.1 Introduction to SFRP

Composite materials are the materials made from two or more materials with different properties when combined gives a very high strength material compared to its constituent elements. Studies on composite materials gave us more insight into their fabrication processes, material and behaviour properties and failures which opened the new applications areas for it. Fibre-reinforced-polymers, namely composite materials are the trending materials used in structures because of their superior mechanical, thermal and electrical properties. Among the other properties of composite materials, the high strength-to-weight and modulus-to-weight properties are the most important properties to increase its use in structures and aerospace.

Principal constituents of composite materials are reinforcements - fibres which gives strength to composite materials and the matrix which adheres the reinforcement phases in place and deforms to distribute the stresses between the constituent reinforcement materials under an applied force. The performance of composites is estimated by shape, length, orientation, and content of the fibres and the mechanical properties of the matrix. Composite materials are classified based on aspect ratio defined as

$$\mathcal{S} = \frac{\text{length of the fibre}}{\text{diameter of the fibre}} = \frac{l}{d}. \tag{1.1}$$

These are mainly classified as continuous-fibre-reinforced-polymers(CFRP) and short-fibre-reinforced-polymers (SFRP). For SFRP, the aspect ratio ranges from $50 - 500$ [1]. CFRP is used, instead of metallic components, especially in aerospace industries, while the SFRP is used, instead of plane polymeric material, for electrical, packaging and automotive applications [2].

Composites with shorter fibres with the proper orientation that use glass, ceramic or multi-purpose fibres can produce considerably higher strength than those that use continuous fibres. Short fibres are also known for their theoretically higher strength. Also, SFRP is very easy to manufacture in large quantity, hence eligible for industrial production. In SFRP, both fibre and matrix take the applied load, and this applied load transfer between the matrix and fibre happens via the fibre-
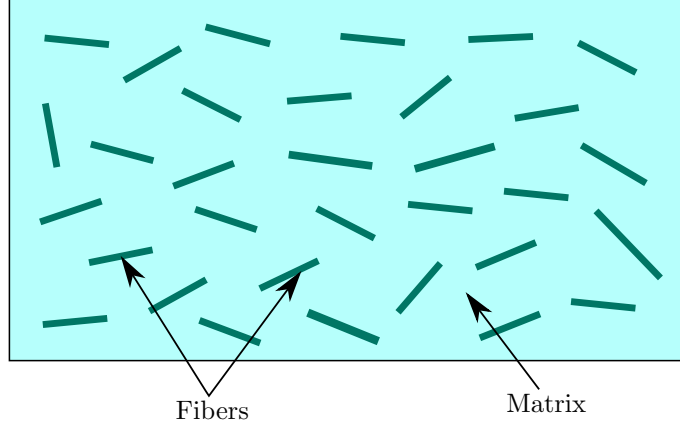
Figure 1.1: A typical distribution of fibres embedded in the matrix in SFRP

matrix interface. As a result, SFRP has superior strength and elastic stiffness over the parent polymeric material [1]. SFRP are now widely used in automobile [3, 4, 5], aerospace and secondary load bearing structures [6]. As the diameter of fibres is very small, usually in microns, compared to the diameter, fibres look more like powder to the unassisted eyes. Enhancement in mechanical properties can be obtained by using a higher aspect ratio in SFRP. But using higher aspect ratio leads the reduction in failure strain and hardness [7]. In general in SFRP, the fibre orientation and its spacing are random as shown in fig 1.1. Also, their mechanical properties mainly depend on two variables, namely a) mean fibre diameter and b) fibre orientation with loading direction. For shorter fibre length, an increase in mean fibre length increases the strength of SFRP, but for longer fibre length, there is almost no effect on the strength of SFRP [8]. Furthermore, the decrease in fibre orientation with loading direction increases the strength of SFRP.

1.1.2 Load transfer mechanism in SFRP

In composite materials, the applied load is shared by both matrix and fibres, though in different proportion, which makes it high strength and stiff. Also, fibres are immensely surrounded by the matrix material. Hence when an external load is applied to the composite structure, it acts on the matrix first and then it gets transferred to the fibres. The load transfer depends on the interface of matrix and fibres. A part of this load is transferred to the fibre through the fibre end and remaining transferred to the fibre through their external cylindrical surface by shear mechanism, as illustrated in the Fig. 1.2. The direct load transfer through fibre end is causing a direct stress σ_f in the fibre. As the shear stress, τ, is acting on the cylindrical surface of the fibre, it causes an increase in stress on one end of the fibre, i.e. $(\sigma_f + d\sigma_f)$. This mechanism is called as the shear mechanism. For the continuous-fibre-reinforced-composites, the load transfer to the fibre end is very low compared load transfer through fibre's external cylindrical surface because of the larger the cylindrical surface. But for the short-fibre-reinforced-composites, the same is not true because of their short length. Hence most of the load transfer happens through the fibre end which creates a stress concentration. Therefore, load transfer is important in the SFRP.

Stress concentration at the fibre end is responsible for fibre separation from the matrix or matrix yielding. Hence, investigators have studied this problem extensively. In these studies, they have
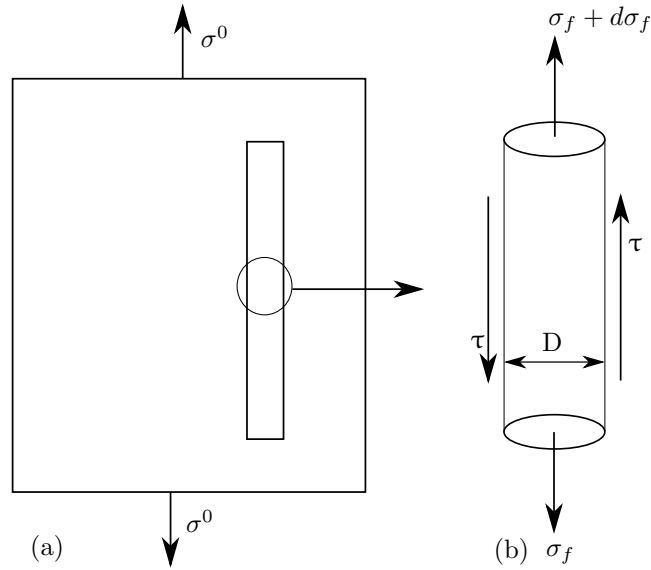
Figure 1.2: Load transfer to the fibre through matrix. (a) A lamina subjected to the stress σ^0, (b) A zoomed view of load transfer by shear mechanism

often modelled the problems fibres as inclusions embedded in the matrix.

1.1.3 Defects in composite materials

Defects can be inevitably introduced in the composite structures either during the material processing, manufacturing process or in the course of service life. These defects are known to adversely affect the performance of structural components in some way and also reduces expected performance. Hence, the size, shape, location and frequency of occurrence of the defects are supposed to be studied, in order to have the knowledge of defects growth in the expected service environment. This exercise can set the acceptance and rejection criterion for the manufacturing and in-service defects.

The manufacturing process can introduce a variety of defects as stated in the order of importance as porosity or presence of voids, foreign body inclusion, incorrect fibre volume fraction, bonding defects, fibre misalignment, ply misalignment, incompletely cured matrix, ply cracking, delaminations, fibre defects, etc. Incorrect fibre volume fraction happens due to excess or insufficient resin. Its local variations always happen but a large departure from specifications may be caused by inappropriate process conditions. Fibre misalignment can cause the local changes in volume fraction by preventing ideal packing of fibres. Ply misalignment can be a result of mistakes made in lay-up of the component plies which can significantly affect the overall stiffness and strength of the laminate. Delaminations are the planar defects and rarely occur during the manufacturing, but can be produced by contamination during lay-up and machining. Fibre defects include fibre kinks results of micro-buckling, broken fibres in the lamina, fibre distribution variance, etc. Fibre defects are one of the demerits in determining the correct strength. These defects are always present, hence must be considered as one of the basic material properties.

Porosity can be caused by volatile resin components, incorrect or non-optimal cure parameters such as duration, temperature, pressure, or vacuum bleeding of resin. Most of these parameters responsible in some way to entrapping the air to structure component. Porosity levels or voids

content can be significant and critical, as they greatly affect mechanical performance parameters, such as inter-laminar shear stress (ILSS).

Composite materials can be degraded in service by a number of mechanisms and those of most are prone environment experienced and materials used. This degradation can be caused due to static overload, impact, fatigue, hygrothermal effects, overheating, lightning strike and creep. The defects in the order of importance are as follows delaminations, bond failures (fibre-matrix debonding), cracks (matrix cracking and crazing), the entrance of moisture, fracture or buckling of fibres, failure of the interface between the fibres and matrix. Delaminations are the most important and most occurring defects in service life. These are a matrix defect, where in-plane matrix cracks propagate between plies of a laminate or within a laminate, where cracks run parallel to the fibre direction.

1.1.4   Voids in composite materials

Studies showed that the limitations of manufacturing processes and uneven process parameters affects the properties of composite materials and also induces the defects, such as voids, delaminations, uneven distribution of resin, and many more. One of the important defects in composite materials is formation of voids or bubbles which greatly affects the mechanical properties such as inter-laminar shear stress (ILSS) and also responsible for crack initiation and growth due to void coalescence. Voids in structures also leads to absorption of moisture which make structure corrosive prone. In SFRP, voids forms when air entraps-in during compounding and processing stages. Due to existence of temperature gradient during cooling, the uneven contraction of volume happens. These voids try to accumulates at the end of the fibre and their content depends on processing conditions, such as fibre concentration, fibre length, etc., [9]. Void content or void ratio can be calculated as

$$\text{Void Ratio}(e) = \frac{V_V}{V_S} = \frac{V_V}{V_T - V_V},\qquad(1.2)$$

where, V_V is volume of voids, V_S is volume of solids and V_T is volume of bulk material. Voids formation depends on various parameters. Voids content increases with the resin viscosity [10], injection and cure temperature of poring resin and vacuum pressure of process [11]. Also, it has been suggested and then implemented that there should be criterion for minimum percentage of void contents in the structure. Hence for aerospace structures approximately 1% of void contents in allowed and for other structures is 3% to 5%. A reduction in void contents from 40% to 10% can increase the flexural strength by nearly three times and almost doubles the modulus [12].

The methods for determining the void contents are microscopy of which optical and environmental scanning electron microscopy (ESEM) is the most commonly used, Archimedes density measurement, micro-computed tomography (micro-CT), etc. [13]. Though we can reduce the void content using precautions and controlled process parameters but it is almost impossible to avoid it at all. In manufacturing, various methods are employed to reduce the void contents such as vacuum injection moulding (VIM) which can reduce void contents to less than 3%. In industry, vacuum bagging around the laid-up component, and pressure within a pressurized autoclave technique are used [12].

4

1.2 Literature Review

The problem of singularity at fibre end is studied extensively by the investigators. A more in-depth understanding from these investigations is gained on the relationship between the reinforced phases, viz. fibre, matrix, etc., and their interaction when loaded. Study of microdamages near fibre ends is important in SFRP, as it directly affects the stiffness and strength of the composites [14]. Hence, in the literature, bulk investigations are done to quantify these microdamages with various methods. Studying the inclusion problems are the basic building block for these studies.

Atkinson [15] has provided displacement and stress field solution for ribbon like inclusion using complex variable approach and also has provided a alternative approach consisting a Fredholm equation in terms of shear stress on ribbon surface. He has studied both rigid and elastic ribbon inclusion. Wang et al. [16] has given the elastic stress and displacement fields near the tip of a rigid line inhomogeneity subjected to an inclined loading using both Eshelby's equivalent-inclusion method and complex potential approach of Muskhelishvili [17]. Also he has attempted to quantify the singularity at the tip of inclusion using various stress intensity factors. Ballarini [18] has provided the solution for stress intensity factor for the rigid line inclusion subjected to remote loading in transverse direction to inclusion length using a singular integral and Muskhelishvili's complex potential approach. Noselli et. al [19] studied the stress state near the rigid line inclusion using the photoelasticity technique. To remove dependency on Poisson's ratio of stress intensity factor, he defined stress intensity factor in strain term instead of stress term. In similar way, Pratap P et al. [20] have also suggested that the strain intensity factor (which is defined in terms of strain instead of stress terms), instead of stress intensity factor, for quantifying the magnitude of singularities at the tip of the rigid line inclusion using Stroh formulation.

Interaction problems are also useful for quantifying the various failures in SFRP material, because the composites fracture can be takes place by fibre breakage, matrix cracking and matrix-fibre interface do-bonding. Ishikawa and Kohno [21] has studied the debonding cracks at the fibre end by modelling this problems as a square hole and a rigid square inclusion in the infinite plate under tension loading using conformal mapping and Goursat stress functions. They also determined the stress singularities and stress intensity factors for Mode I and Mode II deformations. Again, Kohno and Ishikawa [22] have attempted the same problems, this time they modelled it as a lozenge hole and a rigid lozenge inclusion in the infinite plate with same loading and same approach. Gdoutos has studied [23] the propagation of a crack in the presence circular inclusion in an elastic plate subjected to uniform uniaxial tensile stress perpendicular to the axis of the crack. Li and Chudnovsky [24] have studied the crack interaction with elastic soft and stiff inclusion using the energy release rate and stress intensity factor criterion. Natarajan et al.[25] has studied the crack interaction with a single rigid circular inclusion and with a group of rigid inclusions in an elastic medium, using the extended finite element method (XFEM). Also they studied, numerically, influence of crack length, number of inclusions, and geometry of inclusions, on the crack tip stress field. Ayatollahi et al.[26] has studied, numerically, the effect of crack growth retardation by drilling the holes at crack-tip, under pure Mode I and Mode II loading conditions. Also the effect of different diameters on fatigue life is studied for same loading conditions. Thomas et al. [27] has studied circular holes and shrunk fit inclusion on the stress intensity factor using finite element alternating method (FEAM). This study is done for loading of Mode I and Mode II separately.

Sulym et al. [28] have studied the effect of circular hole on generalized stress intensity factor

(GSIF) of thin inclusion in an elastic isotropic medium. The effect is studied for two problems: a traction-free hole and a constrained hole with a thin inclusion.

1.2.1   Summary

Increased applications of SFRP has increased the need for a deeper investigation into the various failures and their improvement over it. In case of SFRP, the excessive stresses at fibre can lead to matrix cracking or fibre-matrix debonding. Hence, the study of stress behaviour at the fibre end is a serious and important topic in case of SFRP because of the singularities at fibre ends. Investigators have extensively studied these problems in different approaches. Modelling the fibres as rigid inclusions become a popular way of solving these problems and hence for these problems solutions are now available. Furthermore, the interaction problems are also important to investigate the failures, like fibre breakage, matrix cracking and matrix-fibre interface do-bonding. The work of Ishikawa and Kohno related to debonding at the fibre ends is notable. The work of Pratap et al. related to using a strain intensity factor instead of stress intensity factor is used.

1.2.2   Problem Statement

The myriad applications of SFRP have increased the challenges includes the stress behaviours in the structures where load-bearing components, like fibres, are uneven in length and orientation with loading direction. Stress behaviour in and at the tip of the fibre is extensively studied by the investigators. In these models, they have considered the fibres as inclusions and modelled them as rigid bodies. The study shows that there are singularities present at the tip of fibres. Also, the imperfections like voids are significant to study especially when there already a singular stress field is present. Hence the present study deals with the same kind of problem but on a simpler level. In this study, the interaction of rigid line inclusion and a two-dimensional circular void is being studied. Hence the problem is modelled as a rigid line inclusion and a hole. To quantify the singularities at the fibre end, strain intensity factor, K_I^ϵ, is used instead of stress intensity factor. The variation
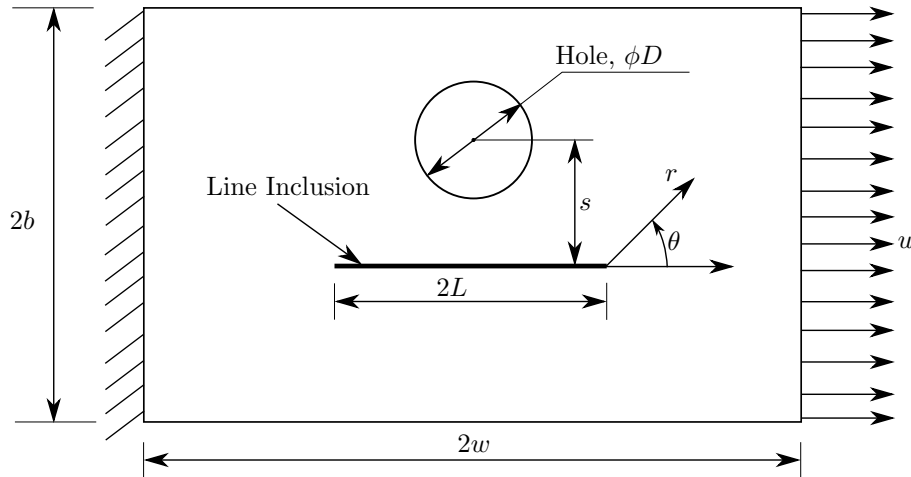
Figure 1.3: A schematic of the rigid line inclusion with a hole embedded in an infinite elastic matrix subjected to a loading.

of strain intensity factor with respect to three parameters, namely diameter of a hole, length of the inclusion and distance between the inclusion and a hole is planned to study. Fig. 1.3 shows schematic of rigid line inclusion with a hole embedded in an infinite elastic matrix subjected to a tensile loading.

In the first phase of the project, numerical investigation for strain intensity factor using commercial analysis software ABAQUS 6.14 is studied. The analysis is carried out in an automated manner with written ABAQUS Python Scripting. The numerical method used to calculate strain intensity factor is adopted from Patil P. et al. [20]. These numerical results are to be validated with Photoelasticity results. The specimens for the photoelasticity experiments have been prepared.

1.3   Scope and motivation

Due to the production process, materials limitations, etc., voids formation is inevitable in the composite materials. In the fabrication process, air entraps in the laminates and unable to move out. After completion of the fabrication process, this entrapped air creates voids in composites. Researchers studied many affecting factors on void formation which includes resin pouring temperature, curing temperature, vacuum pressure, resin viscosity, etc. These factors also affect the void geometry. Also, a much study has been devoted to the reduction of void formation. It is also known that the voids also greatly affect the mechanical properties of composites. A much of the study has been carried out for studying the effects of voids for continuous-fibre-reinforced-polymers but not for the short-fibre-reinforced-polymers which have different stress behaviour when loaded, compared to that of continuous fibre composites. From the literature, we know the that for short fibre composites, there is singular fields present at fibre ends. The present study is devoted to studying the effects of voids on the fibre end stress singularity in case of short-fibre-reinforced-polymers.

A numerical model is created in which the problem is modelled for the 2D case. In this 2D numerical model, fibres are modelled as a rigid line inclusion, and voids are modelled as a hole embedded in an elastic matrix. To get the elastic stress and strain field for present problem, the approach of Pratap et al. [20] is adopted. The strain intensity factor, K_I^ϵ, at the tip of rigid line inclusion is estimated for different configuration of the problem. The strain intensity factor variation with three geometric parameters is studied, viz. inclusion length, the diameter of the hole and distance between line inclusion and hole centre. The reciprocal theorem is used to find the strain intensity factor requires the stress field data which is obtained from finite element analysis(FEA). Further, this numerical model is validated using the Digital photoelasticity technique. The fringe contours from FEA has reconstructed using the multi-parameter equation derived for the present problem. These fringe contours are then compared with that of Photoelasticity experiment. For strain intensity factor estimation, there are several optical techniques like Moiré interferometry, speckle interferometry, holographic interferometry, photoelasticity, digital image correlation. But most of the interferometric techniques are sensitive to vibration. And among these experimental techniques photoelasticity technique is a sophisticated technique which gives rich field data for complex geometry and the vibration sensitivity can be removed with some special arrangements of its optical components.

1.4 Objectives

- Implementation of Adaptive Quality Guided Algorithm (AQGPU) using ten-step Phase Shifting Technique (PST) to get whole field fringe order data and isoclinic data from digital photoelasticity.

- Implementation of the numerical and experimental methods to estimate the strain intensity factor for rigid line inclusion and hole problem.

- Development and implementation an over a deterministic linear least square approach to solving multi-parameter stress field equation for rigid line inclusion problem.

- Study the effect of voids on the stress singularity at the fibre end in case of short-fibre-reinforced-polymers.

1.5 Thesis layout

Chapter 1 talks about defects in composite materials with the major discussion about voids formation and its effects material properties. Also, a brief review of literature work on defects studies, use of digital photoelasticity for fracture studies. This chapter also discusses the problem definition for this thesis. In the end, scope and motivation and objectives for this work are discussed.

Chapter 2 discusses the implementation of AQGUP algorithm using the ten-step PST to get the whole field fringe order data and isoclinic data. These algorithms are then verified for the disc under diametral compression problem.

Chapter 3 discusses the evaluation of strain intensity factor by linear least squares approaches using digital photoelasticity technique. To use this experimental technique, the multi-parameter stress field equation for the rigid line inclusion are derived. The specimen preparation and experimentation procedure is then discussed. Further, the results for the rigid line inclusion and hole problem are discussed.

Chapter 4 discusses the numerical procedure to estimate the strain intensity factor, K_I^ϵ, for rigid line inclusion. This method is then extended to estimate strain intensity factor for the rigid line inclusion and hole problem. Further, the numerical and experimental results for a present problem are compared quantitatively and qualitatively as well.

Chapter 5 states the conclusion and recommendation for future work.

Chapter 2

Whole field isochromatic parameter estimation using digital photoelasticity

2.1 Introduction

Centuries of research have given us different type experimental techniques for design analysis which comes handy when verifying and confirming the analytical and numerical results such as holographic interferometry, Moiré interferometry, electronic-speckle-pattern interferometry, coherent gradient sensing, the method of caustics, photoelasticity, digital image correlation (DIC). Holography and other interferometric techniques are very sensitive to vibration and require a coherent light source and also complex setup. Among these techniques, photoelasticity gives the rich whole field data even for complex problems, and the setup is simple optical elements.

Photoelasticity is non-contact type, optical and whole field technique for the experimental stress analysis. Photoelasticity techniques are used for a variety of stress analysis, design and also verification of numerical methods such as finite elements or boundary elements. The basic principle of this technique is when a certain material stressed, the property of birefringence induces in the stressed components. Many transparent materials exhibit this property. For the transparent materials, transmission photoelasticity can be used, and for non-transparent or opaque materials such as metals, reflection photoelasticity can be used. Photoelasticity is very popular for the two-dimensional plane problem but also it can be extended for three-dimensional problems. In early days, it was used to study stress concentration factor for complex structural shape for both two and three dimensional. Birefringence is the property of the material in which material will have two refractive indices in the two mutually perpendicular directions. When materials with birefringence property are stressed, it shows the fringe contours. These fringe contours are related to the principal stress difference in the plane normal to the propagation of light source. In the early days, the fringe data is obtained manually which limits its applications. With inventions of the computers, it is possible to do image processing and to automate the procedure to capture isoclinic and isochromatics. The recent developments in digital image processing have given birth to a separate branch of photoelasticity called

Digital Photoelasticity.

This chapter discusses the estimation of a whole field digital photoelastic parameter. Ten-step phase shifting technique is used for data acquisition in order to minimise the vibration, optical elements misalignment errors. Further, from this acquired data, wrapped isochromatic data with ambiguous zones and wrapped isoclinic data with inconsistent zones is obtained. This wrapped isoclinic data is then unwrapped to get whole field isoclinic data without inconsistent zones using Adaptive Quality Guided Algorithm (AQGUP). The same algorithm is then applied to get whole field isochromatic data without ambiguous zones. This algorithm is verified by applying to standard disc under diametral compression problem.

2.2   Whole field digital photoelastic parameter estimation

In photoelasticity, we get whole field data such as principle stress difference and principal stress direction orientation. Remember, the upcoming discussion is about two-dimensional photoelasticity, for three-dimensional photoelasticity some discussion point might be different. In photoelasticity technique, two type fringe contours can be obtained, namely isochromatics and isoclinic as shown in fig. 2.1. Isochromatics contours corresponds to principle stress difference and isoclinics corresponds
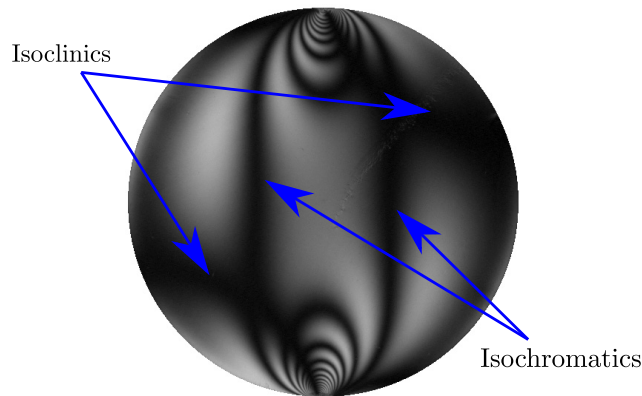
Figure 2.1: A plane polariscope image of a disk under diametric compression showing both isoclinic and isochromatic fringe contours.

to principle stress direction. At the particular isochromatic fringe, the principal stress difference is same throughout the fringe, but the principal stress direction may be different and vice-versa. In the Fig. 2.1, the isochromatic or fringe order data is varying from zero to one which is discrete. And the isoclinic fringe in same figure is corresponds to some angle depending upon arrangement of optical elements. Hence to get whole field data, we generally use different techniques which essentially requires grabbing more images at certain optical arrangements and then processing them.

The data collection using charge-coupled device (CCD) cameras which records the intensity data is became simpler. The techniques are broadly classified into spatial domain and frequency domain methods. Phase-shifting techniques (PST), polarization stepping techniques and load stepping come under spatial domain methods. Spatial domain methods require the smaller number of images to be recorded (from three to ten in most cases). Further, they are computationally very fast. Hence, they are considered for whole field isochromatic parameter estimation.

2.2.1 Data acquisition in digital photoelasticity

Phase shifting technique is most widely used method to get isoclinic and isochromatic values at each point in the model domain. In the phase shifting technique, a few images are recorded corresponding to different angular arrangements of the optical elements used [29]. As each is captured at the different optical arrangement, hence a phase of contours is shifted, therefore called as phase shifting technique (PST). There are many techniques to get whole field data from photoelasticity such as half fringe photoelasticity, three fringe photoelasticity, etc.

Recently, Ramji and Prasath [30] recommended the use of ten-step phase shifting method for manual polariscope with digital photoelastic applications. It has been verified that using ten-step gives the isoclinic and isochromatic very greater accuracy as compared to other phase shifting methods even in the presence of the small optical misalignment. Fig. 2.2 shows the optical element arrangement for photoelasticity technique. The light source used can be a white light or monochromatic light source. When a white light source is a coloured fringe pattern is produced and similarly when monochromatic light is used a white and dark colour fringe patterns produced.
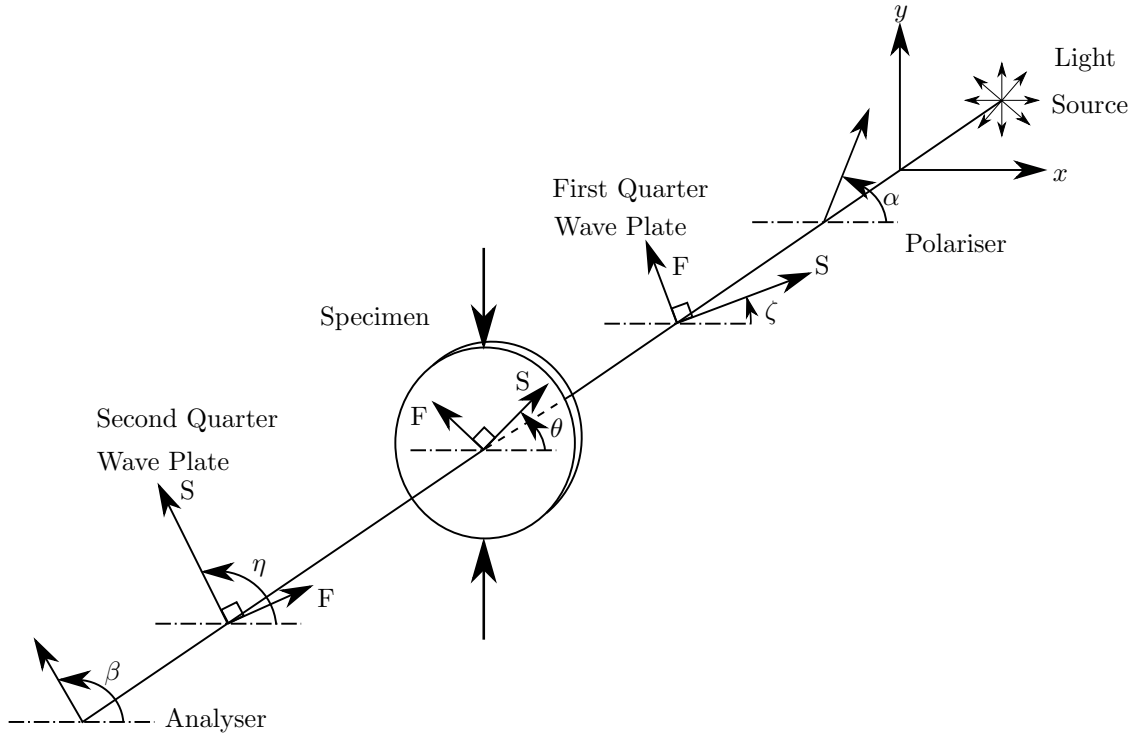
Figure 2.2: Generic optical element arrangement for photoelasticity technique set-up.

The orientation angles used with respect horizontal for different optical elements in the above Fig. 2.2 are:

α = Orientation angle of Polariser,

ζ = Orientation angle of First Quarter wave plate,

η = Orientation angle of Second Quarter wave plate,

β = Orientation angle of Analyser and

θ = Orientation angle of principal stress direction.

Note that the angles, α, ζ, η, β and θ represents orientation of slow axis of the respective optical element. In the Fig. 2.2, the F and S indicate the fast and slow axis of polarised light respectively. The quarter-wave plates are used to obtain a phase difference of quarter of the wavelength, $\lambda_a/4$. But this phase difference obtained by quarter wave plate depends on the wavelength of light source used, hence for a white light source, the quarter wave plate simply acts as a retarder. Therefore, these optical elements can be used for only one type of light source.

2.2.2   Ten-step phase shifting technique

Ten-step PST gives the most accurate whole field data than any other technique. Hence we exercise this technique in our work. For the ten-step PST, the optical arrangements for different optical elements used are given in Table 2.1. In the above Table 2.1, I_b is surrounding light intensity, I_a is

Table 2.1: Ten-step method: Polariscope arrangements and intensity equations for isoclinic and isochromatics evaluation

No.	α	ζ	η	β	Intensity Equation
1.	$\pi/2$	-	-	0	$I_1 = I_b + I_a \sin^2(\frac{\delta}{2}) \sin^2 2\theta$
2.	$5\pi/8$	-	-	$\pi/8$	$I_2 = I_b + \frac{I_a}{2} \sin^2(\frac{\delta}{2})(1 - \sin 4\theta)$
3.	$3\pi/4$	-	-	$\pi/4$	$I_3 = I_b + I_a \sin^2(\frac{\delta}{2}) \cos^2 2\theta$
4.	$7\pi/8$	-	-	$3\pi/8$	$I_4 = I_b + \frac{I_a}{2} \sin^2(\frac{\delta}{2})(1 + \sin 4\theta)$
5.	$\pi/2$	$3\pi/4$	$\pi/4$	$\pi/2$	$I_5 = I_b + \frac{I_a}{2}(1 + \cos \delta)$
6.	$\pi/2$	$3\pi/4$	$\pi/4$	0	$I_6 = I_b + \frac{I_a}{2}(1 - \cos \delta)$
7.	$\pi/2$	$3\pi/4$	0	0	$I_7 = I_b + \frac{I_a}{2}(1 - \sin 2\theta \sin \delta)$
8.	$\pi/2$	$3\pi/4$	$\pi/4$	$\pi/4$	$I_8 = I_b + \frac{I_a}{2}(1 + \cos 2\theta \sin \delta)$
9.	$\pi/2$	$\pi/4$	0	0	$I_9 = I_b + \frac{I_a}{2}(1 + \sin 2\theta \sin \delta)$
10.	$\pi/2$	$\pi/4$	$3\pi/4$	$\pi/4$	$I_{10} = I_b + \frac{I_a}{2}(1 - \cos 2\theta \sin \delta)$

light intensity of light source, δ is phase retardation through the specimen and θ is principal stress orientation. The first four optical arrangements are called as Plane Polariscope, where the quarter wave plates are absent or optically effect made null by putting them align with the other optical elements, viz. polariser and analyser. In these arrangements, we can see both fringe contours, viz. isoclinics and isochromatics. The remaining six optical arrangements are called Circular Polariscope, where quarter wave plates are arranged such a way that the light coming out of first quarter wave will be circularly polarized light and that of after second quarter wave plate light will be again plane polarized. In these arrangements, we can see only isochromatics fringe contours. Using above

different arrangements, the wrapped isoclinic and isochromatic values can be obtained as

$$\theta_c = \frac{1}{4} \tan^{-1}\left(\frac{I_4 - I_2}{I_3 - I_1}\right), \tag{2.1}$$

$$\delta_c = \tan^{-1}\left(\frac{(I_9 - I_7)\sin 2\theta + (I_8 - I_{10})\cos 2\theta}{I_5 - I_6}\right). \tag{2.2}$$

From equation 2.1, one can get the wrapped isoclinic phase map in the range $-\pi/4$ to $+\pi/4$ with inconsistent zone and it needs to be unwrapped. Later, the unwrapped isoclinic data is used for the isochromatic phase map generation as given in equation 2.2. Finally, the wrapped isochromatic phase map has to be unwrapped for getting the continuous fringe order.

2.3   Unwrapping of isoclinic phasemap

After grabbing the images and getting the wrapped isochromatic and isoclinic data, the next step is to get the continuous data. Hence, unwrapping of wrapped isoclinic and isochromatic is necessary, and so it is discussed next. The Fig. 2.3a shows the wrapped isoclinic phasemap with inconsistent zones for a disc under diametral compression problem and Fig. 2.4 shows the wrapped isochromatic phasemap with ambiguous zones for the same problem obtained using the wrapped isoclinic phasemap. In the above equation 2.2, θ is the isoclinic values at a point, and hence it is necessary to unwrap the isoclinic first then it to used for the unwrapping of isochromatics. When isoclinics
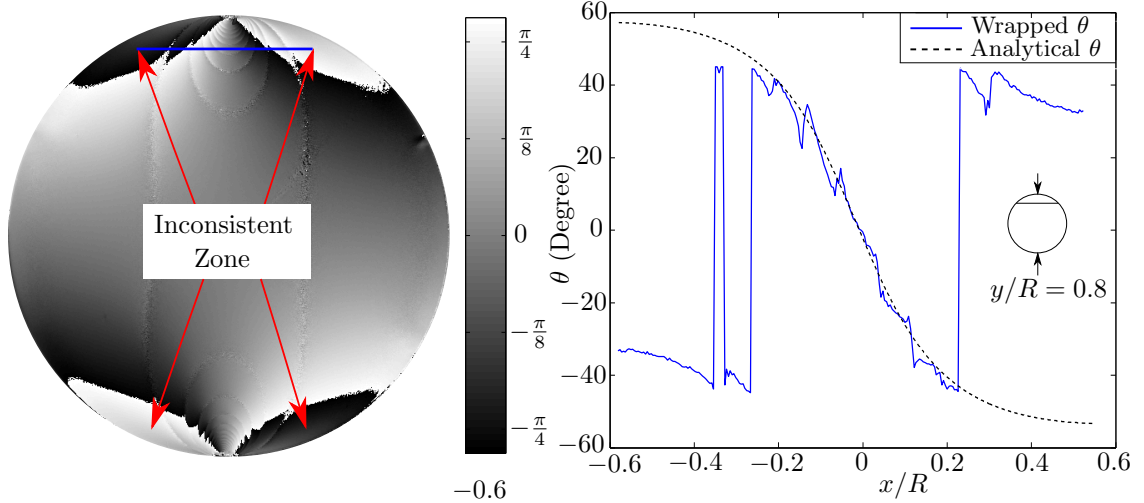
Figure 2.3: Isoclinic phasemap for disc under diametric compression (a) wrapped isoclinic phasemap with inconsistent zone (b) comparison of wrapped isoclinic with analytical obtained values along the line $y/R = 0.8$.

phasemap corresponds to only one of the principal stress direction, let's say, σ_1, we get phasemap without inconsistent zones. And when it corresponds to σ_2 for some region and σ_1 for another region, we get inconsistent zones in isoclinic phasemap. We know that the principal stresses, σ_1 and σ_2, are always perpendicular to each other. This means there is a jump of $\pi/2$ and hence the colour is jumped from white to black and vice-versa. One such example is shown in Fig. 2.3a where isoclinic

13
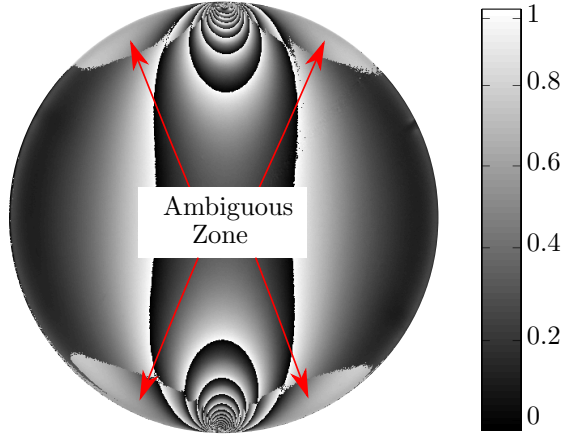
Figure 2.4: Wrapped isochromatic phasemap with ambiguous zones for disc under diametrical compression.

phasemap corresponds to σ_1 except in the inconsistent zone where it corresponds to σ_2. The jump of $\pi/2$ happens at the boundary of the inconsistent zone. This is shown in Fig. 2.3b, where $\pi/2$ jump present between wrapped and analytical isoclinics across the blue line shown in Fig. 2.3a. Hence to get a continuous unwrapped isoclinic, a constant value of $\pi/2$ has to add to the isoclinic values in the inconsistent zone. This process of unwrapping is called phase unwrapping of isoclinic phasemap.
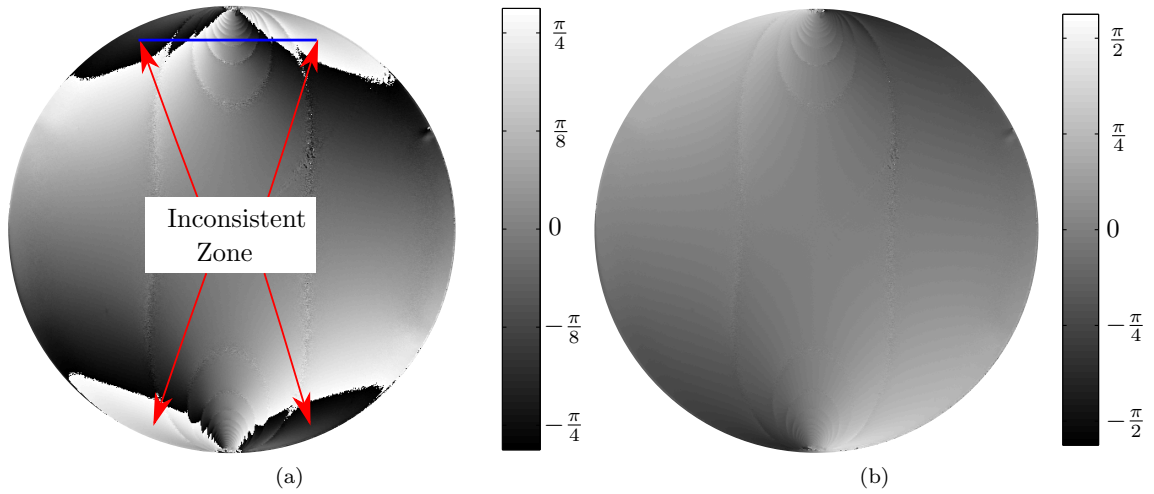
Figure 2.5: Isoclinic phasemap unwrapping for disc under diametric compression (a) wrapped isoclinic phasemap with inconsistent zone and (b) unwrapped isoclinic phasemap.

We know that, in the inconsistent zones, the isoclinics represents the principal direction of the other principal stress. This happens because the arctangent function returns the principal isoclinic value in the range $-\pi/4$ to $+\pi/4$, but physically the isoclinic value must be in the range $-\pi/2$ to $+\pi/2$. Hence, one supposed to unwrap the isoclinic phasemap to get them in the range $-\pi/2$ to $+\pi/2$ and this can be done by using the Adaptive Quality Guided (AQGUP) Algorithm as described in [31]. Figure 2.5 shows the wrapped and unwrapped isoclinic phasemaps for disc under diametral compression.

2.4 Unwrapping of isochromatics phasemap

From Eqn. 2.2, it clear that one needs to use the isoclinic phasemap to get isochromatic phasemap. Hence when we use unwrapped isoclinic phasemap data, we get isochromatic phasemap without ambiguous zones. In the non-ambiguous zone, the black to white colour transition is towards the loading point, but for an ambiguous zone, this is complete opposite which has transitioned from black to white towards the loading point. These isochromatic phasemap shows fractional fringes, and they are in order of $-\pi$ to $+\pi$. Before unwrapping of isochromatic, the obtained isochromatic phasemap need to convert in the range of 0 to 2π. It can be done as follows

$$\delta = \begin{cases} \delta_c, & \text{for } \delta_c > 0, \\ 2\pi + \delta_c, & \text{for } \delta_c \leq 0. \end{cases} \tag{2.3}$$

The wrapped isochromatic phasemap is then unwrapped in the same manner as that of isoclinic phasemap. In the start isochromatic unwrapping process, the seed point needs to be selected and corresponding fringe order has to be given as input. The unwrapped isochromatic phasemap of the disc under diametral compression is shown in the Fig. 2.6.

(a)   (b)
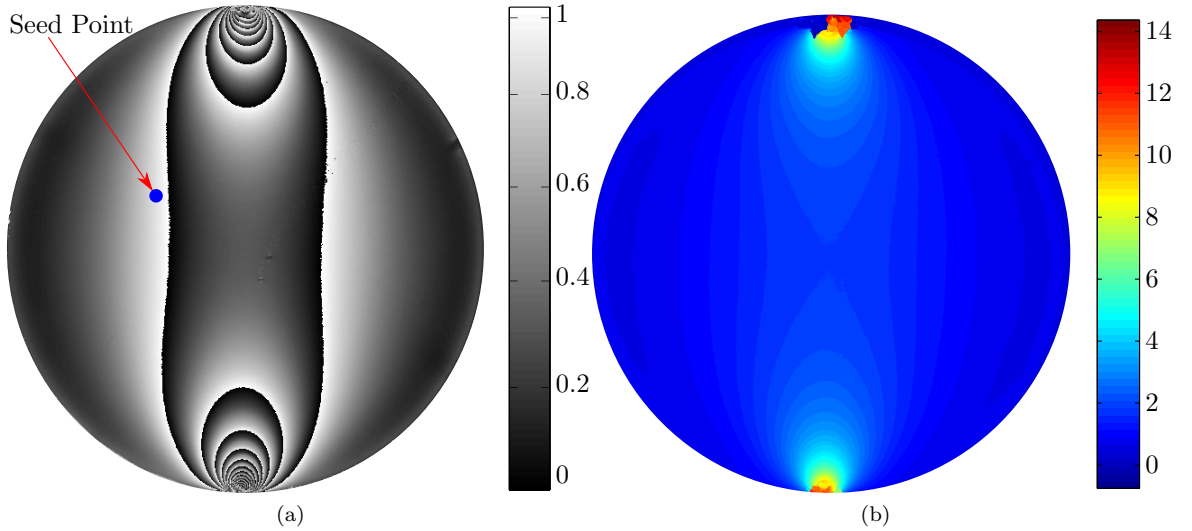
Figure 2.6: Isochromatic phasemap unwrapping for disc under diametric compression (a) wrapped isochromatic phasemap with seed point and (b) unwrapped Isochromatic phasemap.

2.5 Specimen fabrication and experimental procedure

The disc under diametral compression test is a very standard exercise to get material fringe value from the photoelasticity experiment. A disc specimen is prepared using simple casting process in a closed mould. The disc is cast using resin Epofine-221 and hardener Finehard-1842 mixed in the ratio 100:40 by weight. At first resin and hardener are taken in clean, separate beakers in sufficient quantity. Heat the resin and hardener in hot water, so the air and moisture in it get evaporated. After it gets cooled, mix it and stir slowly. While stirring, care should be taken that no air bubbles

formed and also dust should enter. After complete mixing, keep the mixture at a steady temperature to cure normally for 48hr. Then check the specimen for any residual stresses using the polariscope. Then machine the specimen for the required dimensions, for disc its 60mm diameter.

ϕ 60

All dimensions are in mm
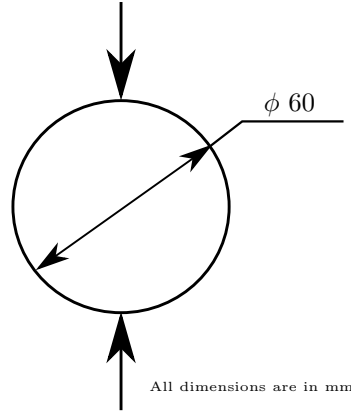
Figure 2.7: Disc specimen for digital photoelasticity experiment

The images are captured using the BASLER monochrome CCD camera which has a spatial resolution of 1392 × 1040 pixels for different optical arrangements as mentioned in the Table 2.1. The specimen is loaded using a 10kN Instron Machine.

2.6 Results

2.6.1 Disc under diametrical compression

A disc under diametrical compression is used to exercise the use of AQGUP algorithm and also the same specimen is used for the estimation of material fringe value, F_σ. A disc specimen is prepared for photoelasticity experiments as shown in Fig. 2.7. Ten-step images are captured as specified in the Table 2.1. For the unwrapping, first the quality map is generated and to start the unwrapping of isoclinic phasemap by AQGUP algorithm, the seed point is selected in the consistent zone as shown in the Fig. 2.8a. Fig. 2.8b shows the unwrapped isoclinic phasemap obtained using AQGPU.

The wrapped isochromatic phasemap without ambiguous zone is obtained using unwrapped isoclinic phasemap values as shown in Fig. 2.8c. To ensure the correctness of the isochromatic data, it is then compared with dark field photoelastic image obtained from polariscope. This image is obtained using the six numbered optical arrangement specified in the Table. 2.1. This isochromatic data is ranged from 0 to 1. Hence, to get continuous isochromatic value over the entire domain, unwrapping of isochromatic phasemap is done using AQGPU. Here, to start the unwrapping of isochromatic phasemap, a seed point (N = 1) is selected as shown in Fig. 2.8c and corresponding fringe order is given as input. The unwrapped isochromatic phasemap is shown in Fig. 2.8d.

Further, the unwrapped isoclinic and isochromatic data is compared with analytical data. Fig. 2.9 shows the comparison of isoclinic values with the analytical values along the line $y/R = 0.8$. Also in Fig. 2.10 shows the comparison of isochromatic values with the analytical values along the line $y/R = 0.8$.
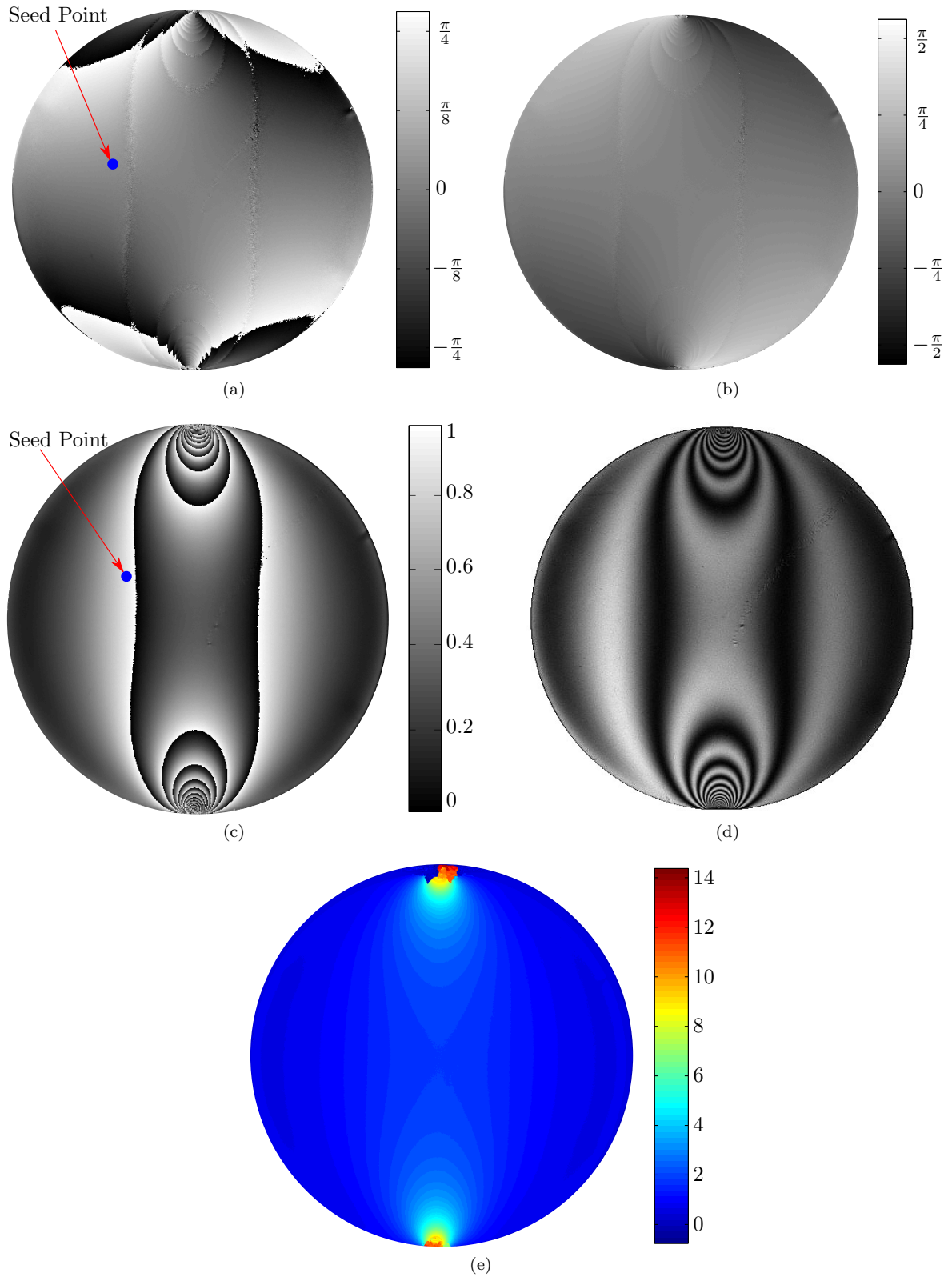
Figure 2.8: Isoclinic and isochromatic phasemap for disc under diametral compression (a) wrapped isoclinic phasemap, (b) unwrapped isoclinic phasemap, (c) wrapped isochromatic phasemap (d) dark field photoelastic image and (e) unwrapped isochromatic phasemap
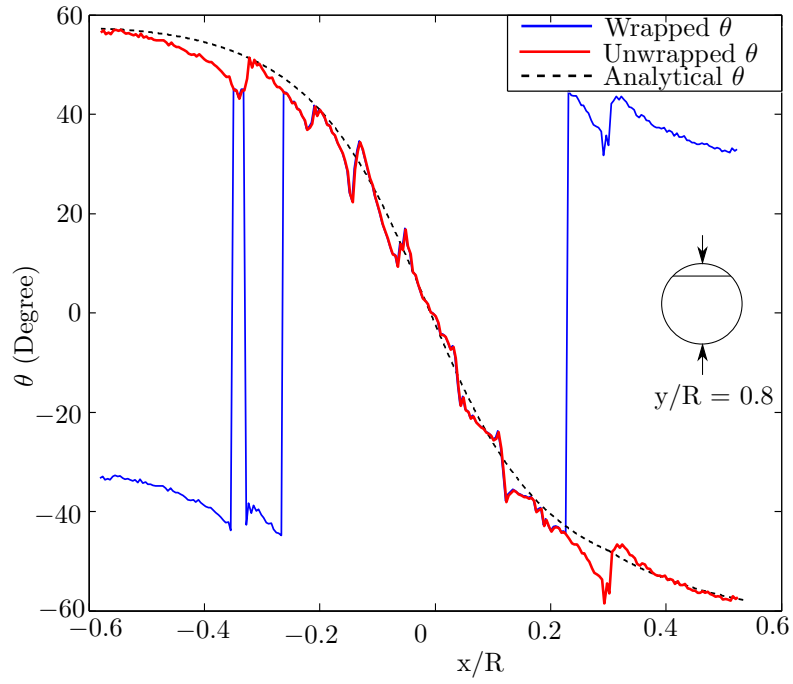
Figure 2.9: Verifying the isoclinic unwrapping using analytically generated isoclinic value along the line $y/R = 0.8$ for disc under diametral compression problem.
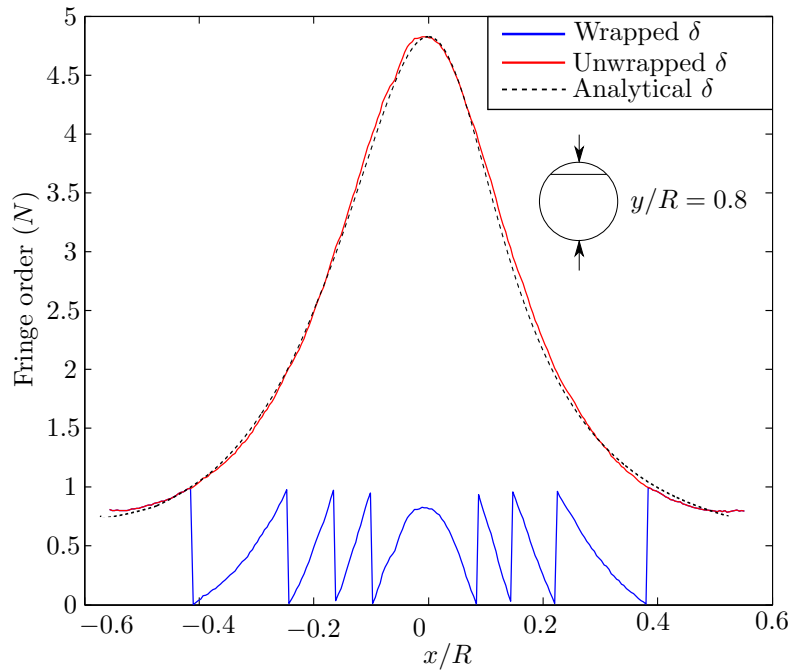
Figure 2.10: Verifying the isochromatic unwrapping using analytically generated fringe values along $y/R = 0.8$ for disc under diametral compression problem.

Chapter 3

Strain intensity factor estimation by linear least squares approach using digital photoelasticity technique

3.1 Introduction

Defects like, cracks, inclusions, etc., are, in some way, responsible for stress concentration and magnifies the load locally which initiates cracks and leads to failures. The presence of crack alters the stress and strain field around the crack-tip. Also similar is the case of rigid line inclusions. In the fracture studies of crack and line inclusions, the stress intensity factor (SIF) expresses the strength of singular elastic stress field and also characterise near-tip stress field. The critical value of SIF decides the initiation of cracks growth and ultimate failure. SIF can be estimated using analytical, numerical, or experimental techniques. However, the analytical techniques are confined to the simple configurations and boundary conditions. For complex configurations, SIF needs to be extracted using either numerical or experimental method. The multi-parameter stress field equations for crack proposed by Atluri and Kobayashi is the extension of William's eigen function expansion. An over-deterministic least squares technique is proposed to evaluate the mixed-mode stress field parameters using multi-parameter stress field equations by the experimental technique called photoelasticity [32].

Foreign materials like inclusions locked inside the parent materials during material formation or manufacturing process which acts as a stress riser and they are different in geometries also. While studying these defects, inclusions are considered as infinite strength or very high strength materials compared to parent materials. In case short-fibre-reinforced-polymers (SFRP), fibre length, its orientation and distribution is not specific. In SFRP, the load is transferred from matrix to fibre, and this can be done through fibre end and its cylindrical surface. But due to the shorter length, its cylindrical area is very small, and hence most of the load transfer happens through the fibre end which creates very high stress concentration at it as the thickness or diameter of the fibre is again

very small compared to its length. Hence while solving the problems in SFRP, it is a fundamental ideology to consider fibres as rigid line inclusions. In the literature, there are solutions available for rigid line inclusion solved using different methods and techniques. In these researches, the stress intensity factor is used to predict the strength of the singular elastic stress field. But the stress intensity factor, in case of inclusion problems, depends on materials properties. Hence, Pratap P et al. [20] used a strain intensity factor, K_I^ϵ, for defining the strength of the singular stress field and also characterise near-tip stress field. strain intensity factor is independent of the material properties. Hence it is more suitable for use.

In past researches, for estimation of fracture parameter such stress intensity factor non-contact optical methods such as holographic interferometry, Moiré interferometry, electronic-speckle-pattern interferometry, coherent gradient sensing, the method of caustics, photoelasticity, digital image correlation (DIC) are used. Holography and other interferometric techniques are very sensitive to vibration and require a coherent light source and also complex setup. Among these techniques, photoelasticity gives the rich whole field data even for complex problems, and the setup is simple optical elements. Hence, photoelasticity technique is exercised here.

In this chapter, the procedure of estimation strain intensity factor using digital photoelasticity technique is discussed. The fracture parameters such as strain intensity factor are evaluated by finding coefficients of a curve fitted multi-parameter stress field equation over the experimental isochromatic data surrounding inclusion-tip. The objective function is defined as the square of the error between experimental and reconstructed fringe order obtained from the multi-parameter equation. This objective function is then minimised to get the coefficient values using non-linear over deterministic technique where an initial guess of the coefficient has to be given. Hence, a solution is not straight forward and sometimes doesn't converge easily especially in the case of mixed mode problems. The extracted coefficients of the multi-parameter equation are related to the inclusion-tip strain intensity factor parameter. Further, finding the exact location of the inclusion-tip is not possible using the above approach, and hence it always results in an uncertainty of the extracted fracture parameters. It is not the fullest extent of use of photoelasticity when we use only isochromatic data for estimation of strain intensity factor. Therefore, in this work, the availability pixel-wise isochromatic and isoclinic data has enabled us to convert the non-linear regression problem into a linear regression problem for unknown coefficients. The linear regression problem is solved over the chosen grid around crack tip by an over deterministic least square approach. This approach ensures fast and accurate determination of crack tip fracture parameters including the inclusion-tip location.

Further, in the chapter, ten-step PST is used to the whole field is isochromatic and isoclinic phasemap for rigid line inclusion and hole problem. Then, wrapped phasemaps are unwrapped using adaptive quality-guided phase unwrapping (AQGPU) algorithm [31]. This unwrapped data is used to find strain intensity factor by solving the multi-parameter stress field equation in an over deterministic linear least square approach. We studied the rigid line inclusion with a hole problem subjected tensile loading.

3.1.1 Strain intensity factor

In the literature, for the rigid line inclusion problems, stress intensity factor is used to quantify the strength of singular stress field near the inclusion-tip. But this stress intensity factor depends on

the materials properties such as Poisson's ratio, ν. Hence there is a need for defining the governing factor which is independent of material properties. We know, the asymptotic stress and strain field at inclusion tip solutions derived given as [20],

$$\sigma_{11} = \frac{2\mu\epsilon_{11}^\infty}{\kappa}\left(\frac{l}{2r}\right)^{1/2}\cos\left(\frac{\theta}{2}\right)\left[1 + \frac{1+\kappa}{2} - \sin\left(\frac{\theta}{2}\right)\sin\left(\frac{3\theta}{2}\right)\right], \quad (3.1)$$

$$\sigma_{22} = \frac{2\mu\epsilon_{11}^\infty}{\kappa}\left(\frac{l}{2r}\right)^{1/2}\cos\left(\frac{\theta}{2}\right)\left[1 - \frac{1+\kappa}{2} + \sin\left(\frac{\theta}{2}\right)\sin\left(\frac{3\theta}{2}\right)\right], \quad (3.2)$$

$$\sigma_{12} = \frac{2\mu\epsilon_{11}^\infty}{\kappa}\left(\frac{l}{2r}\right)^{1/2}\sin\left(\frac{\theta}{2}\right)\left[\frac{1+\kappa}{2} + \cos\left(\frac{\theta}{2}\right)\cos\left(\frac{3\theta}{2}\right)\right], \quad (3.3)$$

$$\epsilon_{11} = \frac{\epsilon_{11}^\infty}{\kappa}\left(\frac{l}{2r}\right)^{1/2}\cos\left(\frac{\theta}{2}\right)\left[\kappa - \sin\left(\frac{\theta}{2}\right)\sin\left(\frac{3\theta}{2}\right)\right], \quad (3.4)$$

$$\epsilon_{22} = -\frac{\epsilon_{11}^\infty}{\kappa}\left(\frac{l}{2r}\right)^{1/2}\cos\left(\frac{\theta}{2}\right)\left[1 - \sin\left(\frac{\theta}{2}\right)\sin\left(\frac{3\theta}{2}\right)\right], \quad (3.5)$$

$$\epsilon_{12} = \frac{\epsilon_{11}^\infty}{\kappa}\left(\frac{l}{2r}\right)^{1/2}\sin\left(\frac{\theta}{2}\right)\left[\frac{1+\kappa}{2} + \cos\left(\frac{\theta}{2}\right)\cos\left(\frac{3\theta}{2}\right)\right]. \quad (3.6)$$

We know the stress intensity factor can be defined for this situation as [19],

$$K_I = \lim_{r\to 0}\sigma_{22}(r, \theta = 0°)\sqrt{2\pi r}, \quad (3.7)$$

which gives the form using above Eqns. 3.3 as,

$$K_I = \mu\epsilon_{11}^\infty\frac{1-\kappa}{\kappa}\sqrt{\pi l}, \quad (3.8)$$

where ϵ_{11}^∞ is the applied strain at infinity in 1-direction. From the Eqn. 3.8, we can see that under the plane strain condition, for incompressibility, i.e. for $\kappa = 1$, or $\nu = 1/2$, this equation is not behaving well. Also, the very definition of stress intensity to be the function of loading condition and not the material properties is violating here. Hence, on inspecting above equation of the stress and strain fields, the strain intensity factor instead of stress intensity factor is defined as follows,

$$K_I^\epsilon = \lim_{r\to 0}\epsilon_{11}(r, \theta = 0°)\sqrt{2\pi r}, \quad (3.9)$$

which gives the form using above Eqns. 3.6 as,

$$K_I^\epsilon = \epsilon_{11}^\infty\sqrt{\pi l}, \quad (3.10)$$

which is completely independent on material properties. The following salient features can be noted in the solution as mentioned above. (1) The order of stress singularity for the inclusion tip is the same as that of a crack tip which is 1/2. (2) The asymptotic stress field is always symmetric and depends only on the applied normal strain in the direction of the inclusion. This is in contrast to the asymptotic field near a crack tip, where the stress field can also be antisymmetric due to a mode II loading. Consequently, for planar loading case, only a single strain intensity factor definition is

applicable for the inclusion problem. (3) The strain intensity factor is independent of the material properties of the matrix material.

3.2 Multi-parameter equations for rigid line inclusion embedded in an elastic matrix

Multi-parameter stress field equations are the sophisticated equations to calculated fracture parameters like stress intensity factor. Also, these equations can be used to find stress intensity factor from experimental isochromatic and isoclinics data surrounding the crack-tip. Multi-parameter equations are available for crack problems for mixed mode case, developed by Atluri and Kobayashi which is simplified solution version of William's eigen function approach. But for rigid line inclusion, these equations are not available. Hence herein, we choose to derive the multi-parameter stress field equation for rigid line inclusion. Later, we use these equations to estimate strain intensity factor for the inclusion-hole problem.

3.2.1 William's eigen function approach

William considered a stress function for the singular problems as,

$$\phi = f_1(r) \ f_2(\theta) = r^{(\lambda+1)} f(\theta), \tag{3.11}$$

where (r, θ) are the polar coordinates centred at the crack-tip or inclusion-tip and λ is a real integer. From the observation, negative values of λ are neglected since they produce infinite displacement at the crack-tip or inclusion-tip and also $\lambda = 0$ excluded.

Now, we just need to find the eigen function, ϕ, which is a solution to the stated problem. But, to be the correct solution to the problem, the eigen function, ϕ, has to satisfy the biharmonic equation in polar coordinates, as

$$\nabla^2 \nabla^2 \phi = \left(\frac{\partial^2}{\partial r^2} + \frac{1}{r} \frac{\partial}{\partial r} + \frac{1}{r^2} \frac{\partial^2}{\partial \theta^2} \right) \left(\frac{\partial^2 \phi}{\partial r^2} + \frac{1}{r} \frac{\partial \phi}{\partial r} + \frac{1}{r^2} \frac{\partial^2 \phi}{\partial \theta^2} \right), \tag{3.12}$$

and the appropriate boundary conditions. Put the Eqn. 3.11 in Eqn. 3.12, we get,

$$\nabla^2 \nabla^2 \phi = \frac{d^4 f}{d\theta^4} + 2(\lambda^2 + 1) \frac{d^2 f}{d\theta^2} + (\lambda^2 - 1)^2 f = 0. \tag{3.13}$$

In the above Eqn. 3.13, note that λ is the eigen value and f is the eigen function. On solving this equation for f, we get,

$$f = f_1 + f_2, \tag{3.14}$$

where,

$$f_1 = A \cos[(\lambda - 1)\theta] + B \cos[(\lambda + 1)\theta], \tag{3.14a}$$

$$f_2 = C \sin[(\lambda - 1)\theta] + D \sin[(\lambda + 1)\theta]. \tag{3.14b}$$
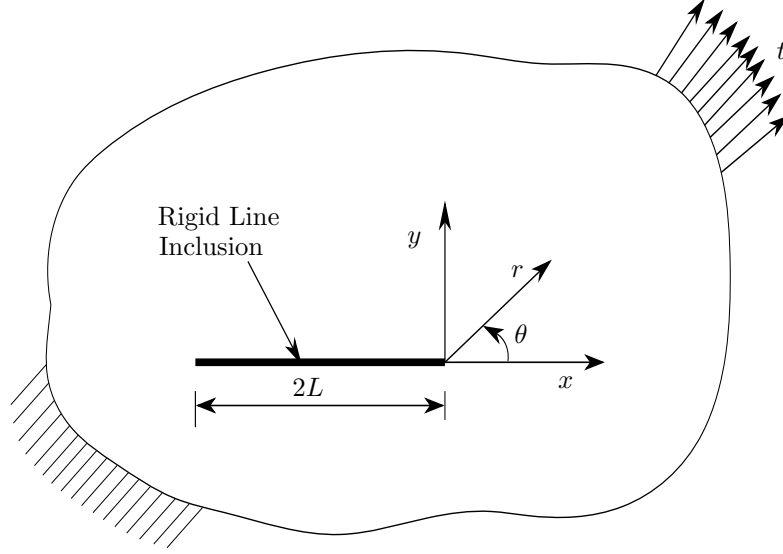
Figure 3.1: A schematic showing rigid line inclusion embedded in an elastic matrix with the origin at inclusion tip

The Eqn. 3.14a is the symmetric part corresponds to opening mode(Mode I) and the Eqn. 3.14b is the anti-symmetric part corresponds to sliding mode(Mode II).

Once we know eigen function, ϕ, we can find stress field using following relations in polar coordinates,

$$\sigma_{rr} = \frac{1}{r}\frac{\partial \phi}{\partial r} + \frac{1}{r^2}\frac{\partial^2 \phi}{\partial \theta^2}, \tag{3.15a}$$

$$\sigma_{\theta\theta} = \frac{\partial^2 \phi}{\partial r^2}, \tag{3.15b}$$

$$\sigma_{r\theta} = \frac{1}{r^2}\frac{\partial \phi}{\partial \theta} - \frac{1}{r}\frac{\partial^2 \phi}{\partial r \partial \theta}. \tag{3.15c}$$

3.2.2 Multi-parameter equations for rigid line inclusion

Consider a polar coordinate system (r, θ) and its origin at the tip inclusion as shown in Fig. 3.1. The problem definition is shown in the Fig. 3.1.

Now, assume a general form of eigen function for a singular problems,

$$\phi = r^{(\lambda+1)}\Big\{A\cos[(\lambda-1)\theta] + B\cos[(\lambda+1)\theta] + C\sin[(\lambda-1)\theta] + D\sin[(\lambda+1)\theta]\Big\}. \tag{3.16}$$

In the above equation 3.16, the first two terms denote symmetric parts of the eigen function, and last two terms denote anti-symmetric parts of the eigen function. Hence we can write symmetric and anti-symmetric parts separately as,

$$\phi = \phi_s + \phi_{as}, \tag{3.17}$$

and also we can solve them separately.

Part - I: Symmetric part

Lets consider the symmetric part of Eqn. 3.16, as

$$\phi_s = r^{(\lambda+1)}\Big\{A\cos[(\lambda-1)\theta] + B\cos[(\lambda+1)\theta]\Big\}. \tag{3.18}$$

Using the Eqn. 3.15 and Eqn. 3.18, we get,

$$\sigma_{rr} = -\lambda r^{(\lambda-1)}\Big\{A(\lambda-3)\cos[(\lambda-1)\theta] + B(\lambda+1)\cos[(\lambda+1)\theta]\Big\}, \tag{3.19a}$$

$$\sigma_{\theta\theta} = \lambda(\lambda+1)r^{(\lambda-1)}\Big\{A\cos[(\lambda-1)\theta] + B\cos[(\lambda+1)\theta]\Big\}, \tag{3.19b}$$

$$\sigma_{r\theta} = \lambda r^{(\lambda-1)}\Big\{A(\lambda-1)\sin[(\lambda-1)\theta] + B(\lambda+1)\sin[(\lambda+1)\theta]\Big\}. \tag{3.19c}$$

Now, to get whole stress field for rigid line inclusion problem, we need to find the constants in the Eqn. 3.19, which can be done by applying the boundary conditions. Boundary conditions for the rigid line inclusion problems can be defined in polar coordinates, as,

$$u_r = 0, \quad \text{at} \quad \theta = \pm\pi, \quad \text{and}$$
$$u_\theta = 0, \quad \text{at} \quad \theta = \pm\pi. \tag{3.20}$$

Now to apply the boundary conditions, we need displacement field solution for the present problem. To get displacement field solution corresponding to the specified symmetric eigen function, ϕ_s, in Eqn. 3.18, we use Michell's solutions, as given below,

$$2\mu u_r = r^\lambda\Big\{A(\kappa-\lambda)\cos[(\lambda-1)\theta] - B(\lambda+1)\cos[(\lambda+1)\theta]\Big\}, \tag{3.21}$$

$$2\mu u_\theta = r^\lambda\Big\{A(\kappa+\lambda)\sin[(\lambda-1)\theta] + B(\lambda+1)\sin[(\lambda+1)\theta]\Big\} \tag{3.22}$$

Applying the boundary conditions as denoted in Eqn. 3.20, we get,

$$A(\kappa-\lambda)\cos[(\lambda-1)\pi] - B(\lambda+1)\cos[(\lambda+1)\pi] = 0$$
$$A(\kappa+\lambda)\sin[(\lambda-1)\pi] + B(\lambda+1)\sin[(\lambda+1)\pi] = 0.$$

On using *sin* and *cos* identities and simplifying, above equation becomes,

$$[-A(\kappa-\lambda) + B(\lambda+1)]\cos(\pi\lambda) = 0 \tag{3.23}$$
$$[A(\kappa+\lambda) + B(\lambda+1)]\sin(\pi\lambda) = 0. \tag{3.24}$$

From Eqn. 3.23, we get values of λ as,

$$\cos(\pi\lambda) = 0 \quad \Rightarrow \quad \lambda = \pm\frac{1}{2}, \pm\frac{3}{2}, \pm\frac{5}{2}, \pm\frac{7}{2}..., \text{and so on,}$$

Now from Eqn. 3.24, we get relation in constants as,

$$B = -\frac{\kappa+\lambda}{\lambda+1}A \tag{3.25}$$

24

Now, from Eqn. 3.24, we get values of λ as,

$$\sin(\pi\lambda) = 0 \quad \Rightarrow \quad \lambda = 0, \pm 1, \pm 2, \pm 3, \pm 4..., \text{and so on,}$$

Now from Eqn. 3.23, we get relation in constants as,

$$B = \frac{\kappa - \lambda}{\lambda + 1} A \tag{3.26}$$

Consider $\lambda = \frac{n}{2}$, where, n is positive integer, and combining the two relations from Eqn. 3.25 and 3.26, we get,

$$B_{In} = \frac{(-1)^n \kappa - \frac{n}{2}}{\frac{n}{2} + 1} A_{In} \tag{3.27}$$

Now, using Eqn. 3.27, we can write the symmetric stress field solution as,

$$\sigma_{rr} = -\frac{n}{2} r^{\frac{n}{2}-1} A_{In} \left\{ \left(\frac{n}{2} - 3\right) \cos\left[\left(\frac{n}{2} - 1\right)\theta\right] + \left[(-1)^n \kappa - \frac{n}{2}\right] \cos\left[\left(\frac{n}{2} + 1\right)\theta\right] \right\}, \tag{3.28a}$$

$$\sigma_{\theta\theta} = \frac{n}{2} r^{\frac{n}{2}-1} A_{In} \left\{ \left(\frac{n}{2} + 1\right) \cos\left[\left(\frac{n}{2} - 1\right)\theta\right] + \left[(-1)^n \kappa - \frac{n}{2}\right] \cos\left[\left(\frac{n}{2} + 1\right)\theta\right] \right\}, \tag{3.28b}$$

$$\sigma_{r\theta} = \frac{n}{2} r^{\frac{n}{2}-1} A_{In} \left\{ \left(\frac{n}{2} - 1\right) \sin\left[\left(\frac{n}{2} - 1\right)\theta\right] + \left[(-1)^n \kappa - \frac{n}{2}\right] \sin\left[\left(\frac{n}{2} + 1\right)\theta\right] \right\} \tag{3.28c}$$

These stress field equations in polar coordinates transformed to cartesian coordinates using following equations,

$$\sigma_{xx} = \frac{\sigma_{rr} + \sigma_{\theta\theta}}{2} + \frac{\sigma_{rr} - \sigma_{\theta\theta}}{2} \cos 2\theta - \sigma_{r\theta} \sin 2\theta, \tag{3.29a}$$

$$\sigma_{yy} = \frac{\sigma_{rr} + \sigma_{\theta\theta}}{2} - \frac{\sigma_{rr} - \sigma_{\theta\theta}}{2} \cos 2\theta + \sigma_{r\theta} \sin 2\theta, \tag{3.29b}$$

$$\sigma_{xy} = \frac{\sigma_{rr} - \sigma_{\theta\theta}}{2} \sin 2\theta + \sigma_{r\theta} \cos 2\theta. \tag{3.29c}$$

The transformed stress field equations in cartesian coordinates using Eqn. 3.29 are given as,

$$\sigma_{xx} = \frac{n}{2} r^{\frac{n}{2}-1} A_{In} \left\{ \left[2 - (-1)^n \kappa + \frac{n}{2}\right] \cos\left[\left(\frac{n}{2} - 1\right)\theta\right] - \left(\frac{n}{2} - 1\right) \cos\left[\left(\frac{n}{2} - 3\right)\theta\right] \right\}, \tag{3.30a}$$

$$\sigma_{yy} = \frac{n}{2} r^{\frac{n}{2}-1} A_{In} \left\{ \left[2 + (-1)^n \kappa - \frac{n}{2}\right] \cos\left[\left(\frac{n}{2} - 1\right)\theta\right] + \left(\frac{n}{2} - 1\right) \cos\left[\left(\frac{n}{2} - 3\right)\theta\right] \right\}, \tag{3.30b}$$

$$\sigma_{xy} = \frac{n}{2} r^{\frac{n}{2}-1} A_{In} \left\{ \left[(-1)^n \kappa - \frac{n}{2}\right] \sin\left[\left(\frac{n}{2} - 1\right)\theta\right] + \left(\frac{n}{2} - 1\right) \sin\left[\left(\frac{n}{2} - 3\right)\theta\right] \right\}. \tag{3.30c}$$

Part - II: Anti-symmetric part

Now, lets consider the anti-symmetric part of Eqn. 3.16, as

$$\phi_{as} = C \sin[(\lambda - 1)\theta] + D \sin[(\lambda + 1)\theta] \tag{3.31}$$

Using Eqn. 3.15 and Eqn. 3.31, we get,

$$\sigma_{rr} = -\lambda r^{(\lambda-1)} \left\{ C(\lambda - 3) \sin[(\lambda - 1)\theta] + D(\lambda + 1) \sin[(\lambda + 1)\theta] \right\}, \tag{3.32a}$$

$$\sigma_{\theta\theta} = \lambda(\lambda + 1) r^{(\lambda-1)} \left\{ C \sin[(\lambda - 1)\theta] + D \sin[(\lambda + 1)\theta] \right\}, \tag{3.32b}$$

$$\sigma_{r\theta} = -\lambda r^{(\lambda-1)} \left\{ C(\lambda - 1) \cos[(\lambda - 1)\theta] + D(\lambda + 1) \cos[(\lambda + 1)\theta] \right\} \tag{3.32c}$$

To get displacement field solution corresponding to the specified anti-symmetric eigen function, ϕ_{as}, we use Michell's solutions, as,

$$2\mu u_r = r^\lambda \Big\{ C(\kappa - \lambda)\sin[(\lambda - 1)\theta] - D(\lambda + 1)\sin[(\lambda + 1)\theta] \Big\}, \tag{3.33}$$

$$2\mu u_\theta = -r^\lambda \Big\{ C(\kappa + \lambda)\cos[(\lambda - 1)\theta] + D(\lambda + 1)\cos[(\lambda + 1)\theta] \Big\} \tag{3.34}$$

Applying the boundary conditions as denoted in Eqn. 3.20, we get,

$$C(\kappa - \lambda)\sin[(\lambda - 1)\pi] - D(\lambda + 1)\sin[(\lambda + 1)\pi] = 0,$$
$$-C(\kappa + \lambda)\cos[(\lambda - 1)\pi] - D(\lambda + 1)\cos[(\lambda + 1)\pi] = 0.$$

On using sin and cos identities and simplifying, above equation becomes,

$$[-C(\kappa - \lambda) + D(\lambda + 1)]\sin(\pi\lambda) = 0, \tag{3.35}$$

$$[C(\kappa + \lambda) + D(\lambda + 1)]\cos(\pi\lambda) = 0. \tag{3.36}$$

From Eqn. 3.35, we get values of λ as,

$$\sin(\pi\lambda) = 0 \quad \Rightarrow \quad \lambda = 0, \pm 1, \pm 2, \pm 3, \pm 4..., \text{and so on.}$$

Now from Eqn. 3.36, we get relation in constants as,

$$D = -\frac{\kappa + \lambda}{\lambda + 1}C \tag{3.37}$$

Now, from Eqn. 3.36, we get values of λ as,

$$\cos(\pi\lambda) = 0 \quad \Rightarrow \quad \lambda = \pm\frac{1}{2}, \pm\frac{3}{2}, \pm\frac{5}{2}, \pm\frac{7}{2}..., \text{and so on.}$$

Now from Eqn. 3.35, we get relation in constants as,

$$D = \frac{\kappa - \lambda}{\lambda + 1}C \tag{3.38}$$

Consider $\lambda = \frac{n}{2}$, where, n is positive integer, and combining the two relations from Eqn. 3.37 and Eqn. 3.38, we get,

$$D_{IIn} = \frac{(-1)^n \kappa - \frac{n}{2}}{\frac{n}{2} + 1} A_{IIn} \tag{3.39}$$

Now, using Eqn. 3.39, we can write the anti-symmetric stress field solution as,

$$\sigma_{rr} = -\frac{n}{2}r^{\frac{n}{2}-1}A_{IIn}\Big\{ \Big(\frac{n}{2} - 3\Big)\sin\Big[\Big(\frac{n}{2} - 1\Big)\theta\Big] - \Big[(-1)^n \kappa + \frac{n}{2}\Big]\sin\Big[\Big(\frac{n}{2} + 1\Big)\theta\Big] \Big\}, \tag{3.40a}$$

$$\sigma_{\theta\theta} = \frac{n}{2}r^{\frac{n}{2}-1}A_{IIn}\Big\{ \Big(\frac{n}{2} + 1\Big)\sin\Big[\Big(\frac{n}{2} - 1\Big)\theta\Big] - \Big[(-1)^n \kappa + \frac{n}{2}\Big]\sin\Big[\Big(\frac{n}{2} + 1\Big)\theta\Big] \Big\}, \tag{3.40b}$$

$$\sigma_{r\theta} = -\frac{n}{2}r^{\frac{n}{2}-1}A_{IIn}\Big\{ \Big(\frac{n}{2} - 1\Big)\cos\Big[\Big(\frac{n}{2} - 1\Big)\theta\Big] - \Big[(-1)^n \kappa + \frac{n}{2}\Big]\cos\Big[\Big(\frac{n}{2} + 1\Big)\theta\Big] \Big\} \tag{3.40c}$$

These stress field equation in polar co-ordinates transformed to cartesian co-ordinates using Eqn.

3.29, as,

$$\sigma_{xx} = \frac{n}{2}r^{\frac{n}{2}-1}A_{IIn}\left\{\left[2 + (-1)^n\kappa + \frac{n}{2}\right]\sin\left[\left(\frac{n}{2}-1\right)\theta\right] - \left(\frac{n}{2}-1\right)\sin\left[\left(\frac{n}{2}-3\right)\theta\right]\right\}, \qquad (3.41a)$$

$$\sigma_{yy} = \frac{n}{2}r^{\frac{n}{2}-1}A_{IIn}\left\{\left[2 - (-1)^n\kappa - \frac{n}{2}\right]\sin\left[\left(\frac{n}{2}-1\right)\theta\right] + \left(\frac{n}{2}-1\right)\sin\left[\left(\frac{n}{2}-3\right)\theta\right]\right\}, \qquad (3.41b)$$

$$\sigma_{xy} = \frac{n}{2}r^{\frac{n}{2}-1}A_{IIn}\left\{\left[(-1)^n\kappa + \frac{n}{2}\right]\cos\left[\left(\frac{n}{2}-1\right)\theta\right] - \left(\frac{n}{2}-1\right)\cos\left[\left(\frac{n}{2}-3\right)\theta\right]\right\}. \qquad (3.41c)$$

Now the complete multi-parameter stress field solution in the polar coordinates can be obtained by adding Eqn. 3.28 and Eqn. 3.40, as,

$$\sigma_{rr} = -\frac{n}{2}r^{\frac{n}{2}-1}A_{In}\left\{\left(\frac{n}{2}-3\right)\cos\left[\left(\frac{n}{2}-1\right)\theta\right] + \left[(-1)^n\kappa - \frac{n}{2}\right]\cos\left[\left(\frac{n}{2}+1\right)\theta\right]\right\}$$
$$-\frac{n}{2}r^{\frac{n}{2}-1}A_{IIn}\left\{\left(\frac{n}{2}-3\right)\sin\left[\left(\frac{n}{2}-1\right)\theta\right] - \left[(-1)^n\kappa + \frac{n}{2}\right]\sin\left[\left(\frac{n}{2}+1\right)\theta\right]\right\}, \qquad (3.42a)$$

$$\sigma_{\theta\theta} = \frac{n}{2}r^{\frac{n}{2}-1}A_{In}\left\{\left(\frac{n}{2}+1\right)\cos\left[\left(\frac{n}{2}-1\right)\theta\right] + \left[(-1)^n\kappa - \frac{n}{2}\right]\cos\left[\left(\frac{n}{2}+1\right)\theta\right]\right\}+$$
$$\frac{n}{2}r^{\frac{n}{2}-1}A_{IIn}\left\{\left(\frac{n}{2}+1\right)\sin\left[\left(\frac{n}{2}-1\right)\theta\right] - \left[(-1)^n\kappa + \frac{n}{2}\right]\sin\left[\left(\frac{n}{2}+1\right)\theta\right]\right\}, \qquad (3.42b)$$

$$\sigma_{r\theta} = \frac{n}{2}r^{\frac{n}{2}-1}A_{In}\left\{\left(\frac{n}{2}-1\right)\sin\left[\left(\frac{n}{2}-1\right)\theta\right] + \left[(-1)^n\kappa - \frac{n}{2}\right]\sin\left[\left(\frac{n}{2}+1\right)\theta\right]\right\}-$$
$$\frac{n}{2}r^{\frac{n}{2}-1}A_{IIn}\left\{\left(\frac{n}{2}-1\right)\cos\left[\left(\frac{n}{2}-1\right)\theta\right] - \left[(-1)^n\kappa + \frac{n}{2}\right]\cos\left[\left(\frac{n}{2}+1\right)\theta\right]\right\} \qquad (3.42c)$$

Similarly, we can get the transformed stress field equations in cartesian coordinates by adding the Eqn. 3.30 and Eqn. 3.41, as

$$\sigma_{xx} = \frac{n}{2}r^{\frac{n}{2}-1}A_{In}\left\{\left[2 - (-1)^n\kappa + \frac{n}{2}\right]\cos\left[\left(\frac{n}{2}-1\right)\theta\right] - \left(\frac{n}{2}-1\right)\cos\left[\left(\frac{n}{2}-3\right)\theta\right]\right\}+$$
$$\frac{n}{2}r^{\frac{n}{2}-1}A_{IIn}\left\{\left[2 + (-1)^n\kappa + \frac{n}{2}\right]\sin\left[\left(\frac{n}{2}-1\right)\theta\right] - \left(\frac{n}{2}-1\right)\sin\left[\left(\frac{n}{2}-3\right)\theta\right]\right\}, \qquad (3.43a)$$

$$\sigma_{yy} = \frac{n}{2}r^{\frac{n}{2}-1}A_{In}\left\{\left[2 + (-1)^n\kappa - \frac{n}{2}\right]\cos\left[\left(\frac{n}{2}-1\right)\theta\right] + \left(\frac{n}{2}-1\right)\cos\left[\left(\frac{n}{2}-3\right)\theta\right]\right\}+$$
$$\frac{n}{2}r^{\frac{n}{2}-1}A_{IIn}\left\{\left[2 - (-1)^n\kappa - \frac{n}{2}\right]\sin\left[\left(\frac{n}{2}-1\right)\theta\right] + \left(\frac{n}{2}-1\right)\sin\left[\left(\frac{n}{2}-3\right)\theta\right]\right\}, \qquad (3.43b)$$

$$\sigma_{xy} = \frac{n}{2}r^{\frac{n}{2}-1}A_{In}\left\{\left[(-1)^n\kappa - \frac{n}{2}\right]\sin\left[\left(\frac{n}{2}-1\right)\theta\right] + \left(\frac{n}{2}-1\right)\sin\left[\left(\frac{n}{2}-3\right)\theta\right]\right\}+$$
$$\frac{n}{2}r^{\frac{n}{2}-1}A_{IIn}\left\{\left[(-1)^n\kappa + \frac{n}{2}\right]\cos\left[\left(\frac{n}{2}-1\right)\theta\right] - \left(\frac{n}{2}-1\right)\cos\left[\left(\frac{n}{2}-3\right)\theta\right]\right\}. \qquad (3.43c)$$

The strain in x direction, ϵ_{xx}, for plain strain condition in the stress term is given as,

$$\epsilon_{xx} = \frac{1+\nu}{E}\left[(1-\nu)\sigma_{xx} - \nu\sigma_{yy}\right]. \qquad (3.44)$$

We also know the definition of strain intensity factor is given as,

$$K_I^\epsilon = \lim_{r\to 0}\epsilon_{xx}(\theta = 0°)\sqrt{r}. \qquad (3.45)$$

Now, from the Eqn. 3.44 and Eqn. 3.45, we get,

$$K_I^\epsilon = A_{I1}\left[\frac{\kappa(1+\nu)}{E}\right]. \qquad (3.46)$$

Eqn. 3.46 shows the relation between the strain intensity factor, K_I^ϵ, and the coefficient constants

in the stress equation for $n = 1$, viz. A_{I1}. Hence to find strain intensity factor, we need to find A_{I1}. Because we have the stress field for the inclusion problem from the photoelasticity, hence we can get the A_{I1} and so the strain intensity factor. Similarly, we can get K_{II}^{ϵ} using

$$K_{II}^{\epsilon} = A_{II1} \left[\frac{(\kappa - 1)(1 + \nu)}{E} \right]. \tag{3.47}$$

3.3 Specimen preparation

The specimen made up of epoxy-resin is prepared using simple casting process for the photoelasticity experiment. The vertical perpendicular distance between the line inclusion and the hole centre is $s = 20mm$. The diameter of the hole and the length of the line inclusion is $D = 10mm$ and $2L = 20mm$ respectively. The Dimensions of the specimen are $200mm \times 110mm \times 6mm$ as shown in Fig. 3.2. The specimen is made up of resin Epofine-221 and hardener Finehard-1842, supplied by Fine Finish Organics Pvt. Ltd., India., with the proportion $100 : 40$ by weight.
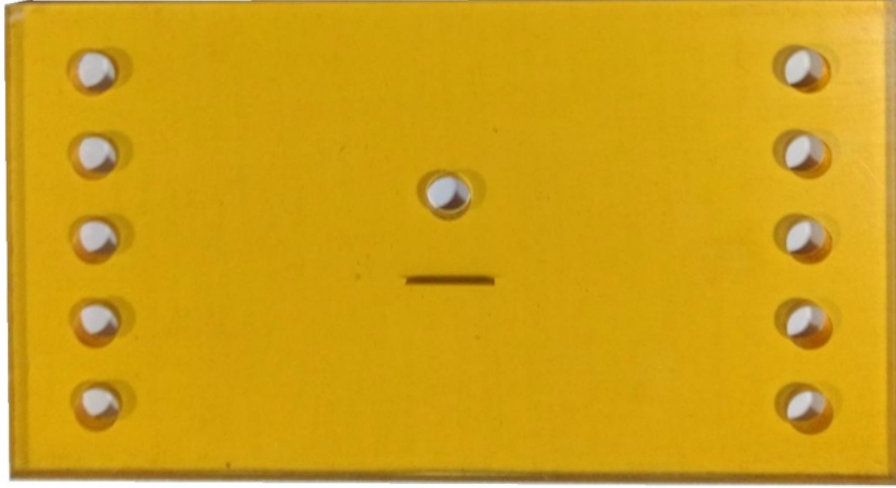
Figure 3.2: A line inclusion with a hole embedded in resin-matrix specimen prepared for photoelasticity experimentation.

3.3.1 Fabrication procedure

The process is a casting process. The mould is prepared as per the size required and cleansed with isopropylene properly to avoid any dust contamination of the specimen. An inclusion of height less than $6mm$ (approximately $5.7mm - 5.8mm$), length $20mm$ and thickness $0.1mm$, made up of steel is prepared, and the surfaces made smoother using fine (P 400) sandpaper to create good contact with a resin material. With proper precautions and marking, this inclusion has adhered upon one of the mould plate using an adhering agent like Fevicol.

The specimen is prepared for larger dimensions than required for the experiment to accommodate the machining allowances. The average density of resin-hardener mixture is $1.13 \ kg/mm^3$. Then in clean and cleansed (with acetone) separate beakers, resin and hardener are taken in required mass proportion. The beakers are heated in hot water to remove the air entrapped in resin and hardener.

After cooled down the beakers, the hardener is poured in resin, and then the mixture is stirred it looks like a homogeneous and wavy-smoke-free. Then the mixture is poured slowly into the mould. Mould is kept in the furnace at a constant temperature of 60°C for 48 hours. Afterwards, the specimen is removed from the furnace and machined using CNC machine, for specified dimensions, and a hole is drilled of 10mm diameter. Also, to fix the specimen in the fixtures of the testing machine, five holes of 10mm are drilled on either side (perpendicular to the inclusion length).
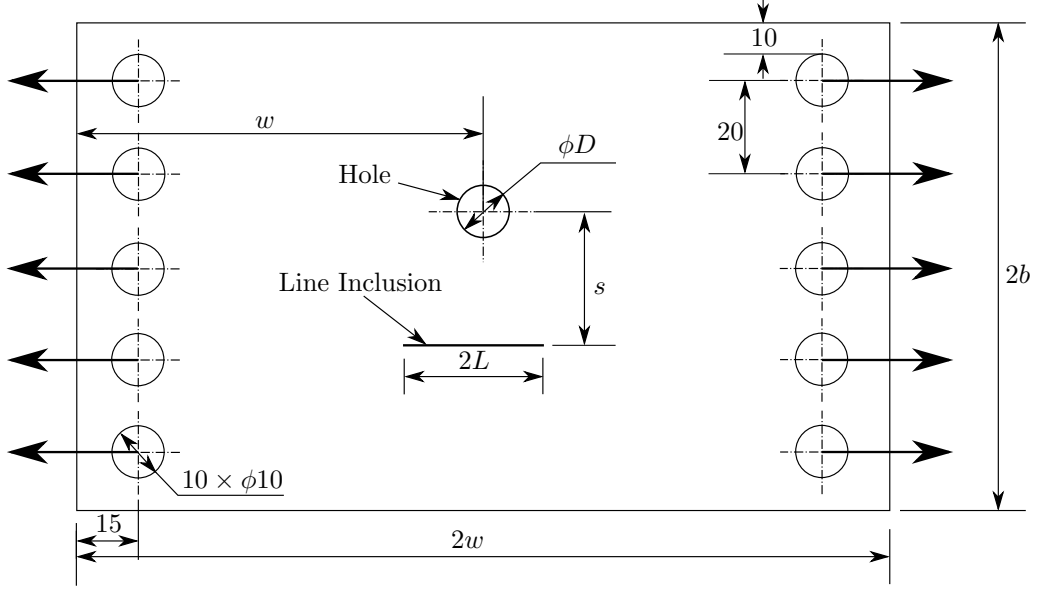
Figure 3.3: A line inclusion with a hole embedded in resin-matrix specimen drawing with dimensions used for the photoelasticity experimentation.

At last, the specimen must be checked for the residual stresses using the polariscope. Specimen must be residual stress-free to obtain good and reliable results out of it. Fig. 3.3 shows a specimen configuration for the photoelasticity experiment to find out strain intensity factor value.

3.4 Photoelastic Experimentation

3.4.1 Ten-step method

Ten-step phase shifting techniques is useful in getting the whole field isoclinic and isochromatic data [33]. Recently, Ramji and Prasath [34] have done an error study to find out the effectiveness of the ten-step method and they found it to be very robust against various error source. For the ten-step PST, the optical arrangements for different optical elements used are given in Table 3.1. In the above Table 2.1, I_b is surrounding light intensity, I_a is light intensity of light source, δ is phase retardation through the specimen and θ is principal stress orientation.

The first four optical arrangements are called as plane polariscope because the incident light on the specimen is plane polarised, where the quarter wave plates are absent or optically effect made null by putting them align with the other optical elements, viz. polariser and analyser. In these arrangements, we can see both fringe contours, viz. isoclinics and isochromatics. The remaining six

Table 3.1: Ten-step method: Polariscope arrangements and intensity equations for isoclinic and isochromatics evaluation

No.	α	ζ	η	β	Intensity Equation
1.	$\pi/2$	-	-	0	$I_1 = I_b + I_a \sin^2(\frac{\delta}{2}) \sin^2 2\theta$
2.	$5\pi/8$	-	-	$\pi/8$	$I_2 = I_b + \frac{I_a}{2} \sin^2(\frac{\delta}{2})(1 - \sin 4\theta)$
3.	$3\pi/4$	-	-	$\pi/4$	$I_3 = I_b + I_a \sin^2(\frac{\delta}{2}) \cos^2 2\theta$
4.	$7\pi/8$	-	-	$3\pi/8$	$I_4 = I_b + \frac{I_a}{2} \sin^2(\frac{\delta}{2})(1 + \sin 4\theta)$
5.	$\pi/2$	$3\pi/4$	$\pi/4$	$\pi/2$	$I_5 = I_b + \frac{I_a}{2}(1 + \cos \delta)$
6.	$\pi/2$	$3\pi/4$	$\pi/4$	0	$I_6 = I_b + \frac{I_a}{2}(1 - \cos \delta)$
7.	$\pi/2$	$3\pi/4$	0	0	$I_7 = I_b + \frac{I_a}{2}(1 - \sin 2\theta \sin \delta)$
8.	$\pi/2$	$3\pi/4$	$\pi/4$	$\pi/4$	$I_8 = I_b + \frac{I_a}{2}(1 + \cos 2\theta \sin \delta)$
9.	$\pi/2$	$\pi/4$	0	0	$I_9 = I_b + \frac{I_a}{2}(1 + \sin 2\theta \sin \delta)$
10.	$\pi/2$	$\pi/4$	$3\pi/4$	$\pi/4$	$I_{10} = I_b + \frac{I_a}{2}(1 - \cos 2\theta \sin \delta)$

optical arrangements are called circular polariscope because the incident light on the specimen is circularly polarised, where quarter wave plates are arranged such a way that the light coming out of first quarter wave will be circularly polarized light and that of after second quarter wave plate light will be again plane polarized. In these arrangements, we can see only isochromatics fringe contours. Using above different arrangements, the wrapped isoclinic and isochromatic values can be obtained as

$$\theta_c = \frac{1}{4} \tan^{-1} \left(\frac{I_4 - I_2}{I_3 - I_1} \right) \quad \text{and} \tag{3.48}$$

$$\delta_c = \tan^{-1} \left(\frac{(I_9 - I_7) \sin 2\theta + (I_8 - I_{10}) \cos 2\theta}{I_5 - I_6} \right). \tag{3.49}$$

From equation 3.48, one can get the wrapped isoclinic phase map in the range $-\pi/4$ to $+\pi/4$ with inconsistent zone and it needs to be unwrapped. Later, the unwrapped isoclinic data is used for the isochromatic phase map generation as given in equation 3.49. Finally, the wrapped isochromatic phase map has to be unwrapped for getting the continuous fringe order.

3.4.2 Experimentation

Fig. 3.4 shows the experimental setup for the transmission photoelasticity used in this study. The ten-step images are captures using the BASLER monochrome CCD (charged coupled device) camera for the optical arrangement shown in Table 3.1. The CCD camera has a spatial resolution of 1392 × 1040 pixels. The specimen is loaded using a 10kN INSTRON 5600 Machine with the proper fixtures.

For the material used for the specimen, fabrication has the materials fringe value of 0.27 N/m-

m/fringe. The isoclinic and isochromatic data surrounding to inclusion-tip is required for estimation of the strain intensity factor. The unwrapped isoclinics without inconsistent zones is obtained using ten-step PST by the AQGUP algorithm. Then using unwrapped isoclinics data, unwrapped isochromatic data is obtained without any ambiguity zones.
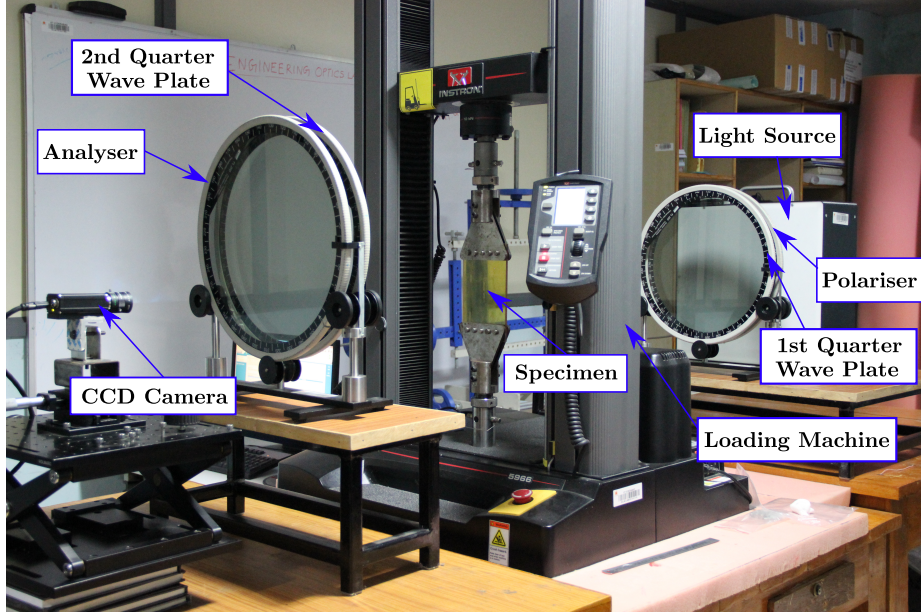
Figure 3.4: Transmission digital photoelasticity experimental setup for strain intensity factor estimation

3.5 Experimental evaluation of Strain intensity factor

In this section, experimental estimation of strain intensity factor for a rigid line inclusion problem using digital photoelasticity is discussed. The strain intensity factor are evaluated by finding the coefficients of the multi-parameter stress field equation as shown in Eqns. 3.57. These coefficients are estimated by fitting the curve of the multi-parameter stress field equation over the experimental isochromatic data around the inclusion-tip. For this curve fitting a linear least square approach a adopted as discussed in this section further. For this, we need unwrapped isoclinic and isochromatic data obtained by AQGUP algorithm using the ten-step method. Using the software interface developed in the MATLAB, the photoelastic parameters are collected automatically. The extracted data corresponds to fringe order (N), principal stress difference (θ_{uw}) (unwrapped data), the corresponding location of points and inclusion-tip location given by the user via GUI. The data collection area is annular, and its minimum radius is chosen in such a way that to avoid the plastic region ahead of the inclusion-tip and three-dimensional stress effect nearer to inclusion-tip. Fig. 3.6a shows a data collection annular area.

From the stress optics law, the principal stress difference and fringe order are related as,

$$\sigma_1 - \sigma_2 = \frac{NF_\sigma}{h}, \tag{3.50}$$
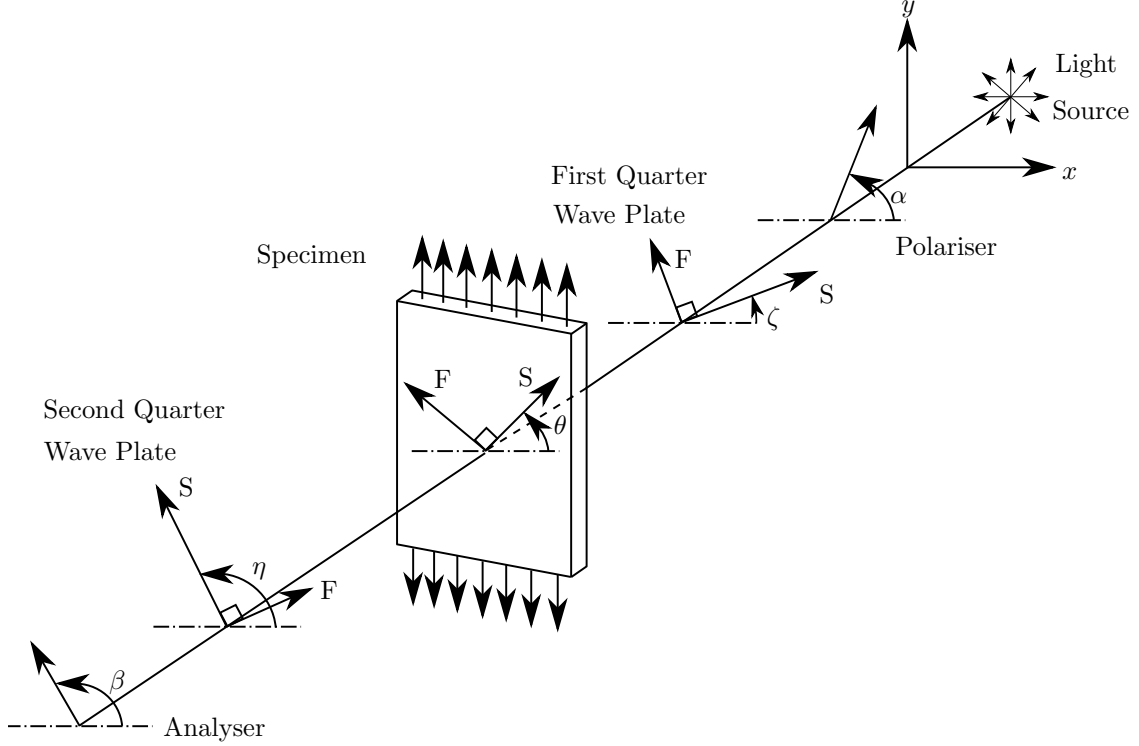
Figure 3.5: Generic optical element arrangement for transmission photoelasticity experimentation.

where, σ_1 and σ_2 are the principal stresses in 1 and 2 direction respectively, N is the fringe order, F_σ is the material fringe value and h is the specimen thickness. As we know the whole field isochromatic or fringe order data, hence we can find the principal stress difference from the Eqn. 3.50. Also the normal stress difference and shear stress are defined in terms of principal stress difference and principal stress direction orientation using Mohr's circle as given below,

$$\begin{Bmatrix} \sigma_x - \sigma_y \\ \tau_{xy} \end{Bmatrix} = \begin{Bmatrix} (\sigma_1 - \sigma_2) \cos 2\theta_{uw} \\ \frac{(\sigma_1 - \sigma_2)}{2} \sin 2\theta_{uw} \end{Bmatrix}, \tag{3.51}$$

where, σ_x and σ_y are the principal stresses in x and y direction respectively and θ_{uw} is the unwrapped principal stress direction orientation. Now we know the principal stress difference, $(\sigma_1 - \sigma_2)$, hence we can find the normal stress difference and shear stress from the Eqn. 3.51. Further, from this stresses information, we can find strain intensity factor using Eqn. 3.43.

3.5.1 Multi-parameter stress field equations

The multi-parameter stress field equations for mixed mode rigid line inclusion are given by the Eqn. 3.42. These stress field equation can be written in general form as,

$$\phi = -\sum_{n=1}^{\infty} \frac{n}{2} A_{In} r^{\frac{n}{2}-1} \boldsymbol{S} - \sum_{n=1}^{\infty} \frac{n}{2} A_{IIn} r^{\frac{n}{2}-1} \boldsymbol{P}, \tag{3.52}$$

32

where,

$$\phi = \begin{Bmatrix} \sigma_x \\ \sigma_y \\ \tau_{xy} \end{Bmatrix}, \tag{3.53}$$

$$\boldsymbol{S} = \begin{Bmatrix} \left[2 - (-1)^n \kappa + \frac{n}{2} \right] \cos\left[\left(\frac{n}{2} - 1 \right)\theta \right] - \left(\frac{n}{2} - 1 \right) \cos\left[\left(\frac{n}{2} - 3 \right)\theta \right] \\ \left[2 + (-1)^n \kappa - \frac{n}{2} \right] \cos\left[\left(\frac{n}{2} - 1 \right)\theta \right] + \left(\frac{n}{2} - 1 \right) \cos\left[\left(\frac{n}{2} - 3 \right)\theta \right] \\ \left[(-1)^n \kappa - \frac{n}{2} \right] \sin\left[\left(\frac{n}{2} - 1 \right)\theta \right] + \left(\frac{n}{2} - 1 \right) \sin\left[\left(\frac{n}{2} - 3 \right)\theta \right] \end{Bmatrix}, \tag{3.54}$$

$$\boldsymbol{P} = \begin{Bmatrix} \left[2 + (-1)^n \kappa + \frac{n}{2} \right] \sin\left[\left(\frac{n}{2} - 1 \right)\theta \right] - \left(\frac{n}{2} - 1 \right) \sin\left[\left(\frac{n}{2} - 3 \right)\theta \right] \\ \left[2 - (-1)^n \kappa - \frac{n}{2} \right] \sin\left[\left(\frac{n}{2} - 1 \right)\theta \right] + \left(\frac{n}{2} - 1 \right) \sin\left[\left(\frac{n}{2} - 3 \right)\theta \right] \\ \left[(-1)^n \kappa + \frac{n}{2} \right] \cos\left[\left(\frac{n}{2} - 1 \right)\theta \right] - \left(\frac{n}{2} - 1 \right) \cos\left[\left(\frac{n}{2} - 3 \right)\theta \right] \end{Bmatrix}, \tag{3.55}$$

where, σ_x and σ_y are the normal stress component along x and y directions respectively, τ_{xy} is in plane shear stress, r and θ are the polar coordinates with origin at the inclusion-tip and n is the number of parameters. The coefficients A_{In} and A_{IIn} define inclusion-tip stress field and they are related to strain intensity factor by Eqn.3.46 and Eqn. 3.47 respectively.

3.5.2 Formulation for linear least square approach

Rewriting the Eqn. 3.52 in general form as we need for further analysis as follows,

$$\sigma_x - \sigma_y = \sum_{n=1}^{\infty} A_{In} \ f_{In}(r,\theta) - \sum_{n=1}^{\infty} A_{IIn} \ f_{IIn}(r,\theta), \tag{3.56}$$

$$\tau_{xy} = \sum_{n=1}^{\infty} A_{In} \ g_{In}(r,\theta) - \sum_{n=1}^{\infty} A_{IIn} \ g_{IIn}(r,\theta), \tag{3.57}$$

where,

$$f_{In} = n r^{\frac{n}{2}-1} \left\{ \left[-(-1)^n \kappa + \frac{n}{2} \right] \cos\left[\left(\frac{n}{2} - 1 \right)\theta \right] - \left(\frac{n}{2} - 1 \right) \cos\left[\left(\frac{n}{2} - 3 \right)\theta \right] \right\}, \tag{3.58}$$

$$f_{IIn} = n r^{\frac{n}{2}-1} \left\{ \left[(-1)^n \kappa + \frac{n}{2} \right] \sin\left[\left(\frac{n}{2} - 1 \right)\theta \right] - \left(\frac{n}{2} - 1 \right) \sin\left[\left(\frac{n}{2} - 3 \right)\theta \right] \right\}, \tag{3.59}$$

$$g_{In} = \frac{n}{2} r^{\frac{n}{2}-1} \left\{ \left[(-1)^n \kappa - \frac{n}{2} \right] \sin\left[\left(\frac{n}{2} - 1 \right)\theta \right] + \left(\frac{n}{2} - 1 \right) \sin\left[\left(\frac{n}{2} - 3 \right)\theta \right] \right\}, \tag{3.60}$$

$$g_{IIn} = \frac{n}{2} r^{\frac{n}{2}-1} \left\{ \left[(-1)^n \kappa + \frac{n}{2} \right] \cos\left[\left(\frac{n}{2} - 1 \right)\theta \right] - \left(\frac{n}{2} - 1 \right) \cos\left[\left(\frac{n}{2} - 3 \right)\theta \right] \right\}, \tag{3.61}$$

where, f_{In}, f_{IIn}, g_{In} and g_{IIn} are the function of number of parameters, n, and polar co-ordinates r and θ. We already know that the inclusion-tip location can have great influence on the strain intensity factor determined, hence inputting the correct inclusion-tip location is considered as an important task in estimating the strain intensity factor value. But in many cases, it is difficult to select the inclusion-tip manually from the photoelasticity images as its the spatial resolution is very low. Hence, there will be always uncertainty in inputting the inclusion-tip location and so will be

in the strain intensity factor value. Therefore to tackle this problem, we consider the inclusion-tip location itself an unknown variable to be determined along with the coefficients A_{In} and A_{IIn} as in Eqn. 3.56 and Eqn. 3.57.

Now, consider a point (x, y) in the Cartesian coordinate system with the origin at an arbitrary location. Then the inclusion-tip location is related to r and θ as follows,

$$r = \sqrt{(x - x_c)^2 + (y - y_c)^2}, \tag{3.62}$$

$$\theta = \tan^{-1}\left(\frac{y - y_c}{x - x_c}\right), \tag{3.63}$$

where, x_c and y_c are the inclusion-tip location relative to the arbitrary Cartesian coordinate system. The Eqn. 3.62 and Eqn. 3.63 enable us to translate the co-ordinate system with respect to the inclusion-tip location. Due to the computational limitations, the number of parameters , n, in the multi-parameter stress field equations given by the Eqn. 3.56 and Eqn. 3.57 are limited. For a single point P, the truncated n parameter equations Eqn. 3.56 and Eqn. 3.57 can be written in a matrix form as follows,

$$\underbrace{\left\{\begin{array}{c} \sigma_x - \sigma_y \\ \\ \tau_{xy} \end{array}\right\}}_{\boldsymbol{\sigma_p}} = \underbrace{\begin{bmatrix} f_{I1}(r_p, \theta_p) & g_{I1}(r_p, \theta_p) \\ f_{I2}(r_p, \theta_p) & g_{I2}(r_p, \theta_p) \\ \vdots & \vdots \\ f_{In}(r_p, \theta_p) & g_{In}(r_p, \theta_p) \\ -f_{II1}(r_p, \theta_p) & -g_{II1}(r_p, \theta_p) \\ -f_{II2}(r_p, \theta_p) & -g_{II2}(r_p, \theta_p) \\ \vdots & \vdots \\ -f_{IIn}(r_p, \theta_p) & -g_{IIn}(r_p, \theta_p) \end{bmatrix}^{\mathrm{T}}}_{\boldsymbol{Q_p}} \underbrace{\left\{\begin{array}{c} A_{I1} \\ A_{I2} \\ \vdots \\ A_{In} \\ A_{II1} \\ A_{II2} \\ \vdots \\ A_{IIn} \end{array}\right\}}_{\boldsymbol{a}}. \tag{3.64}$$

The above equation can be written in simple matrix form as follows,

$$\boldsymbol{\sigma_p} = \boldsymbol{Q_p^{\mathrm{T}}} \boldsymbol{a}. \tag{3.65}$$

Now, for m collected data points surrounding to the inclusion-tip, the solution can be written in matrix form as follows,

$$\boldsymbol{\sigma} = \boldsymbol{Q}(x_c, y_c)\boldsymbol{a}, \tag{3.66}$$

where, $\boldsymbol{\sigma} = [\boldsymbol{\sigma_1^T}, \boldsymbol{\sigma_2^T}, ...\boldsymbol{\sigma_m^T}]$ and $\boldsymbol{C} = [\boldsymbol{Q_1^T}, \boldsymbol{Q_2^T}, ...\boldsymbol{Q_m^T}]^T$. Here, σ is the vector consisting of the experimental values of $\sigma_x - \sigma_y$ and τ_{xy} estimated using the Eqns. 3.51. The matrix $\boldsymbol{C}$ is dependent on x_c and y_c which is a rectangular matrix of the order $2m \times 2n$ and $\boldsymbol{a}$ is the vector consisting of unknown mode I and mode II parameters. Now, the values of x_c, y_c and $\boldsymbol{a}$ can be estimated using the minimizing the objective function given as,

$$J(x_c, y_c, \boldsymbol{a}) = \frac{1}{2}\left[\boldsymbol{\sigma} - \boldsymbol{C}(x_c, y_c)\boldsymbol{a}\right]^T\left[\boldsymbol{\sigma} - \boldsymbol{C}(x_c, y_c)\boldsymbol{a}\right]. \tag{3.67}$$
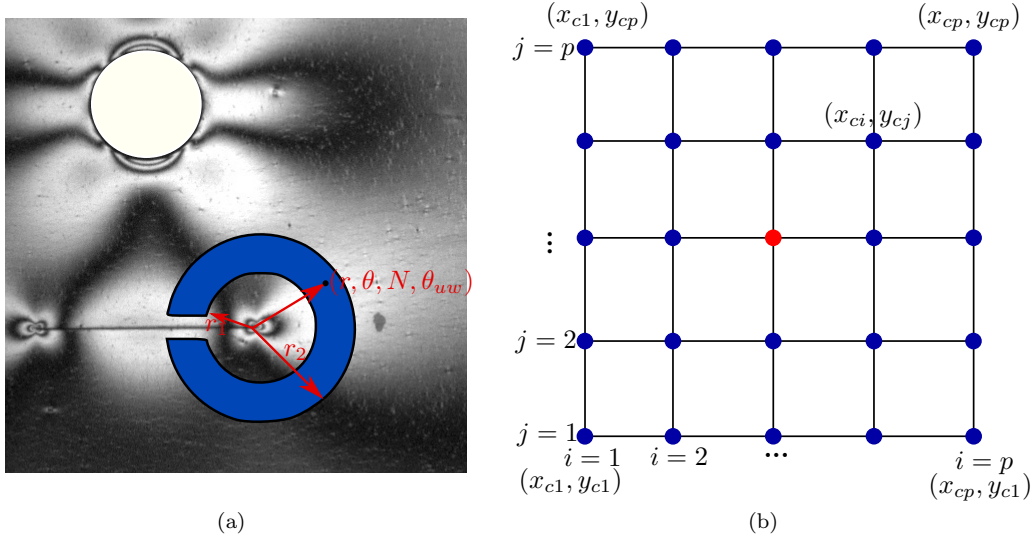
Figure 3.6: Data collection zone and corresponding grid pattern representation. a) schematic representation of annular region for data collection for estimation of strain intensity factor in case rigid line inclusion and a hole problem, b) Schematic representation of square grid pattern used for finding the exact inclusion-tip location.

The objective function J is non-quadratic for stress in terms of unknown parameters, and it also depends on the unknown inclusion-tip co-ordinates x_c and y_c. But when inclusion-tip co-ordinates x_c and y_c are known, the objective function J becomes quadratic, and a closed form of a solution does exist for it. Here, to estimate J both normal stress component difference, $\sigma_x - \sigma_y$, and shear stress, τ_{xy}, are considered. If we considered only a normal stress component difference or shear stress, then we get strain intensity factor value closer to that of actual value, but the reconstructed fringe contours do not match with the experimental fringe contours. This can also create difficulties in selection number parameters for multi-parameter stress field equation. The closed form solution for the unknown vector of parameters ($\boldsymbol{a}$), where the objective function has a global minimum is as follows,

$$\boldsymbol{a} = (\boldsymbol{C}^T \boldsymbol{C})^{-1} \boldsymbol{C}^T \boldsymbol{\sigma}, \tag{3.68}$$

where $(\boldsymbol{C}^T \boldsymbol{C})^{-1} \boldsymbol{C}^T$ is the pseudo inverse of $\boldsymbol{C}$. Now, to find the minimum values of J_{ij}, we select the multiple points, x_{ci}, y_{cj}, where $i = 1, 2, ...p$ and $j = 1, 2, ..., p$ as shown in Fig. 3.6b, collected around inclusion-tip region as shown in Fig. 3.6a. Now for every points, we can estimate the unknown parameters $\boldsymbol{a}_{ij}$ using Eqn. 3.68. Now, having known the values of $\boldsymbol{a}_{ij}$ for every points, we estimate the objective function J_{ij} values using the Eqn. 3.67. Out of all selected and data collected grid points as shown in Fig. 3.6b, for the point produces a minimum value of J_{ij} considered as inclusion-tip location. Hence we can say, $(x_c^*, y_c^*) = (x_{ci}, y_{cj})$ and unknown parameters $\boldsymbol{a}^* = \boldsymbol{a}_{ij}$. Mathematically, this idea of finding optimal value of strain intensity factor and inclusion-tip location can represented as follows,

$$[\boldsymbol{a}^{*T} \quad x_c^{*T} \quad y_c^{*T}] = \arg \min[\min(J_{ij})], \tag{3.69}$$

where, $i = 1, 2, ...p$ and $j = 1, 2, ..., p$, x_c and y_c are the inclusion-tip co-ordinates, $x_c p$ and $x_c p$ are the maximum and minimum x co-ordinate values of the square grid, $y_c p$ and $y_c p$ are the maximum and minimum y co-ordinate values of the square grid, r_1 and $r2$ are the inner and outer radius of data collection zone as shown in Fig. 3.6, n is number of unknown parameters (see the Eqn. 3.64). The algorithm of find the fracture parameters is summarised in the flowchart form as shown in Fig. 3.7
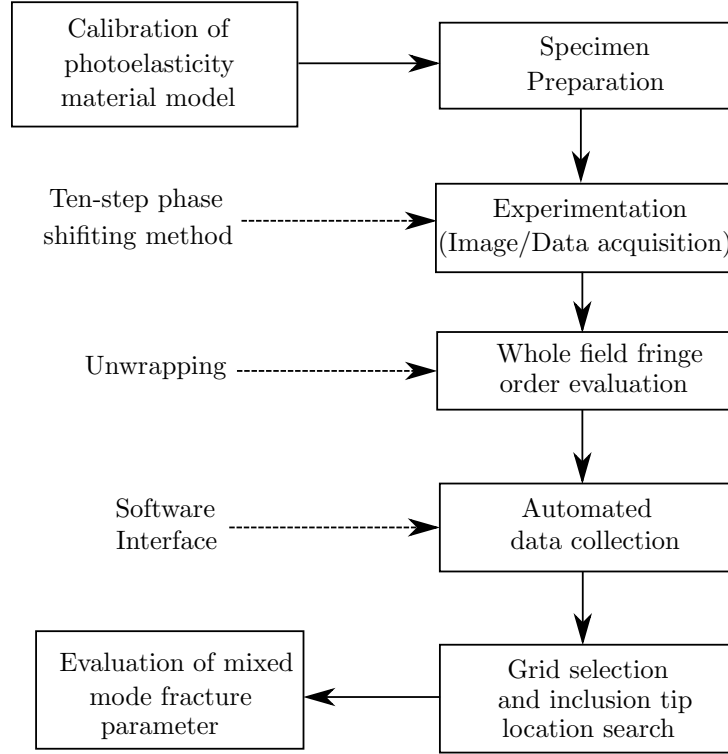
Figure 3.7: Flowchart showing various steps involving in the estimation of optimal fracture parameters using digital photoelasticity

3.6   Result and discussion

Unwrapping of isochromatic and isoclinic phasemaps is obtained using the AQGUP algorithm using the ten-step method. Further, the fringe order and isoclinic data are collected near the inclusion-tip in an annular region using semi-GUI based software developed in MATLAB for digital photoelasticity applications. This collected data is given input to multi-parameter stress field equations for estimation of optimal fracture parameters, here, strain intensity factor.

3.6.1   Experimental estimation of strain intensity factor for inclusion with a hole specimen

Strain intensity factor is estimated for the rigid line inclusion with a hole problem using digital photoelasticity. For the estimation of strain intensity factor, the whole field isoclinic and fringe
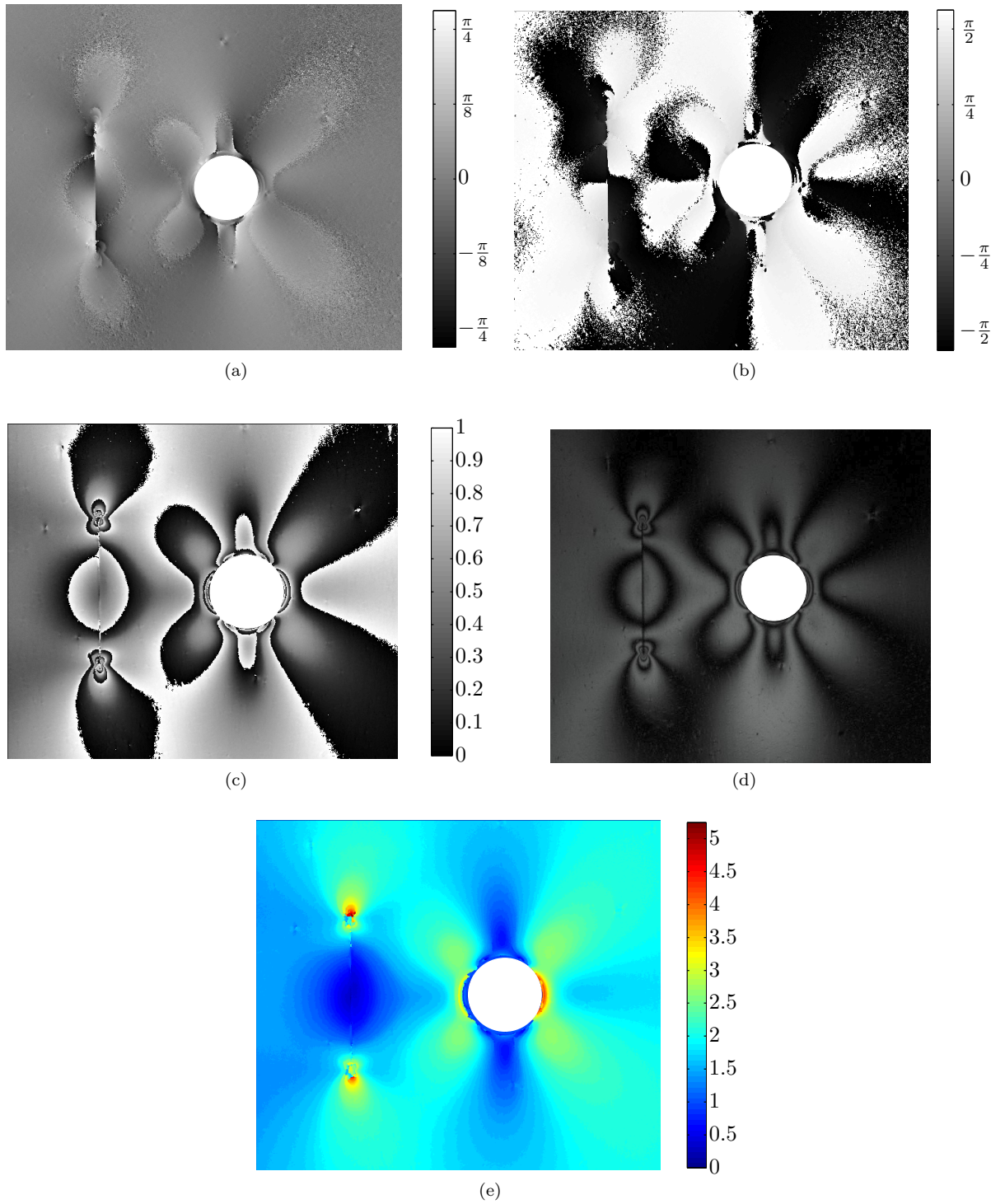
Figure 3.8: Isoclinic and isochromatic phasemaps for rigid line inclusion with a hole problem (a) wrapped isoclinic phasemap, (b) unwrapped isoclinic phasemap, (c) wrapped isochromatic phasemap (d) dark field photoelastic image and (e) unwrapped isochromatic phasemap

37

order data is needed. For this, ten-step PST is used where ten images are captured with the different optical arrangement as described in Table. 3.1. Firstly, wrapped isoclinic data is generated, and it is then unwrapped to get isoclinic data without inconsistent zones using AQGUP algorithm. This unwrapped isoclinic data is then used to get wrapped isochromatic data and further it is unwrapped to isochromatic data without ambiguous zones using AQGUP algorithm. This whole procedure of unwrapping of photoelastic parameters is discussed in detail in Chapter 2.

Figure 3.8a shows the wrapped isoclinic phasemap with inconsistent zones. Then Fig. 3.8b shows the unwrapped isoclinic phasemap without inconsistent zones. Further, Fig. 3.8c show wrapped isochromatic phasemap without ambiguous zones obtained using unwrapped isoclinic phasemap. To check the accuracy, this phasemap is compared with dark field photoelastic fringe contours obtained from ten-step PST, as shown in Fig. 3.8d. The wrapped isochromatic phasemap is then unwrapped to get a total fringe order over the entire model domain as shown in Fig. 3.8e.

Using automatic software interface written in MATLAB, the principal stress direction (isoclinic) data and principal stress difference obtained from fringe order (N) is collected in an annular region surrounding to the inclusion-tip. Also along with this data, the pixel coordinates of each collected data points and the approximately selected inclusion-tip location by software interface is recorded. For the specimen, the material properties are as follows: Young's modulus, E, is 7.95 MPa, Poisson's ratio, ν, is 0.45 and material fringe value, F_σ, is 0.54 N/mm/fringe. This collected data from an annular region around the inclusion-tip is given as input to the linear least square algorithm as discussed in Section 3.5.2. Using the algorithm, the coefficients of multi-parameter stress field equation for rigid line inclusion are estimated. The inclusion-tip, selected using software interface, acts as an origin for the coordinate system, where a square of 0.4 mm length and mesh-grid of size 0.01 mm is created. Now at each grid point, the strain intensity factor and objective function is computed. The optimal value of strain intensity factor, K_I^ϵ, is selected such way that the objective function has a minimum value in the grid. For that grid point, corresponding strain intensity factor is selected and also the point is considered as inclusion-tip.
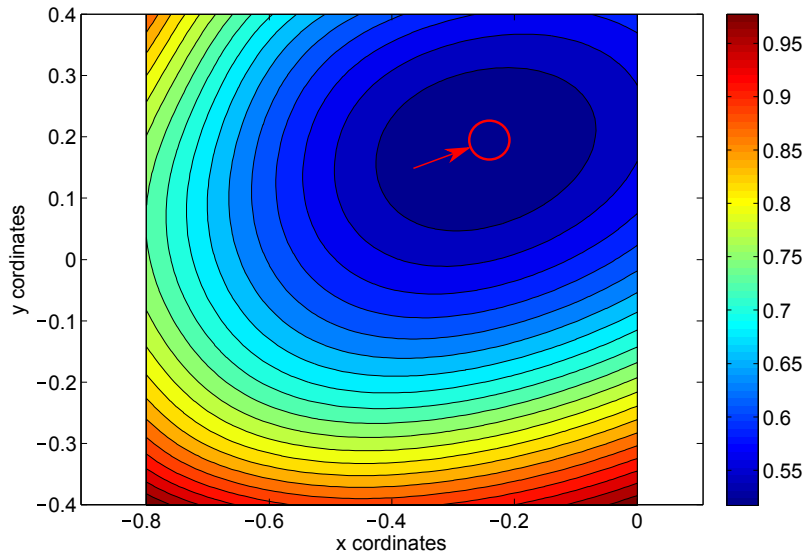
Figure 3.9: Normalised error plot for 7 parameters over the square grid obtained for the experimental estimation of strain intensity factor for rigid line inclusion with a hole specimen.

Table 3.2: Strain intensity factor and corresponding coefficients for different number of parameters

Number of parameters	K_I^ϵ ($\sqrt{mm}$)	A_{I1} ($mm^{1/2}$)	A_{I2}	A_{I3} ($mm^{-1/2}$)	A_{I4} (mm^{-1})	A_{I5} ($mm^{-3/2}$)	A_{I6} (mm^{-2})	A_{I7} ($mm^{-5/2}$)
1-parameter	0.04446	0.2031						
2-parameters	0.02907	0.1328	0.00080					
3-parameters	0.03821	0.1746	-0.0048	0.0031				
4-parameters	0.03612	0.1650	-0.0066	-0.0009	-0.0022			
5-parameters	0.03491	0.1595	-0.0061	-0.0000	0.00539	-0.0003		
6-parameters	0.03396	0.1552	-0.0044	-0.0001	0.00388	-0.0022	0.00024	
7-parameters	0.3419	-0.1562	-0.0049	-0.0001	0.00006	0.0049	-0.0004	0.00004

This marked region is corresponds to the exact inclusion-tip location. Figure 3.10 show the multi-parameter stress field curves fitting to that of experimental fringe contours for different number of parameters. It can be observed that as number parameters are increasing the multi-parameter stress field contours fitting to that of experimental contours. Figure 3.9 shows the normalized error plot for 7 parameters with respect to the selected inclusion-tip and the least error zone is marked. The experimental strain intensity factor, K_I^ϵ, for 7 parameters is found to be 0.03419 $\sqrt{\mathrm{mm}}$ for a rigid line inclusion with a hole specimen. The corresponding convergence error value, J, is found to be 0.000189 MPa^2. The new inclusion-tip location with respect to the manually selected inclusion-tip location is found to be (-0.26, 0.18) estimated using minimum error algorithm. The strain intensity factor for a rigid line inclusion with a hole problem is found numerically also as described in the Chapter 4. It is found to be 0.035024 $\sqrt{\mathrm{mm}}$. Numerical estimated strain intensity factor values has got the deviation of 2.42% with respect to the experimental value. The strain intensity factor is estimated for 1 to 7 parameters. The corresponding K_I^ϵ values and coefficients values are given in Table. 3.2. For confirming the accuracy of results, the multi-parameter stress field curves (blue colour) and experimental fringe contours (red colour) are superimposed over each other as shown in Fig. 3.11. Here, it can be seen that there is good match in the both contours. Furthermore, Fig. 3.12 shows the convergence error, J, plot with respect to the number of parameters, n. Also, Fig. 3.13 shows the strain intensity factor, K_I^ϵ, plot with respect to the number of parameters. It can be observed that after 5 parameters, the K_I^ϵ deviation is very small and same is the case of convergence error plot as shown in Fig. 3.12.

3.7 Closure

In this chapter, we have discussed the experimental estimation of strain intensity factor for the rigid line inclusion with a hole specimen. Firstly, with the definition of strain intensity factor, the multi-
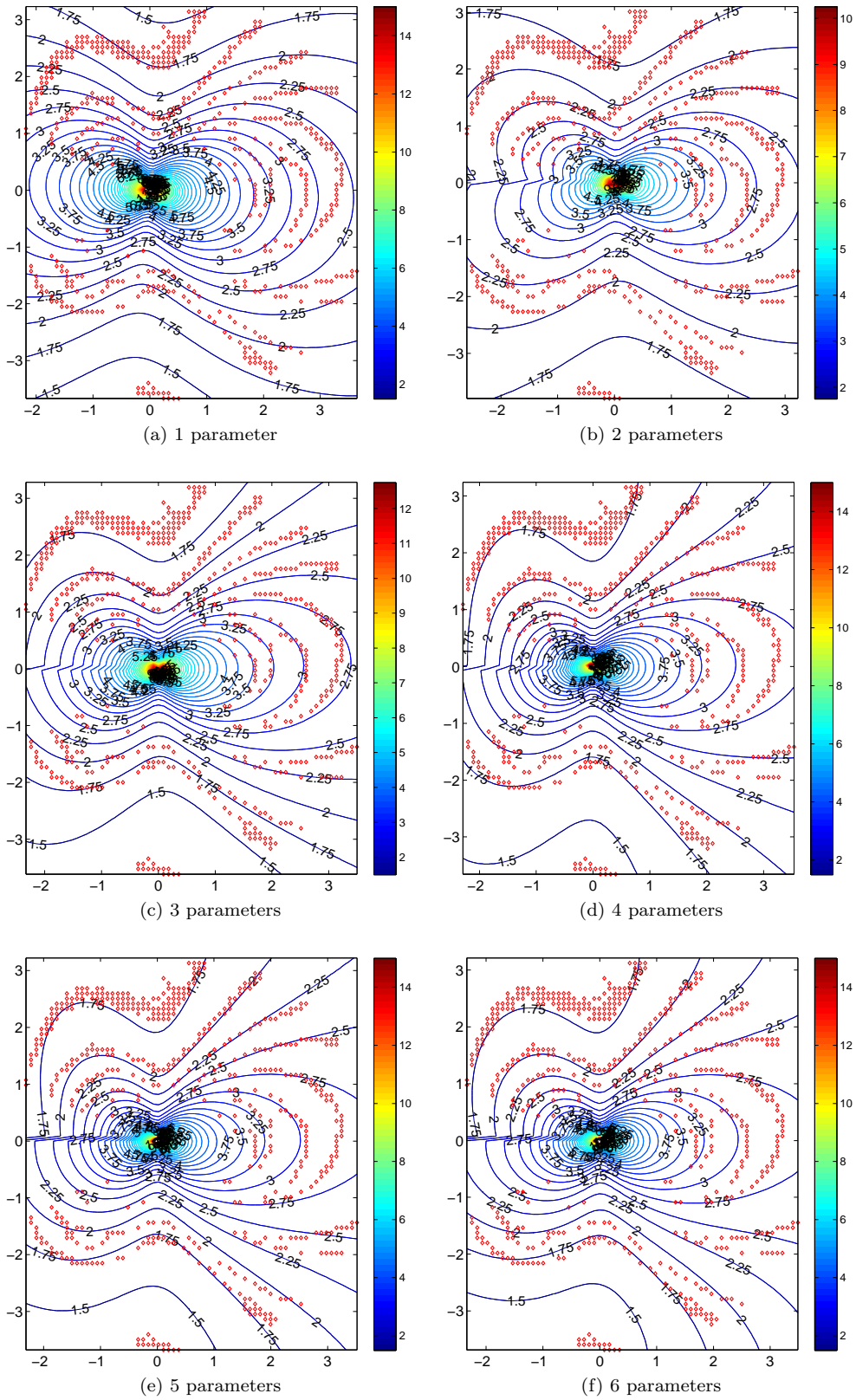
Figure 3.10: Multi-parameter stress field curve (blue colour) fitting for different number of parameters with reconstructed experimental fringe contours (red colour)

40
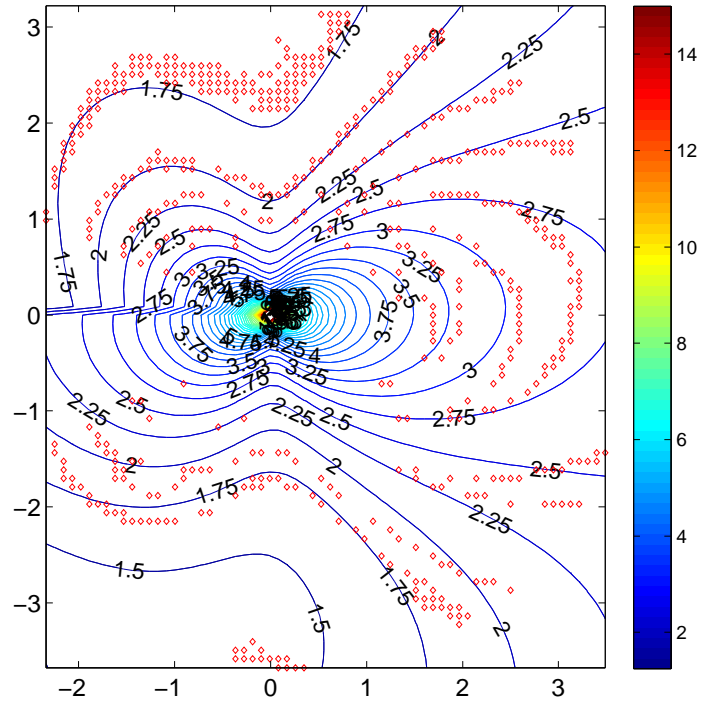
Figure 3.11: Multi-parameter stress field contours for 7 parameters (blue colour) and experimental fringe contours (red colour) are superimposed over each other for rigid line inclusion with a hole specimen loaded at a load of 100 N.
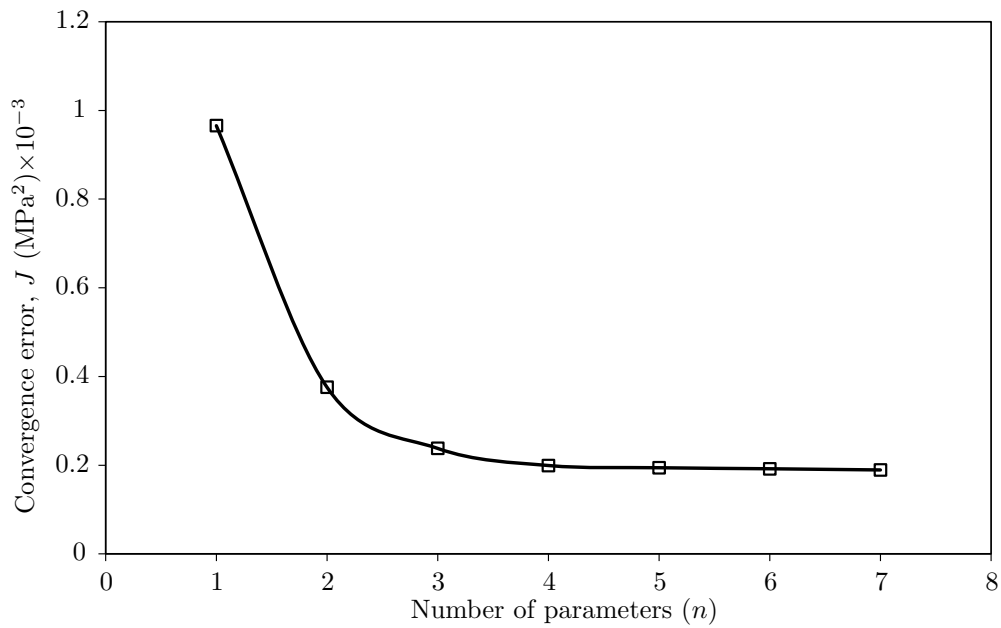
Figure 3.12: Convergence error, J, plot with respect to number of parameters, n, for rigid line inclusion with a hole specimen.

parameter stress field equations for rigid line inclusion embedded in an elastic matrix are derived. These equations are very when estimating the strain intensity factor experimentally. The photoe-
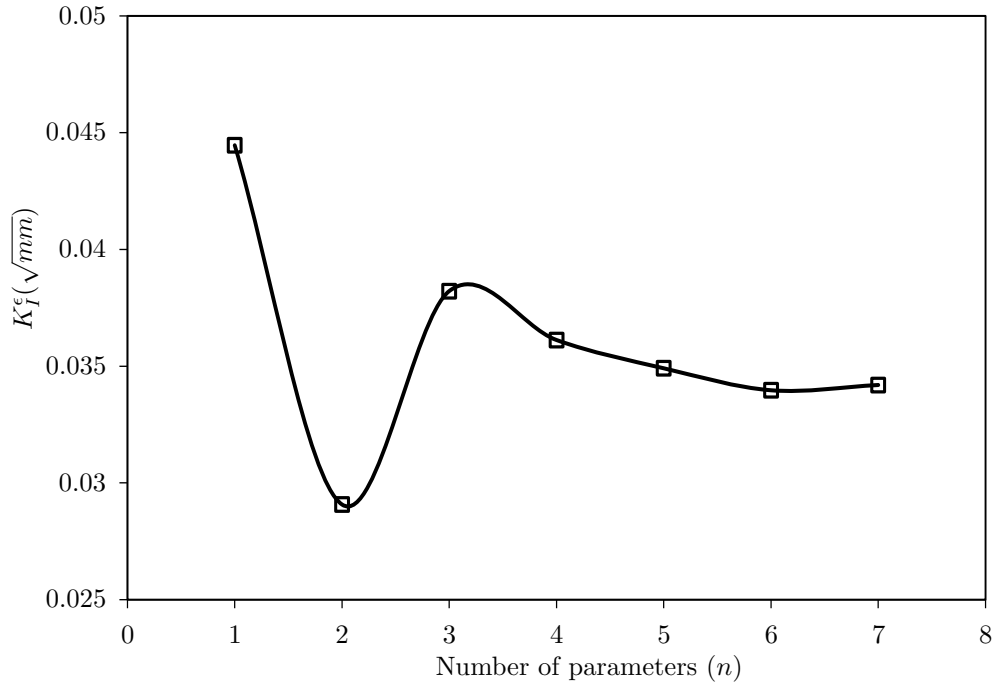
Figure 3.13: Variation of the strain intensity factor with respect to increasing number of parameters for a rigid line inclusion with a hole specimen.

lasticity epoxy specimens are then fabricated for experimentation. Photoelasticity experiments are performed. To get whole field data, ten-step PST technique is used where ten images are captured with different optical elements arrangements. Then unwrapping of isoclinic and isochromatics is performed using AGQUP algorithm. The linear least square method approach is adopted for estimating the strain intensity factor using the multi-parameter stress field equations. This experimental strain intensity factor value is then compared with that of numerically calculated value. It is found to be a good match in these values.

Chapter 4

Numerical Estimation of Strain Intensity Factor for Rigid Line Inclusion

4.1   Introduction

Composite materials are favoured materials in the structure due to their superior mechanical proper-
ties. Main constituents of composite materials are the matrix which binds the reinforcement phases
in place and deforming to distribute the stresses among the constituent reinforcement materials
under an applied force and reinforcements-fibres which gives strength to composite materials. The
strength of this material in the fibre direction is very, but strength in the lateral direction is very
low. This problem can be overcome by placing the fibres in the required strength direction. But the
aligning the fibres in the correct direction is a difficult task and also a slight misalignment of fibres
can reduce strength drastically in that direction. In this cases, one can use the laminate which has
in-plane isotropy, and this can be achieved using short-fibre-reinforces-polymers.

In SFRP, fibre and matrix share the applied load. Hence they have superior strength and elastic
stiffness compared to parent materials. However, the fibres can leads to singular stress field at the
fibres end. If voids are present in the composite, then this singular stress field can cause void growth,
coalesce and also micro-buckling. Hence it important to study the fibre-matrix interaction in case
of SFRP. Therefore, in the literature, this problem is extensively studied as rigid line inclusion
embedded in an elastic matrix. The defects can of different types, cracks, voids, inclusions or second
phase material, to name a few, which ultimately affects the strength of the structure. These defects
can occur due to second phase particle, debond in composite, fabrication process such as welding,
heat treatment and in-service life due to fatigue crack, environment assisted or creep crack etc.
Many catastrophic structural failures have occurred due to brittle fracture. Voids in the composite
materials are potential defects and have great influence on the mechanical properties. We know that
in SFRP, the singular stress field is present at the fibre end and presence of voids near the fibre end
may increase its intensity. There are two reasons for modelling the fibre as a rigid line inclusion.
First is the thickness of the steel inclusion, that we have used, is very small compared to other

specimen dimensions. Second is the strength of the steel is very high compared to the strength of matrix-resin which is such true case in SFRP where fibre has more strength than that of a matrix material.

In this chapter, the numerical method for the estimation of strain intensity factor is discussed. In the first, the duality principle along with Stroh formulation is used to obtain the singular stress field at the inclusion-tip. It is justified that the strain intensity factor is necessary to use to quantify the singularity which is independent of the material properties of the matrix. In the section 4.2, the numerical method based on the reciprocal theorem to estimate the strain intensity factor, K_I^ϵ, for rigid line inclusion embedded in an elastic matrix using the asymptotic and actual elastic fields near an inclusion tip is discussed. The actual stress field is obtained using a finite element analysis in ABAQUS. This numerical model is then verified using the digital photoelasticity technique. The fringe contours from photoelasticity experiment and numerical method are compared. Further, the results for the variation of strain intensity factor for three parameters, namely diameter of a hole, length of line inclusion and the distance between the inclusion and a hole are discussed. In the section 4.4, closure for this chapter is summarized.

4.2   Numerical estimation of strain intensity factor

For the estimation of strain singularity for arbitrary geometry, herein we have adopted a numerical framework based on the reciprocal theorem. Following procedure is described in [35, 36, 37]. For the further analysis, we need the general solution for asymptotic stress field near the inclusion-tip. We have the standard elasticity solution for rigid line inclusion in the polar coordinates obtained from symmetric stress function as follows,

$$\sigma_{rr} = -2\mu H \lambda r^{\lambda-1}[(\lambda-3)\cos((\lambda-1)\theta) - (\kappa+\lambda)\cos((\lambda+1)\theta)], \tag{4.1}$$

$$\sigma_{\theta\theta} = 2\mu H \lambda r^{\lambda-1}[(\lambda+1)\cos((\lambda-1)\theta) - (\kappa+\lambda)\cos((\lambda+1)\theta)], \tag{4.2}$$

$$\sigma_{r\theta} = 2\mu H \lambda r^{\lambda-1}[(\lambda-3)\cos((\lambda-1)\theta) - (\kappa+\lambda)\cos((\lambda+1)\theta)], \tag{4.3}$$

$$\epsilon_{rr} = H \lambda r^{\lambda-1}[(\kappa-\lambda)\cos((\lambda-1)\theta) + (\kappa+\lambda)\cos((\lambda+1)\theta)], \tag{4.4}$$

$$\epsilon_{\theta\theta} = H \lambda r^{\lambda-1}[(\kappa+\lambda-2)\cos((\lambda-1)\theta) - (\kappa+\lambda)\cos((\lambda+1)\theta)], \tag{4.5}$$

$$\epsilon_{r\theta} = H \lambda r^{\lambda-1}[(\lambda-1)\sin((\lambda-1)\theta) - (\kappa+\lambda)\sin((\lambda+1)\theta)], \tag{4.6}$$

$$u_r = H \lambda r^{\lambda}[(\kappa-\lambda)\cos((\lambda-1)\theta) + (\kappa+\lambda)\cos((\lambda+1)\theta)], \tag{4.7}$$

$$u_\theta = H \lambda r^{\lambda}[(\kappa+\lambda)\sin((\lambda-1)\theta) - (\kappa+\lambda)\sin((\lambda+1)\theta)], \tag{4.8}$$

where H is a coefficient depending on the boundary conditions, μ is shear modulus,

$$\lambda = \pm\frac{n}{2}, \qquad n \text{ is an integer}, \tag{4.9}$$

and (r, θ) are polar co-ordinates defined in Fig. 4.1.

The singular displacement and stress fields near the inclusion-tip can be written as

$$u_i = Hr^\lambda g_i(\lambda, \theta), \tag{4.10}$$

$$\sigma_{ij} = 2\mu Hr^{\lambda-1} f_{ij}(\lambda, \theta), \tag{4.11}$$
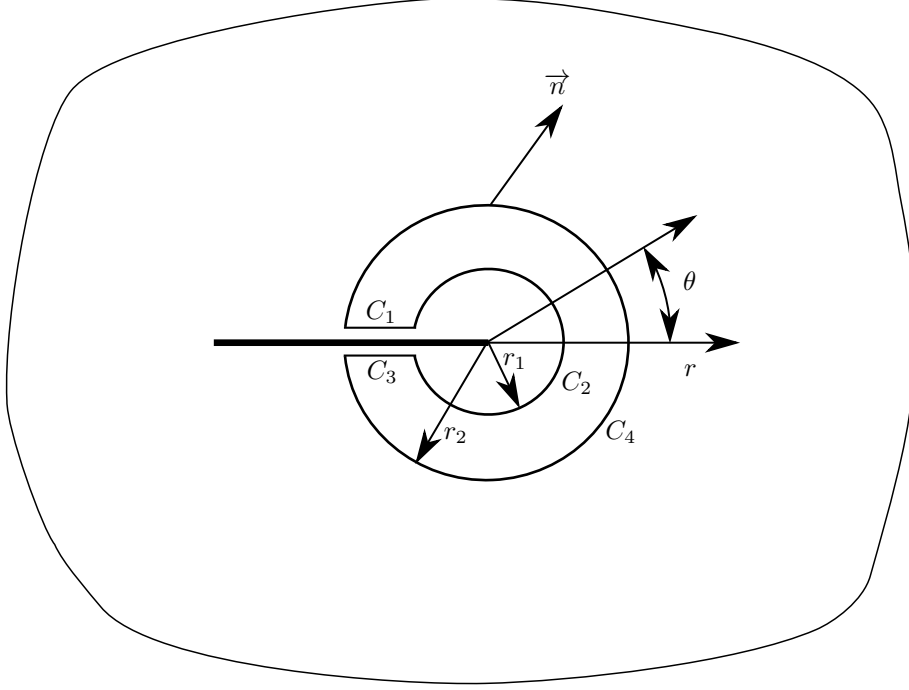
Figure 4.1: Counters around the inclusion tip to evaluate area integral.

where $[i, j] \in [r, \theta]$, f_{ij} and g_i are known functions of λ and θ deduced from the Eqn. 4.1-4.3 and 4.7-4.8 respectively. Comparing Eqn. 3.4 and 4.4, we can say that H is the strain intensity factor. The following described procedure of calculating the strain intensity factor is adopted from Akisanya and Fleck [36] and Carpenter and Byers [37]. We know that the reciprocal theorem in the form as

$$\oint_C (\sigma_{ij} u_i^* - \sigma_{ij}^* u_i) n_j dS = 0, \tag{4.12}$$

where n_j is the unit normal to the contour C consists of C_1, C_2, C_3 and C_4 segments, whose outer radius is r_2 and the inner radius is r_1 as shown in Fig. 4.1. In the above equation (σ_{ij}, u_j) are the actual stress and displacement fields and (σ_{ij}^*, u_j^*) are suitably chosen auxiliary stress and displacement fields that satisfy the boundary conditions. The auxiliary fields are chosen to be the asymptotic fields with $\lambda^* = -\lambda$ as

$$u_i^* = H^* r^{\lambda^*} g_i(\lambda^*, \theta), \tag{4.13}$$

$$\sigma_{ij}^* = 2\mu H^* r^{\lambda^*-1} f_{ij}(\lambda^*, \theta). \tag{4.14}$$

One can subdivide the contour C into four parts as C_1, C_2, C_3 and C_4 as shown in Fig. 4.1. Also, we can write the Eqn. 4.12 as summation of integrals over the contours C_1, C_2, C_3 and C_4. The

45

integral in Eqn. 4.12 vanishes over C_1 and C_3 because of the displacement boundary conditions. Hence the equation can be rewritten as

$$\int_{C_2} (\sigma_{ij} u_i^* - \sigma_{ij}^* u_i) n_j dS = -\int_{C_4} (\sigma_{ij} u_i^* - \sigma_{ij}^* u_i) n_j dS. \tag{4.15}$$

For the line integral along the inner contour $C_2, (\sigma_{ij}, u_j)$ is taken to be the asymptotic elastic fields (in which H is unknown), and for the line integral along the outer contour $C_4, (\sigma_{ij}, u_j)$ are taken from the actual elasticity solution. First, we consider the integral along the contour C_4. Instead of performing a contour integral we perform as area integral. For this we define a scalar $m \equiv (r_2 - r)/(r_2 - r_1)$ which is unity on C_4 and vanishes on C_2. Now we can write,

$$-\int_{C_4} (\sigma_{ij} u_i^* - \sigma_{ij}^* u_i) n_j dS = -\int_C m(\sigma_{ij} u_i^* - \sigma_{ij}^* u_i) n_j dS, \tag{4.16}$$

$$= -\int_A (\sigma_{ij} u_i^* - \sigma_{ij}^* u_i) \frac{\partial m}{\partial x_j} dA \tag{4.17}$$

$$= H^* \int_A \left(\sigma_{ij} r^{\lambda^*} g_i(\lambda^*, \theta) - u_i r^{\lambda^*-1} 2\mu f_{ij}(\lambda^*, \theta) \right) \frac{\partial m}{\partial x_j} dA, \tag{4.18}$$

where the last quantity is obtained using the divergence theorem. We now consider the line integral along C_2. Substituting asymptotic elastic field and auxiliary field on the left side of the Eqn. 4.15 the line integral becomes

$$\int_{C_2} (\sigma_{ij} u_i^* - \sigma_{ij}^* u_i) n_j dS = 2\mu H H^* \int_{-\pi}^{\pi} (f_{ij}(\lambda) g_i(\lambda^*) - g_i(\lambda) f_{ij}(\lambda^*)) n_j d\theta \tag{4.19}$$

$$= c_1 H H^*, \tag{4.20}$$

where

$$c_1 = 2\pi \int_{-\pi}^{\pi} (f_{ij}(\lambda) g_i(\lambda^*) - g_i(\lambda) f_{ij}(\lambda^*)) n_j d\theta. \tag{4.21}$$

The value of c_1 can be calculated by performing the numerical integration. Note that c_1 is independent of r; this is due to choice of $\lambda^* = -\lambda$. Finally , Eqn. 4.15 can be rewritten using Eqns. 4.18 and 4.20 as

$$H = -\frac{1}{c_1} \int_A \left(\sigma_{ij} r^{\lambda^*} g_i(\lambda^*, \theta) - u_i r^{\lambda^*-1} 2\mu f_{ij}(\lambda^*, \theta) \right) \frac{\partial m}{\partial x_j} dA. \tag{4.22}$$

In the above equation, the actual stress fields (σ_{ij}, u_j) are computed using the finite elements, whereas the auxiliary fields (σ_{ij}^*, u_j^*) are calculated by Eqn.4.13. The finite element analysis is carried out using the commercial analysis software ABAQUS 6.14 [38]. The stress and displacement field from FEA is given to a script written in MATLAB [39] to estimate the strain intensity factor using Eqn.4.22. Validation of these finite element analysis model is carried out by comparing the fringe pattern of surrounding of inclusion tip obtained from the FEA with that of photoelasticity experiments.

4.3 FEA modelling and results

A rigid line inclusion with a hole embedded in finite matrix is modelled in a ABAQUS 6.14 as shown in fig. 4.2.
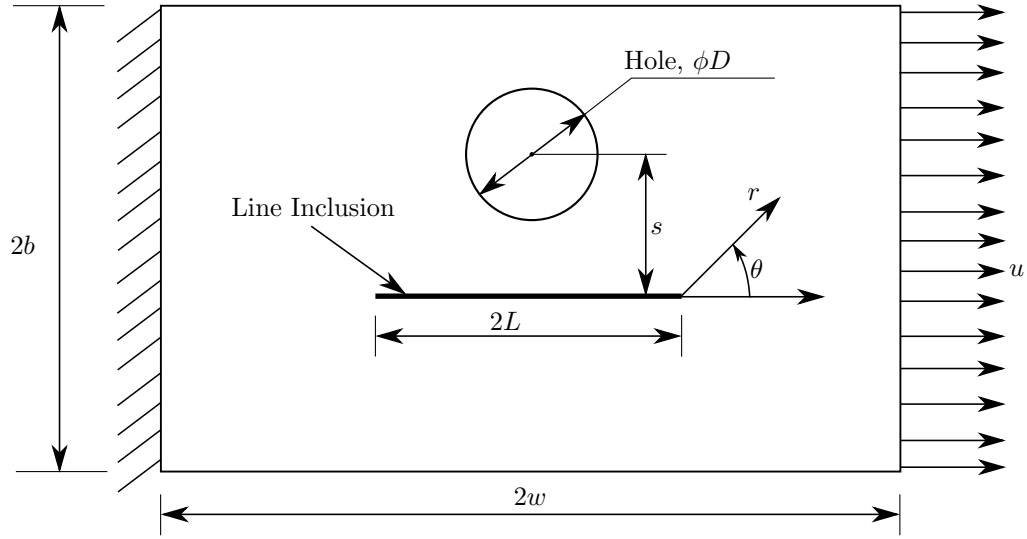
Figure 4.2: A FEA model of a rigid line inclusion with a hole embedded in a finite matrix for ABAQUS.

A primary motive of FEA is to get stress field near the tip of the rigid line inclusion as require it for numerical strain intensity factor estimation. The validation of this model is important because we model the rigid line inclusion using the constraint that the nodes lying on the inclusion line deform rigidly. The validation of this numerical model is carried using the experimental technique, digital photoelasticity.

A 2D plate is modelled with following dimensions: $2w = 200mm$ and $2b = 100mm$ with the dimensions rigid line inclusion length, $2L$, the diameter of the hole, D, and distance between rigid line inclusion and a hole centre, s, are variables, as shown in Fig. 4.2. The plate is discretised using 8-nodded plane strain elements abbreviated as CPE8H in ABAQUS. The quarter-point element is used to capture square root singularity at the tip of inclusion more accurately. A mesh convergence study is performed to arrive at the number of circumferential element at the tip of inclusion, as shown in fig. 4.3. It is found to be 176 elements in the circumferential and 120 along the radial direction are enough. Figure 4.4 shows generated mesh for the whole model. A dense mesh is used at the tip of line inclusion because it is a high-stress concentration zone and also it is the area of interest to us. Away from the inclusion, a coarse mesh is used to reduce the total number of degrees of freedom. The rigid inclusion is modelled as a rigid line defined by rigid constraint in ABAQUS. The degrees of freedom in x-direction of the nodes on the boundary edge at $x = -w$ is arrested. A tensile load of 150 N magnitudes in x-direction on the boundary edge at $x = +w$ is applied, and these results are then compared qualitatively with photoelastic results. Furthermore, using the stress obtained from ABAQUS, strain intensity factor is calculated and compared with that of obtained from photoelasticity experiment.

The dark field isochromatic contours plot is generated using nodal stress field data from the FEA [40]. A brief description of the fringe plotting algorithm is given in Appendix A. These contours are then compared with that of experimental contours, and we found a good agreement between them, as shown in fig. 4.5.
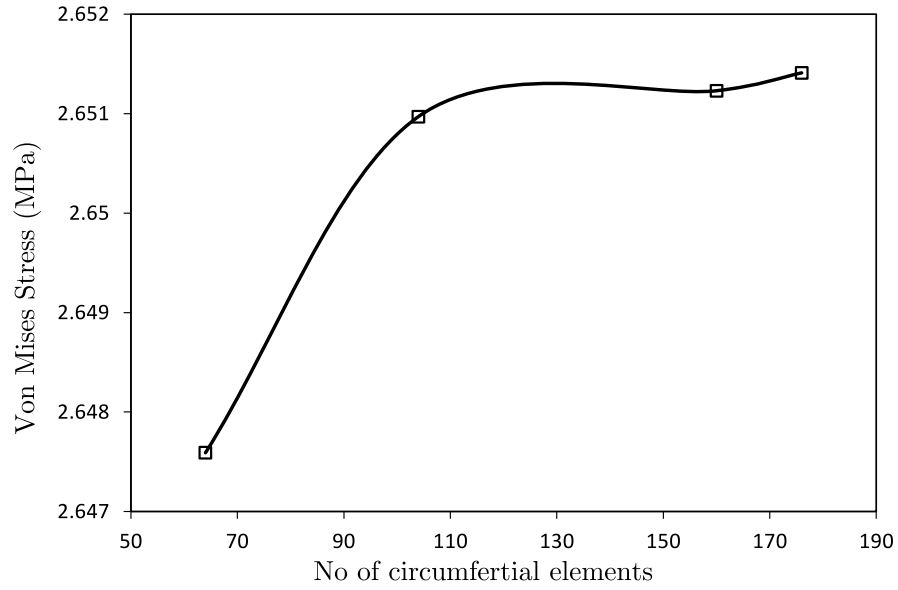
Figure 4.3: Mesh convergence study for present model for circumferential number of elements.

(a)

(b)
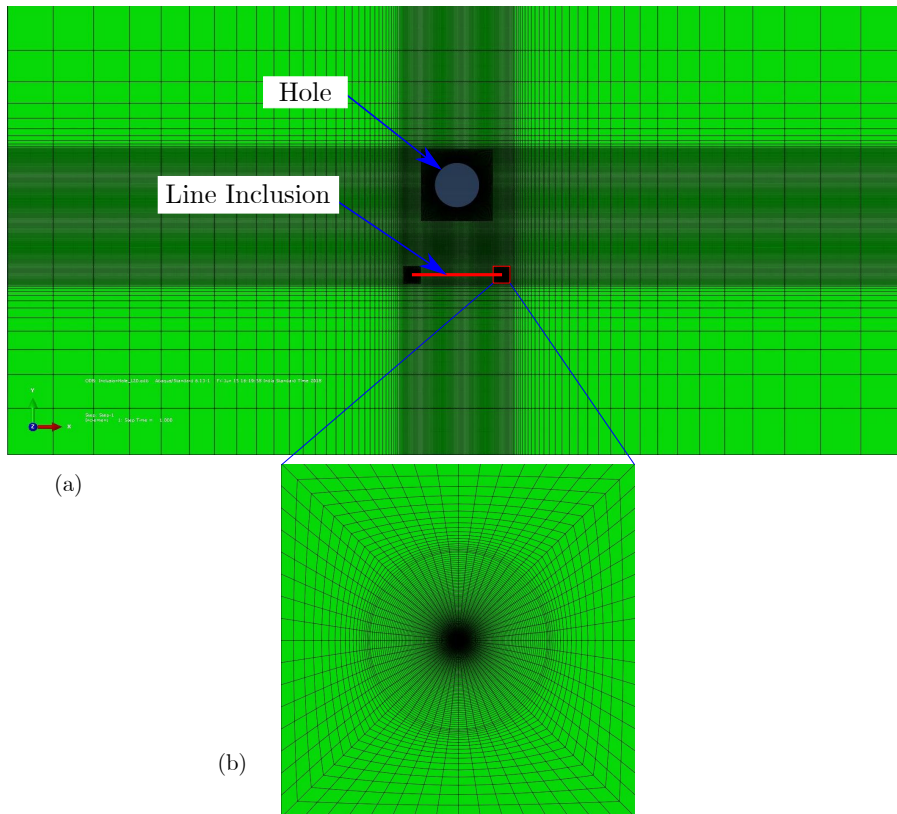
Figure 4.4: A meshed FEA rigid line inclusion with a hole model, (a) whole meshed model showing line inclusion and hole and (b) a zoomed view of mesh used at the inclusion-tip.

4.3.1 FEA results for strain intensity factor

After validating the FEA model of the present problem using digital photoelasticity technique, the effect of a hole on the strain singularity at the tip of rigid line inclusion is studied. The variation of
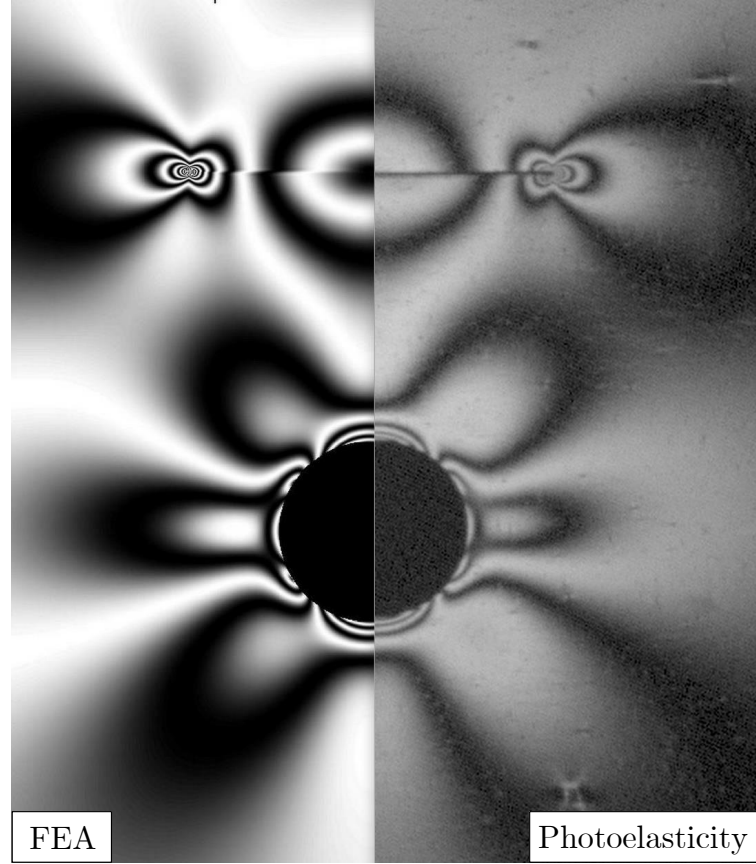
Figure 4.5: Qualitative validation of FEA model using photoelasticity. Left half represents fringe contour plotted from FEA solution and right half represents experimental dark field photoelastic fringe contour obtained, for a tensile load of 150 N.

strain intensity factor with respect to three parameters, namely, the diameter of a hole, D, length of line inclusion, L, and the distance between the line inclusion and a hole, s, as shown in Fig. 4.2, is investigated. In the FEA model, the degrees of freedom in x-direction of the nodes on the boundary edge at $x = -w$ is arrested. A tensile load of magnitude 0.1 MPa in x-direction on the boundary edge at $x = +w$ is applied. In the entire FEA analysis, load, boundary condition, model dimensions, etc. are kept constant, and only D, L and s are changed. The normalised strain intensity factor (NSIF) is calculated using the relation,

$$\text{NSIF} = \frac{\text{strain intensity factor with hole}}{\text{strain intensity factor without hole}}.$$ (4.23)

The variation of normalised strain intensity factor is plotted for different configuration and inferences are discussed below. First of all, from Figs. 4.6, 4.7 and 4.8 it is clear that with the presence of hole the strain intensity factor increases. Fig. 4.6 shows the NSIF variation with respect to the distance between line inclusion and hole centre, s. To get this plot, we have kept the diameter of the hole, $D = 10$ mm and inclusion length, $L = 20$ mm as constant. As the hole is coming towards the inclusion NSIF is increasing, but when it nearer to inclusion, the NSIF increase rate is more. Also as hole moving further its effect is vanishing, hence NSIF is reaching to unity.
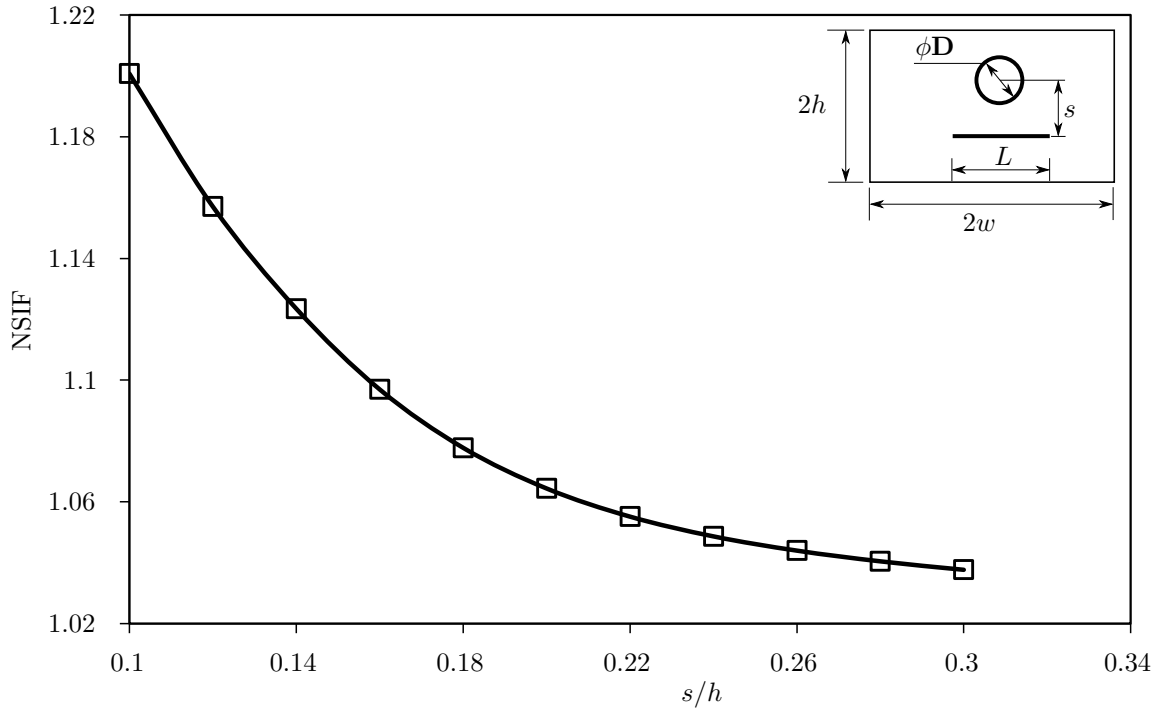
Figure 4.6: Variation of NSIF with respect to the increasing distance between the line inclusion and hole centre, s.
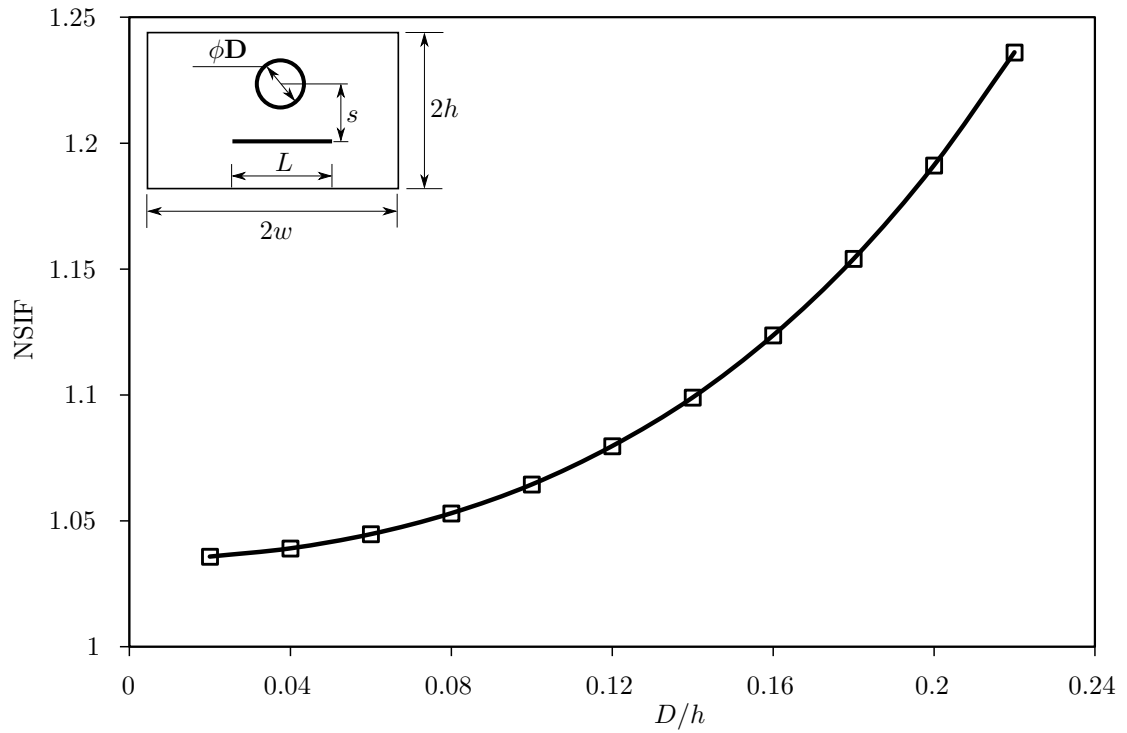
Figure 4.7: Variation of NSIF with respect to the increasing diameter of the hole, D.
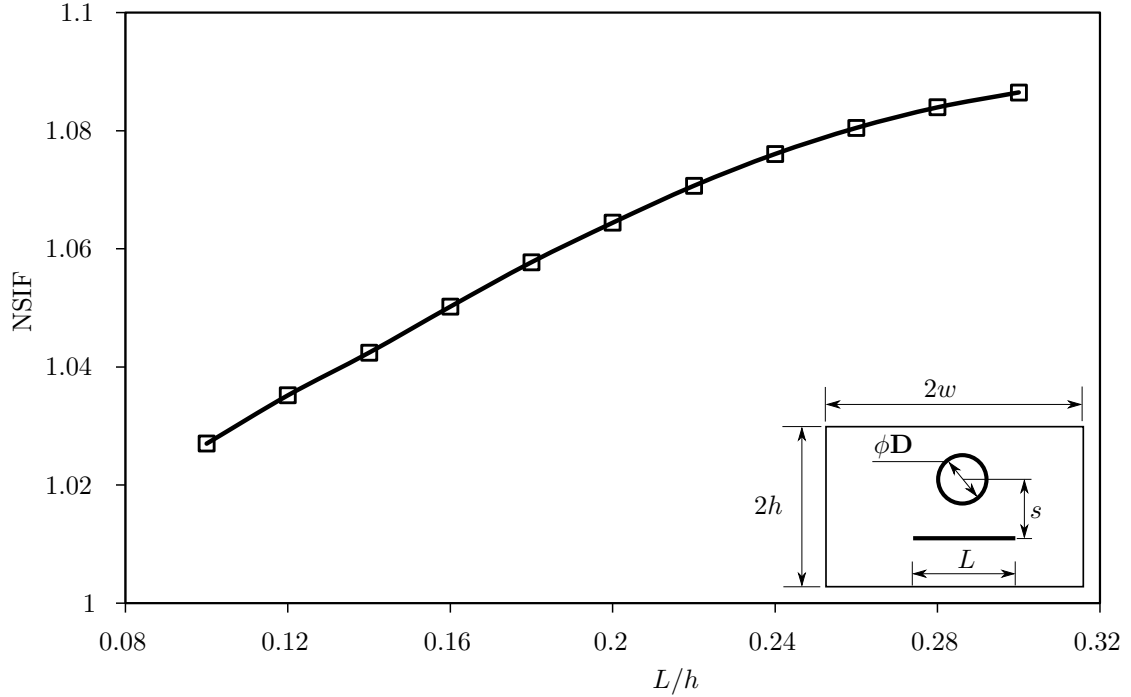
Figure 4.8: Variation of NSIF with respect to the increasing length of line inclusion, L.

Figure 4.7 shows the NSIF variation with respect to the diameter of the hole, D. To get this plot, we have kept the distance between line inclusion and hole centre, $s = 20$ mm and inclusion length, $L = 20$ mm as constant. For the smaller diameter hole, the increase rate of NSIF is less and also as the hole diameter is increasing, increase rate of NSIF is also increasing.

Figure 4.8 shows NSIF variation with respect to the length of line inclusion, L. To get this plot, we have kept the distance between line inclusion and hole centre, $s = 20$ mm and the diameter of the hole, $D = 10$ mm as constant. An important thing to notice here is an increase in NSIF with respect inclusion length is less compared to that of distance, s, and hole diameter, D. Also, for the shorter inclusion length, increase rate of NSIF is almost same, but for longer inclusion length increase is keep on decreasing. This variation is probably because as the inclusion length increases its side surface area is also increases, and we know that this area is also responsible for the load transfer from the matrix to the inclusion.

4.4 Closure

Voids in SFRP is studied for a simple 2D case and modelled as rigid line inclusion with a hole. A strain Instead of stress intensity factor, strain intensity factor is used which independent of the material properties. Using reciprocal theorem and FEA, strain intensity factor has estimated numerically rigid line inclusion with a hole. Further, the FEA model is validated using the digital photoelasticity technique qualitatively and quantitatively, and the comparison is quite good.

Normalized strain intensity factor (NSIF) is defined and its variation with respect to three parameters, viz., the distance between line inclusion and hole centre, inclusion length and hole diameter is

investigated. It is found that presence of the hole always increases the strain intensity factor value. This can be because of the presence of a hole expose the fibre end singularity to the boundary effect.

Chapter 5

Conclusions and Recommendations

A rigid line inclusion with a hole embedded in an elastic matrix problem was taken to study. The primary focus was on finding the effect of presence of a void nearby to fibre end in case of short fibre composites. Here, the fibres are modelled as rigid line inclusion and void as for its simplest 2D case, hole. Strain intensity factor, which is independent of the matrix material properties and hence makes it more suitable for inclusion problems, is used for quantifying the singularity at the inclusion-tip. Using numerical modelling in ABAQUS, the variation of strain intensity factor is studied for three parameters namely diameter of a hole, length of line inclusion and the distance between the inclusion and a hole. For simulation purpose, a ABAQUS python scripting is written as it is very helpful when estimating the stress and other data surrounding to the inclusion-tip. A numerical methodology is adopted for calculation of strain intensity factor as described by Pratap P. et. al [20]. Furthermore, the numerical model is validated qualitatively and quantitatively using the experimental technique, digital photoelasticity.

From numerical study, it is concluded that the presence of a hole nearby to the inclusion-tip always increases the strain intensity factor. The reason can be stated as follows: as hole can be considered as traction free boundary, hence the inclusion-tip singularity exposed to the boundary effect and hence increases the strain intensity factor. Furthermore, the severity of presence of a hole is also checked. Following points can be highlight from this work:

(a) presence of hole/free boundary near to singularity always increases values of fracture parameter, here strain intensity factor,

(b) as hole comes nearer to the inclusion strain intensity factor increases,

(c) as diameter of the hole increases, the strain intensity factor also increases and for higher diameter the increase rate also increases and

(d) as inclusion length increases strain intensity factor also increases but for higher length increase rate reduces. This decrease in increase rate with inclusion length can be reasoned as follows: as inclusion length increases, inclusion has more side area which can be used during the load transfer from matrix to inclusion and this reduces stress concentration at the inclusion-tip, meaning reduces strain intensity factor.

References

[1] D. Hull and T. W. Clyne. An Introduction to Composite Materials. 2nd edition. Cambridge University Press, 1996.

[2] S.-Y. Fu, Y.-W. Mai, and B. Lauke. Science and Engineering of Short Fibre Reinforced Polymers Composites. Woodhead Pub, Cambridge, UK, 2009.

[3] F. Rezaei, R. Yunus, N. A. Ibrahim, and E. S. Mahdi. Development of Short-Carbon-Fiber-Reinforced Polypropylene Composite for Car Bonnet. *Polymer-Plastics Technology and Engineering* 47, (2008) 351–357.

[4] T. Wang and Y. Li. Design and analysis of automotive carbon fiber composite bumper beam based on finite element analysis. *Advances in Mechanical Engineering* 7, (2015) 1687814015589,561.

[5] K. Hamza, A. Y. Shash, and M. Abdrabou. Application of Short Fibers Reinforced Composites in Power Transmission Coupling. *Latin American Journal of Solids and Structures* 14, (2017) 1789 – 1803.

[6] E. Kurkin and V. Sadykova. Application of Short Fiber Reinforced Composite Materials Multilevel Model for Design of Ultra-light Aerospace Structures. *Procedia Engineering* 185, (2017) 182 – 189. Electric Propulsions and Their Application.

[7] R. L. Orfice, L. L. Hench, and A. B. Brennan. Effect of Particle Morphology on the Mechanical and Thermo-Mechanical Behavior of Polymer Composites. *Journal of the Brazilian Society of Mechanical Sciences* vol.23.

[8] S. Y. Fu and B. Lauke. The Elastic Modulus of misaligned Short-Fiber-Reinforced Polymers. *Composites Science and Technology* 58, (1998) 389 – 400.

[9] A. Vaxman, M. Narkis, A. Siegmann, and S. Kenig. Void formation in short-fiber thermoplastic composites. *Polymer composites* 10, (1989) 449–453.

[10] N. Shakya, J. Roux, and A. Jeswani. Effect of resin viscosity in fiber reinforcement compaction in resin injection pultrusion process. *Applied Composite Materials* 20, (2013) 1173–1193.

[11] A. Njionhou, F. Berthet, and B. Castanié. Effects of process parameters on the mechanical properties and morphology of stitched and non-stitched carbon/epoxy liquid resin-infused NCF laminate, out of autoclave and out of oven. *The International Journal of Advanced Manufacturing Technology* 65, (2013) 1289–1302.

[12] F. Boey and S. Lye. Void reduction in autoclave processing of thermoset composites: Part 1: High pressure effects on void reduction. *Composites* 23, (1992) 261–265.

[13] J. E. Little, X. Yuan, and M. I. Jones. Characterisation of voids in fibre reinforced composite materials. *NDT & E International* 46, (2012) 122–127.

[14] P. T. Curtis, M. G. Bader, and J. E. Bailey. The stiffness and strength of a polyamide thermoplastic reinforced with glass and carbon fibres. *Journal of Materials Science* 13, (1978) 377–390.

[15] C. Atkinson. Some ribbon-like inclusion problems. *International Journal of Engineering Science* 11, (1973) 243–266.

[16] Z. Wang, H. Zhang, and Y. Chou. Characteristics of the elastic field of a rigid line inhomogeneity. *Journal of Applied Mechanics* 52, (1985) 818–822.

[17] N. I. Muskhelishvili. Some basic problems of the mathematical theory of elasticity. 4th edition. Springer Science & Business Media, 2013.

[18] R. Ballarini. An integral equation approach for rigid line inhomogeneity problems. *International Journal of Fracture* 33, (1987) R23–R26.

[19] G. Noselli, F. Dal Corso, and D. Bigoni. The stress intensity near a stiffener disclosed by photoelasticity. *International journal of fracture* 166, (2010) 91–103.

[20] P. Patil, S. Khaderi, and M. Ramji. Numerical estimation of strain intensity factors at the tip of a rigid line inclusion embedded in a finite matrix. *Engineering Fracture Mechanics* 172, (2017) 215 – 230.

[21] H. Ishikawa and Y. Kohno. Analysis of stress singularities at the corner point of square hole and rigid square inclusion in elastic plates by conformal mapping. *International Journal of Engineering Science* 31, (1993) 1197 – 1213.

[22] Y. Kohno and H. Ishikawa. Analysis of stress singularities at the corner point of lozenge hole and rigid lozenge inclusion in elastic plates by conformal mapping. *International Journal of Engineering Science* 32, (1994) 1749 – 1768.

[23] E. Gdoutos. Interaction effects between a crack and a circular inclusion. *Fibre Science and Technology* 15, (1981) 173 – 185.

[24] R. Li and A. Chudnovsky. Energy Analysis of Crack interaction with an Elastic Inclusion. *International Journal of Fracture* 63, (1993) 247–261.

[25] S. Natarajan, P. Kerfriden, D. R. Mahapatra, and S. P. A. Bordas. Numerical Analysis of the Inclusion-Crack Interaction by the Extended Finite Element Method. *International Journal for Computational Methods in Engineering Science and Mechanics* 15, (2013) 26–32.

[26] M. Ayatollahi, S. Razavi, and H. Chamani. Fatigue Life Extension by Crack Repair Using Stophole Technique under Pure Mode-I and Pure mode-II Loading Conditions. *Procedia Engineering* 74, (2014) 18–21.

[27] S. Thomas, M. Mhaiskar, and R. Sethuraman. Stress intensity factors for circular hole and inclusion using finite element alternating method. *Theoretical and Applied Fracture Mechanics* 33, (2000) 73 – 81.

[28] H. Sulym, L. Andrusiv, and Y. Pasternak. Interaction of thin inclusion with circular hole in the elastic isotropic medium. *ZAMM - Journal of Applied Mathematics and Mechanics / Zeitschrift fr Angewandte Mathematik und Mechanik* 95, (2014) 1282–1289.

[29] K. Ramesh and G. Lewis. Digital photoelasticity: advanced techniques and applications. *Applied Mechanics Reviews* 55, (2002) B69.

[30] M. Ramji and R. Prasath. Sensitivity of isoclinic data using various phase shifting techniques in digital photoelasticity towards generalized error sources. *Optics and Lasers in Engineering* 49, (2011) 1153–1167.

[31] M. Ramji and K. Ramesh. Adaptive Quality Guided Phase Unwrapping Algorithm for Whole-Field Digital Photoelastic Parameter Estimation of Complex Models. *Strain* 46, (2010) 184–194.

[32] K. Ramesh, S. Gupta, and A. A. Kelkar. Evaluation of stress field parameters in fracture mechanics by photoelasticityrevisited. *Engineering Fracture Mechanics* 56, (1997) 25–45.

[33] M. Ramji and K. Ramesh. Whole field evaluation of stress components in digital photoelasticityissues, implementation and application. *Optics and Lasers in Engineering* 46, (2008) 257–271.

[34] M. Ramji and R. Prasath. Sensitivity of isoclinic data using various phase shifting techniques in digital photoelasticity towards generalized error sources. *Optics and Lasers in Engineering* 49, (2011) 1153–1167.

[35] Z. Qian and A. Akisanya. Wedge corner stress behaviour of bonded dissimilar materials. *Theoretical and Applied Fracture Mechanics* 32, (1999) 209 – 222.

[36] A. Akisanya and N. Fleck. Interfacial cracking from the freeedge of a long bi-material strip. *International Journal of Solids and Structures* 34, (1997) 1645 – 1665.

[37] B. C. Carpenter WC. A path independent integral for computing stress intensities for V-notched cracks in a bi-material. *International Journal of Fracture* 35(4), (1987) 24568.

[38] Abaqus. Dassault Systems, Simulia Corporation, Providence, RhodeIsland, USA version 6.14.

[39] MATLAB. The MathWorks Inc., Natick, Massachusetts version 9.0 (R2016a).

[40] K. Ramesh, A. Yadav, and V. A. Pankhawalla. Plotting of fringe contours from finite element results. *International Journal for Numerical Methods in Biomedical Engineering* 11, (1995) 839–847.

Appendix

Appendix A: Ten-step PST photoelastic images

(a)

(b)

(c)

(d)

(e)

(f)

(g)

(h)

(i)

(j)
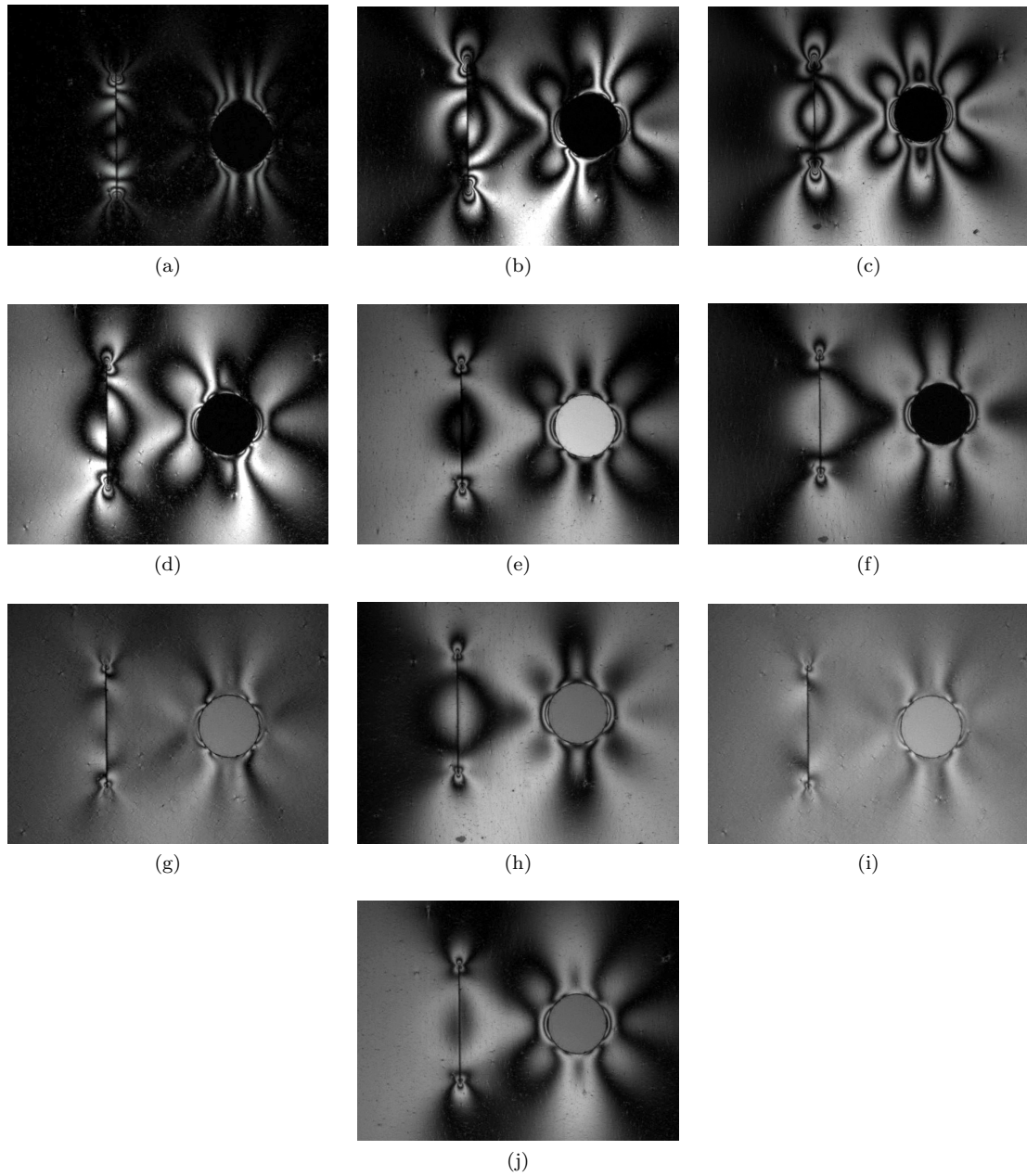
Figure 1: Experimentally recorded phase shifted images of line inclusion with a hole (150 N) corresponding to ten-step phase shifting algorithm as per the sequence given in table 2.1.

Appendix B: Python script

Python script for ABAQUS modelling for rigid line inclusion with a hole

```python
## A Python Script for the ABAQUS
## A problem of A plate with an inclusion and a hole
import numpy as np
import numpy
import os
from part import *
from material import *
from section import *
from assembly import *
from step import *
from interaction import *
from load import *
from mesh import *
from optimization import *
from job import *
from sketch import *
from visualization import *
from connectorBehavior import *
from abaqusConstants import*
from math import*
import sys
from abaqus import *
from odbAccess import *
import xyPlot
import displayGroupOdbToolset as dgo
Mdb()
numpy.set_printoptions(threshold='nan')
path = "D:\\Satish\\numerical\\fringe plot\\E100"
os.chdir(path)
### Parameters to be Specified ###
w=100.00;       # Half Width of plate
b=113.23/2.0; # Half Height if plate
l=10.00;        # Half Inclusion length
r3=5.00;      # Radius of the hole
s=20.00; # vertical distance b/w inclusion and hole
a=s/2
dt = 1e-3
###
jbname = 'InclusionHole'
if (r3==5.00) and (s==20.00):
        jbname = jbname + '_L' + str(int(2*l))
elif(l==10.00) and (r3==5.00):
        jbname = jbname + '_s' + str(int(s))
elif(l==10.00) and (s==20.00):
```

```python
45            jbname = jbname + '_D' + str(int(2*r3))
46   pressure=0.15;    # applied pressure
47   dispbv=1;          # applied displacement
48   alpha=0 *pi/180;
49   ka=1.00;
50   E=100;          # Youg's modulus
51   nu=0.45;         # Poisson's ratio
52   r1=0.001;     # Radius of small circle at tip of inclusion
53   r2=1.00;      # Radius of bigger circle at tip of inclusion
54   c=2.00;        # Half Width of square at inclusion tip
55   c5=1.6*r3;   # c5= Half Width of square at hole
56   m2=10.00;     # max Mesh size in x-direction
57   m3=10.00;     # max Mesh size in y-direction
58   m5=0.001;     # Mesh size at small circle
59   m7=0.1;        # Mech size surounding to the hole
60   m1=0.25;       # mesh size upto square
61   m4=0.25;       # Mesh size on the box
62   m6=0.025;     # Mesh size at big circle
63   rt=(r2+c)/2;rt1=sin(pi/8);rt2=cos(pi/8);rt3=sin(3*pi/8);
64   rt4=cos(3*pi/8);
65   rt5=(r1+r2)/2;rt6=r1/2;rt7=(r3+c5)/2;rt8=sin(pi/4);
66   rt9=cos(pi/4)
67   myModel=mdb.Model('Model A')
68   mySketch = myModel.ConstrainedSketch( name='Sketch A', sheetSize=400.0)
69   session.journalOptions.setValues(replayGeometry=COORDINATE,recoverGeometry=
        COORDINATE)
70   mySketch.rectangle(point1=(-w,-b), point2=(w,b))
71   mySketch.CircleByCenterPerimeter(center=(0,a), point1=(0,a+r3))
72   myPart=myModel.Part(name='Part A', dimensionality=TWO_D_PLANAR,type=
        DEFORMABLE_BODY)
73   myPart.BaseShell(sketch=mySketch)
74   ## Material and cross-section assign
75   mdb.models['Model A'].Material(name='Matrix')
76   mdb.models['Model A'].materials['Matrix'].Elastic(table=((E, nu), ))
77   mdb.models['Model A'].HomogeneousSolidSection(material='Matrix', name='
        matrixSection', thickness=None)
78   p1 = mdb.models['Model A'].parts['Part A']
79   p1.Set(faces=p1.faces.findAt(((w*0.99, b*0.99, 0.0), )), name='Set-1')
80   p1.SectionAssignment(offset=0.0, offsetField='', offsetType=MIDDLE_SURFACE,
        region=p1.sets['Set-1'], sectionName='matrixSection', thicknessAssignment=
        FROM_SECTION)
81   ## Assembly Module
82   mdb.models['Model A'].rootAssembly.DatumCsysByDefault(CARTESIAN)
83   mdb.models['Model A'].rootAssembly.Instance(dependent=ON, name='Part A-1',
84       part=mdb.models['Model A'].parts['Part A'])
85   ## Partition
86   myModel.ConstrainedSketch(name='PartitionSketch', sheetSize=400)
```

```python
87   p2=mdb.models['Model A'].sketches['PartitionSketch']
88   # Inclusion Line
89   p2.Line(point1=(-l,-a), point2=(l,-a))
90   # Horizintal Partition lines near the inclusion tip
91   p2.Line(point1=(-w,-a-c), point2=(w,-a-c))
92   p2.Line(point1=(-w,-a+c), point2=(w,-a+c))
93   # Vertical Partition lines near the inclusion tip
94   if (-l-c)>(-c5):
95           p2.Line(point1=(-l-c,-b), point2=(-l-c,(a-c5)))
96   else:p2.Line(point1=(-l-c,-b), point2=(-l-c,b))
97   if (-l+c)>(-c5):
98           p2.Line(point1=(-l+c,-b), point2=(-l+c,(a-c5)))
99   else:p2.Line(point1=(-l+c,-b), point2=(-l+c,b))
100  if (l-c)<(c5):
101          p2.Line(point1=(l-c,-b), point2=(l-c,(a-c5)))
102  else:p2.Line(point1=(l-c,-b), point2=(l-c,b))
103  if (l+c)<(c5):
104          p2.Line(point1=(l+c,-b), point2=(l+c,(a-c5)))
105  else:p2.Line(point1=(l+c,-b), point2=(l+c,b))
106  # Horizontal Partition lines near the hole
107  p2.Line(point1=(-w, (a-c5)), point2=(w, (a-c5)))
108  p2.Line(point1=(-w, (a+c5)), point2=(w, (a+c5)))
109  # Vertical Partition lines near the hole
110  if ((-c5)>(-l-c)) and ((-c5)<(-l+c)):
111          p2.Line(point1=(-c5,a-c5), point2=(-c5,b))
112  else:p2.Line(point1=(-c5,-b), point2=(-c5,b))
113  if (c5>(l-c)) and (c5<(l+c)):
114          p2.Line(point1=(c5,a-c5), point2=(c5,b))
115  else:p2.Line(point1=(c5,-b), point2=(c5,b))
116  # Partition lines at the tip of the Inclusion
117  p2.Line(point1=(-l-c,-a-c), point2=(-l+c,-a+c))
118  p2.Line(point1=(-l+c,-a-c), point2=(-l-c,-a+c))
119  p2.Line(point1=(-l-c,-a), point2=(-l+c,-a))
120  p2.Line(point1=(-l,-a-c), point2=(-l,-a+c))
121  #
122  p2.Line(point1=(l-c,-a-c), point2=(l+c,-a+c))
123  p2.Line(point1=(l+c,-a-c), point2=(l-c,-a+c))
124  p2.Line(point1=(l-c,-a), point2=(l+c,-a))
125  p2.Line(point1=(l,-a-c), point2=(l,-a+c))
126  # Patition lines at Hole
127  p2.Line(point1=(0.0, a-c5), point2=(0.0, a+c5))
128  p2.Line(point1=(-c5, a-c5), point2=(c5, a+c5))
129  p2.Line(point1=(c5, a-c5), point2=(-c5, a+c5))
130  # Circles
131  p2.CircleByCenterPerimeter(center=(-l,-a), point1=(-l,-a+r1))
132  p2.CircleByCenterPerimeter(center=(-l,-a), point1=(-l,-a+r2))
133  p2.CircleByCenterPerimeter(center=(l,-a), point1=(l,-a+r1))
```

```python
134  p2 . CircleByCenterPerimeter ( center =( l ,−a ) ,  point1 =( l ,−a+r2 ) )
135  p1 . PartitionFaceBySketch ( faces=p1 . faces . findAt ( ( ( w∗0.99 ,  b∗0.99 ,  0.0 ) ,  ) ) ,
         sketch=p2 )
136  del  mdb . models [ ' Model−1 ' ]
137  ## Mesh Module ##
138  # ___1___##Horizontal  line − Single  Bias
139  p1 . seedEdgeByBias ( biasMethod=SINGLE , constraint=FINER ,  end2Edges=p1 . edges .
         findAt ( ( ( −0.99∗w,  b ,  0.0 ) ,  ) ,  ( ( −0.99∗w,  −a−c ,  0.0 ) ,  ) , ( ( −0.99∗w,  −a+c ,
         0.0 ) ,  ) , ( ( −0.99∗w,  a−c5 ,  0.0 ) ,  ) , ( ( −0.99∗w,  a+c5 ,  0.0 ) ,  ) ) ,  end1Edges=p1 .
         edges . findAt ( ( ( −0.99∗w,  −b ,  0.0 ) ,  ) , ) ,  maxSize=m2 ,  minSize=m1 )
140  ##
141  p1 . seedEdgeByBias ( biasMethod=SINGLE , constraint=FINER ,  end1Edges=p1 . edges .
         findAt ( ( ( 0.99∗w,  b ,  0.0 ) ,  ) ,  ( ( 0.99∗w,  −a−c ,  0.0 ) ,  ) , ( ( 0.99∗w,  −a+c ,  0.0 ) ,
          ) , ( ( 0.99∗w,  a−c5 ,  0.0 ) ,  ) , ( ( 0.99∗w,  a+c5 ,  0.0 ) ,  ) ) ,  end2Edges=p1 . edges .
         findAt ( ( ( 0.99∗w,  −b ,  0.0 ) ,  ) , ) ,  maxSize=m2 ,  minSize=m1 )
142  # ___2___## Vertical  line − Single  Bias
143  p1 . seedEdgeByBias ( biasMethod=SINGLE , constraint=FINER ,  end2Edges=p1 . edges .
         findAt ( ( ( −w,  −0.99∗b ,  0.0 ) ,  ) ,  ( ( −l−c ,  −0.99∗b ,  0.0 ) ,  ) ,  ( ( −l+c ,  −0.99∗b ,
         0.0 ) ,  ) , ( ( l−c ,  −0.99∗b ,  0.0 ) ,  ) ,  ( ( l+c ,  −0.99∗b ,  0.0 ) ,  ) ,  ( ( −c5 ,  −0.99∗b ,
         0.0 ) ,  ) , ( ( c5 ,  −0.99∗b ,  0.0 ) ,  ) , ) ,  end1Edges=p1 . edges . findAt ( ( ( w,  −0.99∗b ,
         0.0 ) ,  ) , ) ,  maxSize=m2 ,  minSize=m1 )
144  ##
145  p1 . seedEdgeByBias ( biasMethod=SINGLE , constraint=FINER ,  end1Edges=p1 . edges .
         findAt ( ( ( −w,  0.99∗b ,  0.0 ) ,  ) ,  ( ( −l−c ,  0.99∗b ,  0.0 ) ,  ) ,  ( ( −l+c ,  0.99∗b ,
         0.0 ) ,  ) , ( ( l−c ,  0.99∗b ,  0.0 ) ,  ) ,  ( ( l+c ,  0.99∗b ,  0.0 ) ,  ) ,  ( ( −c5 ,  0.99∗b ,
         0.0 ) ,  ) , ( ( c5 ,  0.99∗b ,  0.0 ) ,  ) , ) ,  end2Edges=p1 . edges . findAt ( ( ( w,  0.99∗b ,
         0.0 ) ,  ) , ) ,  maxSize=m2 ,  minSize=m1 )
146  ### middle  of  Inclusion  and Hole − Bias−None
147  ww=p1 . getDistance ( entity1=p1 . edges . findAt ( ( −0.99∗w,−a+c ,0.0 ) , ) ,  entity2=p1 .
         edges . findAt ( ( −0.99∗w, a−c5 ,0.0 ) , ) )
148  if  (ww>0 ) :
149          p1 . seedEdgeBySize ( edges=p1 . edges . findAt ( ( ( −w , a−c5∗1.01 ,  0.0 ) ,  ) , ( ( −l−
                 c , a−c5∗1.01 ,  0.0 ) ,  ) ,  ( ( −l+c , a−c5∗1.01 ,  0.0 ) ,  ) ,  ( ( l−c , a−c5
                 ∗1.01 ,  0.0 ) ,  ) , ( ( l+c , a−c5∗1.01 ,  0.0 ) ,  ) ,  ( ( w , a−c5∗1.01 ,  0.0 ) ,  )
                 , ( ( −c5 , a−c5∗1.01 ,  0.0 ) ,  ) , ( ( c5 , a−c5∗1.01 ,  0.0 ) ,  ) , ) ,  size=m1 ,
                 deviationFactor =0.1 , constraint=FINER )
150  # Near the  Inclusion ,  Vertical  line  seeding & side  end edges
151  p1 . seedEdgeBySize ( edges=p1 . edges . findAt ( ( ( −w,  −a ,  0.0 ) ,  ) , ( ( w,  −a ,  0.0 ) ,  ) , ( ( −
         l−c ,  −a−dt ,  0.0 ) ,  ) ,  ( ( −l−c ,  −a+dt ,  0.0 ) ,  ) , ( ( −l+c ,  −a−dt ,  0.0 ) ,  ) , ( ( −l+c ,
          −a+dt ,  0.0 ) ,  ) , ( ( l−c ,  −a−dt ,  0.0 ) ,  ) ,  ( ( l−c ,  −a+dt ,  0.0 ) ,  ) , ( ( l+c ,  −a−dt
         ,  0.0 ) ,  ) , ( ( l+c ,  −a+dt ,  0.0 ) ,  ) , ) ,  size=m4 ,  deviationFactor =0.1 ,
         constraint=FINER )
152  if  (−c5 ) <(−l−c ) :
153          p1 . seedEdgeBySize ( edges=p1 . edges . findAt ( ( ( −c5 ,  −a ,  0.0 ) ,  ) , ) ,  size=m4 ,
                 deviationFactor =0.1 , constraint=FINER )
154          p1 . seedEdgeBySize ( edges=p1 . edges . findAt ( ( ( c5 ,  −a ,  0.0 ) ,  ) , ) ,  size=m4 ,
                 deviationFactor =0.1 , constraint=FINER )
```

61

```python
155  # Near the Inclusion Horizontal line seeding & side end edges
156  p1.seedEdgeBySize(edges=p1.edges.findAt(((-l-dt, -a-c, 0.0), ),((-l-dt, -a+c,
         0.0), ),((-l+dt, -a-c, 0.0), ), ((-l+dt, -a+c, 0.0), ),    ((l-dt, -a-c,
         0.0), ),((l-dt, -a+c, 0.0), ),((l+dt, -a-c, 0.0), ),((l+dt, -a+c, 0.0), ),
          ((-l-c*0.99, -b, 0.0), ),((-l-c*0.99, b, 0.0), ),((l+c*0.99, -b, 0.0), )
         ,((l+c*0.99, b, 0.0), ), ((-l-c*0.99, a-c5, 0.0), ),((-l-c*0.99, a+c5,
         0.0), ),((l+c*0.99, a-c5, 0.0), ),((l+c*0.99, a+c5, 0.0), ), ((-l+c*1.01,
         -a+c, 0.0), ),((-l+c*1.01, -a-c, 0.0), ),((-l+c*1.01, -b, 0.0), ),((-l+c
         *1.01, b, 0.0), ),     ((l-c*1.01, -a+c, 0.0), ),((l-c*1.01, -a-c, 0.0), )
         ,((l-c*1.01, -b, 0.0), ),((l-c*1.01, b, 0.0), ),), size=m4,
         deviationFactor=0.1,constraint=FINER)
157  # Near the hole vertical line seeding
158  p1.seedEdgeBySize(edges=p1.edges.findAt(((-w, a, 0.0), ),((w, a, 0.0), ),((-c5
         , a, 0.0), ), ((c5, a, 0.0), ), ((-l-c, a, 0.0), ),((-l+c, a, 0.0), ),((l-
         c, a, 0.0), ), ((l+c, a, 0.0), ),), size=m4, deviationFactor=0.1,
         constraint=FINER)
159  # Near the hole horizontal line seeding
160  p1.seedEdgeBySize(edges=p1.edges.findAt(((0.0, -a-c, 0.0), ),((0.0, -a+c, 0.0)
         , ),((0.0, -b, 0.0), ),((0.0, b, 0.0), ), ((-c5*0.99, a-c5, 0.0), ),((c5
         *0.99, a-c5, 0.0), ),((-c5*0.99, a+c5, 0.0), ),((c5*0.99, a+c5, 0.0), ),
         ((dt, a-c5, 0.0), ),((-dt, a-c5, 0.0), ),), size=m4, deviationFactor=0.1,
         constraint=FINER)
161  ## 5 for inclusion circle
162  # __5-1__For left Side box
163  p1.seedEdgeByBias(biasMethod=SINGLE, constraint=FINER, end2Edges=p1.edges.
         findAt(((-l, -a-c*0.99, 0.0), ),((-l+rt, -a-rt, 0.0), ),((-l-c*0.99, -a,
         0.0), )),     end1Edges=p1.edges.findAt(((-l-rt, -a+rt, 0.0), ),((-l, -a+c
         *0.99, 0.0), ),     ((-l+c*0.99, -a, 0.0), ),), maxSize=m4, minSize=m6)
164  zh1=p1.edges.findAt((-l-rt, -a-rt, 0.0), ).getVertices()
165  sp1=p1.vertices.findAt((-l-r2*rt9, -a-r2*rt8, 0.0),).index
166  if zh1[0]==sp1:
167          p1.seedEdgeByBias(biasMethod=SINGLE, constraint=FINER, end1Edges=p1.
                 edges.findAt(((-l-rt, -a-rt, 0.0), ),), maxSize=m4, minSize=m6)
168  else:
169          p1.seedEdgeByBias(biasMethod=SINGLE, constraint=FINER, end2Edges=p1.
                 edges.findAt(((-l-rt, -a-rt, 0.0), ),), maxSize=m4, minSize=m6)
170  #
171  zh2=p1.edges.findAt((-l+rt, -a+rt, 0.0), ).getVertices()
172  sp2=p1.vertices.findAt((-l+r2*rt9, -a+r2*rt8, 0.0),).index
173  if zh2[0]==sp2:
174          p1.seedEdgeByBias(biasMethod=SINGLE, constraint=FINER, end1Edges=p1.
                 edges.findAt(((-l+rt, -a+rt, 0.0), ),), maxSize=m4, minSize=m6)
175  else:
176          p1.seedEdgeByBias(biasMethod=SINGLE, constraint=FINER, end2Edges=p1.
                 edges.findAt(((-l+rt, -a+rt, 0.0), ),), maxSize=m4, minSize=m6)
177  # __5-2__For Right Side box
178  p1.seedEdgeByBias(biasMethod=SINGLE, constraint=FINER, end2Edges=p1.edges.
```

```
        findAt (((1, -a-c*0.99, 0.0), ),((1+rt, -a-rt, 0.0), ),((1-c*0.99, -a, 0.0)
        , )), end1Edges=p1.edges.findAt (((1-rt, -a+rt, 0.0), ),((1, -a+c*0.99,
        0.0), ), ((1+c*0.99, -a, 0.0), ),), maxSize=m4, minSize=m6)
179 zh3=p1.edges.findAt ((1-rt, -a-rt, 0.0), ).getVertices()
180 sp3=p1.vertices.findAt ((1-r2*rt9, -a-r2*rt8, 0.0),).index
181 if zh3[0]==sp3:
182         p1.seedEdgeByBias(biasMethod=SINGLE,constraint=FINER, end1Edges=p1.
                edges.findAt (((1-rt, -a-rt, 0.0), ),), maxSize=m4, minSize=m6)
183 else:
184         p1.seedEdgeByBias(biasMethod=SINGLE,constraint=FINER, end2Edges=p1.
                edges.findAt (((1-rt, -a-rt, 0.0), ),), maxSize=m4, minSize=m6)
185 zh4=p1.edges.findAt ((1+rt, -a+rt, 0.0), ).getVertices()
186 sp4=p1.vertices.findAt ((1+r2*rt9, -a+r2*rt8, 0.0),).index
187 if zh4[0]==sp4:
188         p1.seedEdgeByBias(biasMethod=SINGLE,constraint=FINER, end1Edges=p1.
                edges.findAt (((1+rt, -a+rt, 0.0), ),), maxSize=m4, minSize=m6)
189 else:
190         p1.seedEdgeByBias(biasMethod=SINGLE,constraint=FINER, end2Edges=p1.
                edges.findAt (((1+rt, -a+rt, 0.0), ),), maxSize=m4, minSize=m6)
191 ## 6 for big circle
192 # __6-1__Right Side
193 p1.seedEdgeByBias(biasMethod=SINGLE,constraint=FINER, end2Edges=p1.edges.
        findAt (((1, -a-r2*0.99, 0.0), ), ((1-r2*0.99, -a, 0.0), ),((1+r1, -a-r1,
        0.0), ),), end1Edges=p1.edges.findAt (((1-r1, -a+r1, 0.0), ), ((1, -a+r2
        *0.99, 0.0), ),((1+r2*0.99, -a, 0.0), ),), maxSize=m6, minSize=m5)
194 #
195 zh5=p1.edges.findAt ((1-rt5, -a-rt5, 0.0), ).getVertices()
196 sp5=p1.vertices.findAt ((1-r1*rt9, -a-r1*rt8, 0.0),).index
197 if zh5[0]==sp5:
198         p1.seedEdgeByBias(biasMethod=SINGLE,constraint=FINER, end1Edges=p1.
                edges.findAt (((1-r1, -a-r1, 0.0), ),), maxSize=m6, minSize=m5)
199 else:
200         p1.seedEdgeByBias(biasMethod=SINGLE,constraint=FINER, end2Edges=p1.
                edges.findAt (((1-r1, -a-r1, 0.0), ),), maxSize=m6, minSize=m5)
201 #
202 zh6=p1.edges.findAt ((1+rt5, -a+rt5, 0.0), ).getVertices()
203 sp6=p1.vertices.findAt ((1+r1*rt9, -a+r1*rt8, 0.0),).index
204 if zh6[0]==sp6:
205         p1.seedEdgeByBias(biasMethod=SINGLE,constraint=FINER, end1Edges=p1.
                edges.findAt (((1+r1, -a+r1, 0.0), ),), maxSize=m6, minSize=m5)
206 else:
207         p1.seedEdgeByBias(biasMethod=SINGLE,constraint=FINER, end2Edges=p1.
                edges.findAt (((1+r1, -a+r1, 0.0), ),), maxSize=m6, minSize=m5)
208 # __6-1__Left Side
209 p1.seedEdgeByBias(biasMethod=SINGLE,constraint=FINER, end2Edges=p1.edges.
        findAt (((-1, -a-r2*0.99, 0.0), ), ((-1-r2*0.99, -a, 0.0), ),((-1+r1, -a-r1
        , 0.0), ),), end1Edges=p1.edges.findAt (((-1-r1, -a+r1, 0.0), ),        ((-1,
```

```python
                    -a+r2*0.99,  0.0) ,  ) ,((-l+r2*0.99,  -a,  0.0) ,  ) ,) ,  maxSize=m6,  minSize=m5)
#
zh5=p1.edges.findAt((-l-rt5,  -a-rt5,  0.0) ,  ).getVertices()
sp5=p1.vertices.findAt((-l-r1*rt9,  -a-r1*rt8,  0.0) ,).index
if  zh5[0]==sp5:
        p1.seedEdgeByBias(biasMethod=SINGLE,constraint=FINER,  end1Edges=p1.
            edges.findAt(((-l-r1,  -a-r1,  0.0) ,  ) ,) ,  maxSize=m6,  minSize=m5)
else:
        p1.seedEdgeByBias(biasMethod=SINGLE,constraint=FINER,  end2Edges=p1.
            edges.findAt(((-l-r1,  -a-r1,  0.0) ,  ) ,) ,  maxSize=m6,  minSize=m5)
#
zh6=p1.edges.findAt((-l+rt5,  -a+rt5,  0.0) ,  ).getVertices()
sp6=p1.vertices.findAt((-l+r1*rt9,  -a+r1*rt8,  0.0) ,).index
if  zh6[0]==sp6:
        p1.seedEdgeByBias(biasMethod=SINGLE,constraint=FINER,  end1Edges=p1.
            edges.findAt(((-l+r1,  -a+r1,  0.0) ,  ) ,) ,  maxSize=m6,  minSize=m5)
else:
        p1.seedEdgeByBias(biasMethod=SINGLE,constraint=FINER,  end2Edges=p1.
            edges.findAt(((-l+r1,  -a+r1,  0.0) ,  ) ,) ,  maxSize=m6,  minSize=m5)
### 7 for small circle - 1 element
#__7-1__Left Side
p1.seedEdgeByNumber(edges=p1.edges.findAt(((-l,  -a-r1*0.99,  0.0) ,  ) ,((-l-r1/2,
    -a+r1/2,  0.0) ,  ) ,  ((-l+r1/2,  -a+r1/2,  0.0) ,  ) ,((-l-r1*0.99,  -a,  0.0) ,  )
    ,((-l-r1/2,  -a-r1/2,  0.0) ,  ) ,((-l,  -a+r1*0.01,  0.0) ,  ) ,  ((-l+r1/2,  -a-r1
    /2,  0.0) ,  ) ,((-l+r1*0.99,  -a,  0.0) ,  )) ,  number=1,  constraint=FINER)
# __7-2__Right Side
p1.seedEdgeByNumber(edges=p1.edges.findAt(((l,  -a-r1*0.99,  0.0) ,  ) ,((l-r1/2,  -
    a+r1/2,  0.0) ,  ) ,  ((l+r1/2,  -a+r1/2,  0.0) ,  ) ,((l-r1*0.99,  -a,  0.0) ,  ) ,((l-
    r1/2,  -a-r1/2,  0.0) ,  ) ,((l,  -a+r1*0.01,  0.0) ,  ) ,  ((l+r1/2,  -a-r1/2,  0.0) ,
    ) ,((l+r1*0.99,  -a,  0.0) ,  )) ,  number=1,  constraint=FINER)
 ## 8 hole
# __8__
p1.seedEdgeByBias(biasMethod=SINGLE,constraint=FINER,  end2Edges=p1.edges.
    findAt(((0.0,  a-r3*1.01,  0.0) ,  ) ,  ((-r3,  a-r3,  0.0) ,  ) ,((r3,  a-r3,  0.0) ,  )
    ) ,end1Edges=p1.edges.findAt(((-r3,  a+r3,  0.0) ,  ) ,  ((r3,  a+r3,  0.0) ,  )
    ,((0.0,  a+r3*1.01,  0.0) ,  )) ,  maxSize=m1,  minSize=m7)
#
zh9=p1.edges.findAt((rt7,  a-rt7,  0.0) ,  ).getVertices()
sp9=p1.vertices.findAt((r3*rt9,  a-r3*rt8,  0.0) ,).index
if  zh9[0]==sp9:
        p1.seedEdgeByBias(biasMethod=SINGLE,constraint=FINER,  end1Edges=p1.
            edges.findAt(((rt7,  a-rt7,  0.0) ,  ) ,) ,  maxSize=m1,  minSize=m7)
else:
        p1.seedEdgeByBias(biasMethod=SINGLE,constraint=FINER,  end2Edges=p1.
            edges.findAt(((rt7,  a-rt7,  0.0) ,  ) ,) ,  maxSize=m1,  minSize=m7)
#
zh11=p1.edges.findAt((-rt7,  a+rt7,  0.0) ,  ).getVertices()
```

```python
sp11=p1.vertices.findAt((( -r3*rt9 , a+r3*rt8 , 0.0 ),).index
if zh11[0]==sp11:
        p1.seedEdgeByBias(biasMethod=SINGLE,constraint=FINER, end1Edges=p1.
            edges.findAt((( -rt7 , a+rt7 , 0.0 ), ),), maxSize=m1, minSize=m7)
else:
        p1.seedEdgeByBias(biasMethod=SINGLE,constraint=FINER, end2Edges=p1.
            edges.findAt((( -rt7 , a+rt7 , 0.0 ), ),), maxSize=m1, minSize=m7)
## dependent OFF
mdb.models['Model A'].rootAssembly.Instance(dependent=OFF, name='Part A-1',
    part=mdb.models['Model A'].parts['Part A'])
p3=mdb.models['Model A'].rootAssembly.regenerate()
p3=mdb.models['Model A'].rootAssembly
## Set for Inclusion
p3.Set(edges=p3.instances['Part A-1'].edges.findAt((( -l+r1*0.99,-a , 0.0 ), ),
    (( -l+r1*1.01,-a , 0.0 ), ),(( -l+r2*1.01,-a , 0.0 ), ),(( l-r1*0.99,-a , 0.0 ),
     ), (( l-r1*1.01,-a , 0.0 ), ),(( l-r2*1.01,-a , 0.0 ), ),(( l-c*1.01,-a , 0.0 )
    , ), (( -l+c*1.01,-a , 0.0 ), ),(( 0.0 , -a , 0.0 ), ),), name='Inclusion')
## Defining the Crack
## ---#1---Left side crack
p3.engineeringFeatures.ContourIntegral(collapsedElementAtTip=DUPLICATE_NODES,
    crackFront=p3.sets['Inclusion'], crackTip=Region(vertices=p3.instances['
    Part A-1'].vertices.findAt(((-l , -a , 0.0 ), ), )), extensionDirectionMethod
    =Q_VECTORS, midNodePosition=0.25, name='CrackLeft', qVectors=((p3.
    instances['Part A-1'].vertices.findAt((-l , -a , 0.0 ), ), p3.instances['Part
     A-1'].vertices.findAt((-l-c , -a , 0.0 ), )), ), symmetric=ON)
## ---#2---Right Side crack
p3.engineeringFeatures.ContourIntegral(collapsedElementAtTip=DUPLICATE_NODES,
    crackFront=p3.sets['Inclusion'], crackTip=Region(vertices=p3.instances['
    Part A-1'].vertices.findAt(((l , -a , 0.0 ), ), )), extensionDirectionMethod=
    Q_VECTORS, midNodePosition=0.25, name='CrackRight', qVectors=((p3.
    instances['Part A-1'].vertices.findAt((l , -a , 0.0 ), ), p3.instances['Part
     A-1'].vertices.findAt((l+c , -a , 0.0 ), )), ), symmetric=ON)
## Assign Mesh Control ##
p3.setMeshControls(regions=p3.instances['Part A-1'].faces.findAt((( -0.99*w,
    -0.99*b , 0.0 ), ),(( -0.99*w, 0.99*b , 0.0 ), ), (( -0.99*w, -a , 0.0 ), )
    ,(( -0.99*w, a , 0.0 ), ),((0.99*w, -0.99*b , 0.0 ), ),((0.99*w, 0.99*b , 0.0 ),
    ), ((0.99*w, -a , 0.0 ), ),((0.99*w, a , 0.0 ), ),((-l-c*0.99, -0.99*b , 0.0 ),
    ) ,((l+c*0.99, -0.99*b , 0.0 ), ), ((0.0 , -0.99*b , 0.0 ), ),((0.0 , 0.99*b ,
    0.0 ), ),((0.0 , -a-dt , 0.0 ), ),((0.0 , -a+dt , 0.0 ), ), ), elemShape=QUAD,
    technique=STRUCTURED)
if (ww!=0):
        p3.setMeshControls(regions=p3.instances['Part A-1'].faces.findAt
            ((( -0.99*w, a-c5*1.01 , 0.0 ), ),((0.99*w, a-c5*1.01 , 0.0 ), ), ((-l,
             a-c5*1.01 , 0.0 ), ),((l , a-c5*1.01 , 0.0 ), ),((-l+c*1.01, a-c5
            *1.01 , 0.0 ), ), ((l-c*1.01, a-c5*1.01 , 0.0 ), ),((0.0 , a-c5*1.01 ,
            0.0 ), ),), elemShape=QUAD, technique=STRUCTURED)
#
```

```python
262  if ((-c5)>(-1-c)):
263          p3.setMeshControls(regions=p3.instances['Part A-1'].faces.findAt(((-1-
                 c*0.99, 0.99*b, 0.0), ),((-1-c*0.99, a, 0.0), ),),elemShape=QUAD,
                 technique=STRUCTURED)
264  #
265  if (c5<(1+c)):
266          p3.setMeshControls(regions=p3.instances['Part A-1'].faces.findAt(((1+c
                 *0.99, 0.99*b, 0.0), ),((1+c*0.99, a, 0.0), ),),  elemShape=QUAD,
                 technique=STRUCTURED)
267  #
268  if (-1+c)<(-c5):
269          p3.setMeshControls(regions=p3.instances['Part A-1'].faces.findAt(((-1+
                 c*1.01, -0.99*b, 0.0), ),((-1+c*1.01, 0.99*b, 0.0), ), ((-1+c
                 *1.01, a, 0.0), ),((-1+c*1.01, 0.0, 0.0), ),((-1+c*1.01, -a-dt,
                 0.0), ), ((-1+c*1.01, -a+dt, 0.0), ),), elemShape=QUAD, technique=
                 STRUCTURED)
270  #
271  if (1-c)>(c5):
272          p3.setMeshControls(regions=p3.instances['Part A-1'].faces.findAt(((1-c
                 *1.01, -0.99*b, 0.0), ),((1-c*1.01, 0.99*b, 0.0), ),((1-c*1.01, a,
                  0.0), ), ((1-c*1.01, 0.0, 0.0), ),((1-c*1.01, -a-dt, 0.0), ), ((1
                 -c*1.01, -a+dt, 0.0), ),          ), elemShape=QUAD, technique=
                 STRUCTURED)
273  #
274  if ((-c5)<(-1-c)):
275          p3.setMeshControls(regions=p3.instances['Part A-1'].faces.findAt(((-c5
                 +dt, a-c5*1.01, 0.0), ),((-c5+dt, -a, 0.0), ), ((-c5+dt, -a-c
                 *1.01, 0.0), ),), elemShape=QUAD, technique=STRUCTURED)
276  #
277  if (c5>(1+c)):
278          p3.setMeshControls(regions=p3.instances['Part A-1'].faces.findAt(((c5-
                 dt, a-c5*1.01, 0.0), ),((c5-dt, -a, 0.0), ), ((c5-dt, -a-c*1.01,
                 0.0), ),), elemShape=QUAD, technique=STRUCTURED)
279  # Left Side Box except inner small circle
280  p3.setMeshControls(regions=p3.instances['Part A-1'].faces.findAt(((-1+rt*rt2,
        -a+rt*rt1, 0.0),),((-1-rt*rt2, -a+rt*rt1, 0.0),), ((-1-rt*rt2, -a-rt*rt1,
        0.0),),((-1+rt*rt2, -a-rt*rt1, 0.0),),((-1+rt*rt4, -a+rt*rt3, 0.0),), ((-1
        -rt*rt4, -a+rt*rt3, 0.0),),((-1-rt*rt4, -a-rt*rt3, 0.0),),((-1+rt*rt4, -a-
        rt*rt3, 0.0),), ((-1+rt5*rt2, -a+rt5*rt1, 0.0),),((-1-rt5*rt2, -a+rt5*rt1,
         0.0),),((-1-rt5*rt2, -a-rt5*rt1, 0.0),), ((-1+rt5*rt2, -a-rt5*rt1, 0.0),)
        ,((-1+rt5*rt4, -a+rt5*rt3, 0.0),),((-1-rt5*rt4, -a+rt5*rt3, 0.0),),
        ((-1-rt5*rt4, -a-rt5*rt3, 0.0),),((-1+rt5*rt4, -a-rt5*rt3, 0.0),)),
        elemShape=QUAD, technique=SWEEP)
281  # Right Box except inner small circle
282  p3.setMeshControls(regions=p3.instances['Part A-1'].faces.findAt(((1+rt*rt2, -
        a+rt*rt1, 0.0),),((1-rt*rt2, -a+rt*rt1, 0.0),), ((1-rt*rt2, -a-rt*rt1,
        0.0),),((1+rt*rt2, -a-rt*rt1, 0.0),),((1+rt*rt4, -a+rt*rt3, 0.0),), ((1-rt
```

```python
                *rt4 , -a+rt*rt3 , 0.0) ,) ,((l-rt*rt4 , -a-rt*rt3 , 0.0) ,) ,((l+rt*rt4 , -a-rt*
                rt3 , 0.0) ,) , ((l+rt5*rt2 , -a+rt5*rt1 , 0.0) ,) ,((l-rt5*rt2 , -a+rt5*rt1 , 0.0)
                ,) ,((l-rt5*rt2 , -a-rt5*rt1 , 0.0) ,) , ((l+rt5*rt2 , -a-rt5*rt1 , 0.0) ,) ,((l+
                rt5*rt4 , -a+rt5*rt3 , 0.0) ,) ,((l-rt5*rt4 , -a+rt5*rt3 , 0.0) ,) , ((l-rt5*rt4 ,
                -a-rt5*rt3 , 0.0) ,) ,((l+rt5*rt4 , -a-rt5*rt3 , 0.0) ,)) , elemShape=QUAD,
                technique=SWEEP)
283 # For Left side Inner Small Circle
284 p3.setMeshControls(regions=p3.instances['Part A-1'].faces.findAt(((-l+rt6*rt2 ,
         -a+rt6*rt1 , 0.0) ,) ,((-l-rt6*rt2 , -a+rt6*rt1 , 0.0) ,) ,      ((-l-rt6*rt2 , -a
        -rt6*rt1 , 0.0) ,) ,((-l+rt6*rt2 , -a-rt6*rt1 , 0.0) ,) ,((-l+rt6*rt4 , -a+rt6*rt3
        , 0.0) ,) ,      ((-l-rt6*rt4 , -a+rt6*rt3 , 0.0) ,) ,((-l-rt6*rt4 , -a-rt6*rt3 ,
        0.0) ,) ,((-l+rt6*rt4 , -a-rt6*rt3 , 0.0) ,)) , elemShape=QUAD_DOMINATED,
        technique=SWEEP)
285 # For Right side Inner Small Circle
286 p3.setMeshControls(regions=p3.instances['Part A-1'].faces.findAt(((l+rt6*rt2 ,
        -a+rt6*rt1 , 0.0) ,) ,((l-rt6*rt2 , -a+rt6*rt1 , 0.0) ,) , ((l-rt6*rt2 , -a-rt6*
        rt1 , 0.0) ,) ,((l+rt6*rt2 , -a-rt6*rt1 , 0.0) ,) ,((l+rt6*rt4 , -a+rt6*rt3 , 0.0)
        ,) , ((l-rt6*rt4 , -a+rt6*rt3 , 0.0) ,) ,((l-rt6*rt4 , -a-rt6*rt3 , 0.0) ,) ,((l+
        rt6*rt4 , -a-rt6*rt3 , 0.0) ,)) , elemShape=QUAD_DOMINATED, technique=SWEEP)
287 # In the Square box surrounded to the hole
288 p3.setMeshControls(regions=p3.instances['Part A-1'].faces.findAt(((rt7*rt4 , a+
        rt7*rt3 , 0.0) ,) ,((-rt7*rt4 , a+rt7*rt3 , 0.0) ,) , ((rt7*rt4 , a-rt7*rt3 , 0.0)
        ,) ,((-rt7*rt4 , a-rt7*rt3 , 0.0) ,) ,((-rt7 , a , 0.0) ,) , ((rt7 , a , 0.0) ,) ,) ,
        elemShape=QUAD, technique=SWEEP)
289 ## set AREA
290 # p3.Set(faces=p3.instances['Part A-1'].faces.findAt(((-l+rt5*rt2 , -a+rt5*rt1 ,
         0.0) ,) , ((-l-rt5*rt2 , -a+rt5*rt1 , 0.0) ,) ,((-l-rt5*rt2 , -a-rt5*rt1 , 0.0) ,)
        , ((-l+rt5*rt2 , -a-rt5*rt1 , 0.0) ,) ,((-l+rt5*rt4 , -a+rt5*rt3 , 0.0) ,) ,((-l-
        rt5*rt4 , -a+rt5*rt3 , 0.0) ,) , ((-l-rt5*rt4 , -a-rt5*rt3 , 0.0) ,) ,((-l+rt5*rt4
        , -a-rt5*rt3 , 0.0) ,)) , name='Area')
291 p3.Set(faces=p3.instances['Part A-1'].faces.findAt(((l+rt5*rt2 , -a+rt5*rt1 ,
        0.0) ,) , ((l-rt5*rt2 , -a+rt5*rt1 , 0.0) ,) ,((l-rt5*rt2 , -a-rt5*rt1 , 0.0) ,) ,
        ((l+rt5*rt2 , -a-rt5*rt1 , 0.0) ,) ,((l+rt5*rt4 , -a+rt5*rt3 , 0.0) ,) ,((l-rt5*
        rt4 , -a+rt5*rt3 , 0.0) ,) , ((l-rt5*rt4 , -a-rt5*rt3 , 0.0) ,) ,((l+rt5*rt4 , -a-
        rt5*rt3 , 0.0) ,)) , name='Area')
292 ## Generating the Mesh
293 p3.generateMesh(regions=(p3.instances['Part A-1'], ))
294 p3.regenerate()
295 p3.setElementType(elemTypes=(ElemType(elemCode=CPE8H, elemLibrary=STANDARD),
        ElemType(elemCode=CPE6H, elemLibrary=STANDARD)), regions=(p3.instances['
        Part A-1'].              faces.getByBoundingBox(-1.01*w, -1.01*w, -100,    w
        *1.01, b*1.01, 100), ))
296 ### Creating Static General Step ###
297 mdb.models['Model A'].StaticStep(name='Step-1', previous='Initial')
298 p3.Set(name='Node-A', nodes=(p3.instances['Part A-1'].nodes.
        getByBoundingSphere(center=((l, -a, 0)),radius=dt) ,))
299 p3.Set(name='Node-B', nodes=(p3.instances['Part A-1'].nodes.
```

```
        getByBoundingSphere ( center=((−l , −a, 0)) , radius=dt ) , ) )
300  xya=p3 . s e t s [ 'Node−A ' ] . nodes [ 0 ] . coordinates
301  xyb=p3 . s e t s [ 'Node−B ' ] . nodes [ 0 ] . coordinates
302  la=p3 . s e t s [ 'Node−A ' ] . nodes [ 0 ] . label
303  ## Specifying Inclusion ##
304  ## Reference point
305  RP1=p3 . ReferencePoint ( point =(0.0 , −a, 0.0))
306  mdb. models [ 'Model A ' ] . RigidBody (name= 'Constraint −1 ', pinRegion=p3 . s e t s [ '
        Inclusion ' ] , refPointAtCOM=ON, refPointRegion=Region ( referencePoints =(p3 .
        referencePoints [RP1.id ] , ) ) )
307  ## Set for BC
308  p3 . Set ( edges=p3 . instances [ 'Part A−1 ' ] . edges . findAt (((−w, −0.99∗b, 0.0) , ) ,((−w
        , 0.99∗b, 0.0) , ) , ((−w, a, 0.0) , ) ,((−w, −a, 0.0) , ) ,((−w, a−c5 ∗1.01 ,
        0.0) , ) , ) , name= 'SetLeftBC ')
309  #
310  p3 . Set ( edges=p3 . instances [ 'Part A−1 ' ] . edges . findAt (((w, −0.99∗b, 0.0) , ) ,((w,
        0.99∗b, 0.0) , ) , ((w, a, 0.0) , ) ,((w, −a, 0.0) , ) ,((w, a−c5 ∗1.01 , 0.0) , )
        , ) , name= 'SetRightBC ')
311  #
312  p3 . Set ( vertices=p3 . instances [ 'Part A−1 ' ] . vertices . findAt (((−w, −b, 0.0) , ) , ) ,
        name= 'SetLLConr ')
313  ## Applying BC
314  mdb. models [ 'Model A ' ] . DisplacementBC ( amplitude=UNSET, createStepName= 'Step −1 ',
        distributionType=UNIFORM, fieldName= ' ' , fixed=OFF, localCsys=None , name= '
        BC−LeftSd ', region=p3 . s e t s [ 'SetLeftBC ' ] , u1=0.0 , u2=UNSET, ur3=UNSET)
315  #
316  # mdb. models [ 'Model A ' ] . DisplacementBC ( amplitude=UNSET, createStepName= 'Step
        −1 ', distributionType=UNIFORM, fieldName= ' ' , fixed=OFF, localCsys=None ,
        name= 'BC−RightSd ', region=p3 . s e t s [ 'SetRightBC ' ] , u1=dispbv , u2=UNSET, ur3
        =UNSET)
317  #
318  mdb. models [ 'Model A ' ] . DisplacementBC ( amplitude=UNSET, createStepName= 'Step −1 ',
        distributionType=UNIFORM, fieldName= ' ' , fixed=OFF, localCsys=None , name= '
        BC−LLpt ', region=p3 . s e t s [ 'SetLLConr ' ] , u1=UNSET, u2=0.0 , ur3=UNSET)
319  ## Applying Pressure ##
320  # creating Surface to apply pressure
321  # p3 . Surface (name= 'SurfLoadLeft ', side1Edges=p3 . instances [ 'Part A−1 ' ] . edges .
        findAt (((−w, −0.99∗b, 0.0) , ) ,((−w, 0.99∗b, 0.0) , ) ,((−w, a, 0.0) , ) ,((−w,
        −a, 0.0) , ) , ((−w, a−c5 ∗1.01 , 0.0) , ) , ) )
322  p3 . Surface (name= 'SLR ', side1Edges=p3 . instances [ 'Part A−1 ' ] . edges . findAt (((w,
        −0.99∗b, 0.0) , ) ,((w, 0.99∗b, 0.0) , ) ,((w, a, 0.0) , ) ,((w, −a, 0.0) , ) ,((w
        , a−c5 ∗1.01 , 0.0) , ) , ) )
323  # # Giving pressure
324  # mdb. models [ 'Model A ' ] . Pressure ( amplitude=UNSET, createStepName= 'Step −1 ',
        distributionType=UNIFORM, f i e l d = ' ' , magnitude=−pressure , name= 'LoadLeft ',
        region=p3 . instances [ 'Part A−1 ' ] . surfaces [ 'SurfLoadLeft ' ])
325  mdb. models [ 'Model A ' ] . Pressure ( amplitude=UNSET, createStepName= 'Step −1 ',
```

```
              distributionType=UNIFORM, field='', magnitude=-pressure, name='Load-1',
              region= p3.surfaces['SLR'])
326  # mdb.models['Model A'].Pressure(amplitude=UNSET, createStepName='Step-1',
              distributionType=UNIFORM, field='', magnitude=-pressure, name='Load-1',
              region=mdb.models['Model A'].rootAssembly.surfaces['Surf-1'])
327  ## Creating the Job ##
328  mdb.Job(name=jbname, model='Model A', description='', type=ANALYSIS, queue='',
              waitHours=0, waitMinutes=0, atTime='', echoPrint=OFF, contactPrint=OFF,
              modelPrint=OFF, historyPrint=OFF, scratch='', userSubroutine='', numCpus
              =1, memory=90, memoryUnits=PERCENTAGE, getMemoryFromAnalysis=ON,
              explicitPrecision=SINGLE, nodalOutputPrecision=SINGLE, multiprocessingMode
              =DEFAULT)
329  ## Submitting the Job
330  mdb.jobs[jbname].submit(consistencyChecking=OFF)
331  mdb.jobs[jbname].waitForCompletion()
332  ## POST PROCESSING ##
333  jname = jbname
334  odbname= jname+'.odb'
335  odb = openOdb(odbname)
336  assembly    = odb.rootAssembly
337  nodes=odb.rootAssembly.instances['Part A-1'].nodes
338  elements=odb.rootAssembly.instances['Part A-1'].elements
339  nelm = len(elements)
340  nnod = len(nodes)
341  session.viewports['Viewport: 1'].setValues(displayedObject=odb)
342  path = session.Path(name='path', type=POINT_LIST, expression=((l, -s/2, 0.0), (
         l+10, -s/2, 0.0)))
343  data = session.XYDataFromPath(name='data',
344       path=path,
345       includeIntersections=True,
346       shape=UNDEFORMED,
347       labelType=TRUE_DISTANCE,
348       variable=('S',INTEGRATION_POINT,((COMPONENT, 'S11'),),))
349  dataS11 = numpy.zeros(shape=(0,2))
350  temp = numpy.zeros(shape=(2))
351  for value in range(0,len(data)):
352           temp[0] =   data[value][0]
353           temp[1] =   data[value][1]
354           dataS11=numpy.vstack((dataS11,temp))
355  data = session.XYDataFromPath(name='data',
356       path=path,
357       includeIntersections=True,
358       shape=UNDEFORMED,
359       labelType=TRUE_DISTANCE,
360       variable=('S',INTEGRATION_POINT,((COMPONENT, 'S22'),),))
361  dataS22 = numpy.zeros(shape=(0,2))
362  temp = numpy.zeros(shape=(2))
```

```python
363  for value in range(0,len(data)):
364          temp[0] =  data[value][0]
365          temp[1] =  data[value][1]
366          dataS22=numpy.vstack((dataS22,temp))
367  data = session.XYDataFromPath(name='data',
368       path=path,
369       includeIntersections=True,
370       shape=UNDEFORMED,
371       labelType=TRUE_DISTANCE,
372       variable=('S',INTEGRATION_POINT,((COMPONENT,'S12'),),))
373  dataS12 = numpy.zeros(shape=(0,2))
374  temp = numpy.zeros(shape=(2))
375  for value in range(0,len(data)):
376          temp[0] =  data[value][0]
377          temp[1] =  data[value][1]
378          dataS12=numpy.vstack((dataS12,temp))
379  numpy.savetxt(jname+'_dataS11.dat', dataS11, fmt='%15.7e %15.7e ')
380  numpy.savetxt(jname+'_dataS22.dat', dataS22, fmt='%15.7e %15.7e ')
381  numpy.savetxt(jname+'_dataS12.dat', dataS12, fmt='%15.7e %15.7e ')
382  mylist=[]
383  for inode in range(0,nnod):
384          mylist.append(nodes[inode].coordinates)
385  x= numpy.array(mylist)
386  mylist=[]
387  disp_big = odb.steps['Step-1'].frames[1].fieldOutputs['U']
388  for inode in range(0,nnod):
389          mylist.append(disp_big.values[inode].data )
390          if inode==la-1:
391                  aaa=list(disp_big.values[inode].data )
392  disp= numpy.array(mylist)
393  mylist=[]
394  for ielement in range(0,nelm):
395          if len(elements[ielement].connectivity) == 8:
396                  ab=list(elements[ielement].connectivity)
397                  ab.insert(0,elements[ielement].label)
398                  mylist.append(ab)
399          else:
400                  a=[0,1,2,3,4,5,6,7]
401                  a.insert(0,elements[ielement].label)
402                  mylist.append(a)
403  icon= numpy.array(mylist)
404  nelsets = len(odb.rootAssembly.elementSets['AREA'].elements[0])
405  mylist=[]
406  elset_big = odb.rootAssembly.elementSets['AREA']
407  for i in range(0,nelsets):
408      mylist.append(elset_big.elements[0][i].label)
409  elset= numpy.array(mylist)
```

```
410  iintp=0;
411  ngp=9;
412  stress_big = odb.steps['Step-1'].frames[1].fieldOutputs['S']
413  strain_big = odb.steps['Step-1'].frames[1].fieldOutputs['E']
414  stress = numpy.zeros(shape=(0,5))
415  strain = numpy.zeros(shape=(0,5))
416  temp = numpy.zeros(shape=(5))
417  for ielement in  elset:
418      #print ielement
419    for iintp in range(0,9):
420          index=(ielement-1)*ngp+iintp
421          #index=(ielement)*ngp+iintp
422          temp[0] =  ielement
423          temp[1] =  iintp+1
424          temp[2] = stress_big.values[index].data[0]
425          temp[3] = stress_big.values[index].data[1]
426          temp[4] = stress_big.values[index].data[3]
427          stress=numpy.vstack((stress,temp))
428          temp[0] =  ielement
429          temp[1] =  iintp+1
430          temp[2] = strain_big.values[index].data[0]
431          temp[3] = strain_big.values[index].data[1]
432          temp[4] = strain_big.values[index].data[3]
433          strain=numpy.vstack((strain,temp))
434  data=list(range(0,13))
435  prtc=nodes[la-1].coordinates
436  data[0]=l; data[1]=r1; data[2]=r2; data[3]=alpha; data[4]=E; data[5]=nu; data
          [6]=pressure;
437  data[7]=la; data[8]=prtc[0]; data[9]=prtc[1]; data[10]=aaa[0];
438  data[11]=aaa[1]; data[12]=ka
439  data= numpy.array(data)
440  numpy.savetxt(jname+'_data.dat', data)
441  numpy.savetxt(jname+'_x.dat', x)
442  numpy.savetxt(jname+'_icon.dat', icon, fmt='%8i')
443  numpy.savetxt(jname+'_disp.dat', disp)
444  numpy.savetxt(jname+'_stress.dat',stress,fmt='%8i %8i %15.7e %15.7e %15.7e ')
445  numpy.savetxt(jname+'_strain.dat',strain,fmt='%8i %8i %15.7e %15.7e %15.7e ')
446  odb.close()
```

Appendix C: Plotting fringe Contours from FEA results

To validate our finite element analysis results with photoelastic results, we reconstruct the fringe contours using the nodal stress data, connectivity data and xy data from the FEA results. This method is adopted from the work of Ramesh et al. [40]. The optical technique, photoelasticity, gives the whole field fringe contours corresponding to the principal stress difference and principal stress orientation. These fringe order and the principal stress are related by the relation

$$(\sigma_1 - \sigma_2) = \frac{NF_\sigma}{t}, \tag{1}$$

where, σ_1, and σ_2 are the principal stresses in 1 and 2 direction, F_σ is the material fringe values which is fixed for a material and t is the specimen thickness. This relation is applied at a point in the problem domain. In general, Eqn.1 can be represented as

$$\psi = NK, \tag{2}$$

where, N is the fringe order and K is the factor calculated for particular experiment. So the fringe order at a point can be calculated by ψ/K. For the plotting of fringe contours, initially the fringe order is calculated from stress data directly. Also, if the node is common to many elements, then the stress can be averaged,

$$\sigma_i = \frac{1}{n} \sum_{j=1}^{n} \sigma_i^j \tag{3}$$

To plot the fringe contours i.e. to use the relation Eqn. 1 , firstly find the principal stress difference $(\sigma_1 - \sigma_2)$ at the each nodes from the σ_x, σ_y and τ_{xy} stress values, as we have nodal stress data from FEA results. Then we can calculate the fringe order as

$$N_i = \frac{(\sigma_1 - \sigma_2)_i t}{F_\sigma}. \tag{4}$$

But to plot fringe contours, we still need the fringe order values at the intermediate point, so that validation with photoelastic results will be precise. To do so with new scheme, instead of solving the non-linear equation, here a each element in the domain is scanned discretely, for which the plot has to be made, a field variable is calculated. A check is done, to find out whether this fringe value is integer or not. If so, then this point is plotted. The quality of the plot is depends upon the scanning interval. For our results, the scanning interval is fixed to be $0.01mm$ to get good quality plot. For each point of interest within the element, the global co-ordinates and the fringe order are calculated, using the shape function as the interpolation functions as

$$
\begin{aligned}
x_g &= N_1 x_1 + N_2 x_2 + ... + N_8 x_8 \\
y_g &= N_1 y_1 + N_2 y_2 + ... + N_8 y_8 \\
frn_g &= N_1 frn_1 + N_2 frn_2 + ... + N_8 frn_8,
\end{aligned} \tag{5}
$$

where, x_i and y_i are nodal co-ordinates of the element, x_g and y_g are the global co-ordinates of the point of interest, $N_1, N_2, ..., N_8$ are the shape functions for interpolation, $frn_1, frn_2, ..., frn_8$ are the known fringe order values of elemental nodes and frn_g is fringe order values of the point of interest
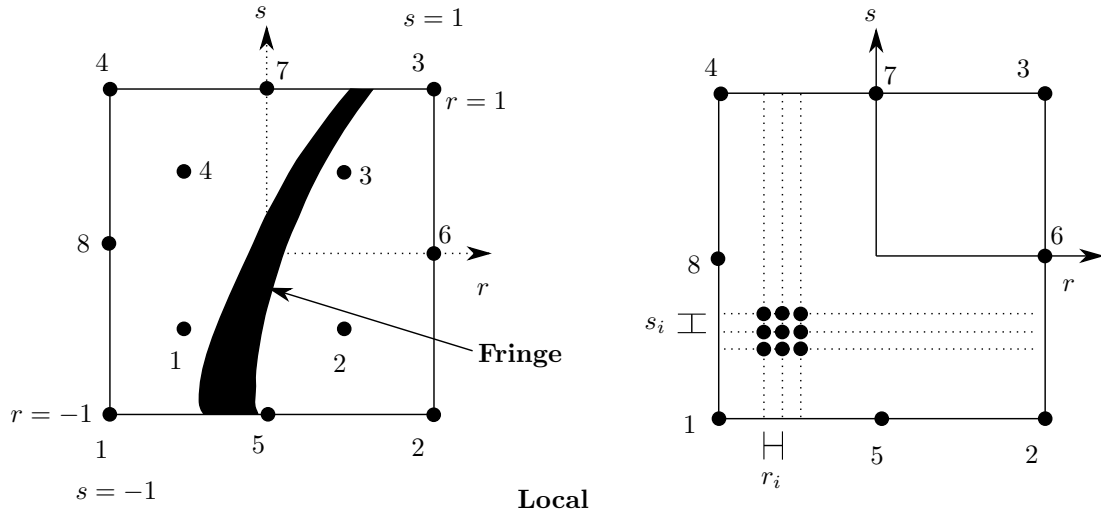
Figure 2: The element in natural coordinate system (a) fringe contour (b) scanning interval.

being scanned. Fringes in the fringe contours plot appears as broad bands. Hence to get this effect, we plot the points whose fringe value lie in the range $N \pm e$ rather than just N. Generally, the value of the e is of the order 0.1. Hence, when plotting the fringe contours 1,2,3,..., etc., it satisfies the following condition:

$$abs((frn) - round(frn)) \leqslant 0.1 \qquad (6)$$

and for the fringe contours 0.5,1.5,2.5,..., etc., it satisfies the following condition:

$$abs((frn + 0.5) - round(frn + 0.5)) \leqslant 0.1 \qquad (7)$$